

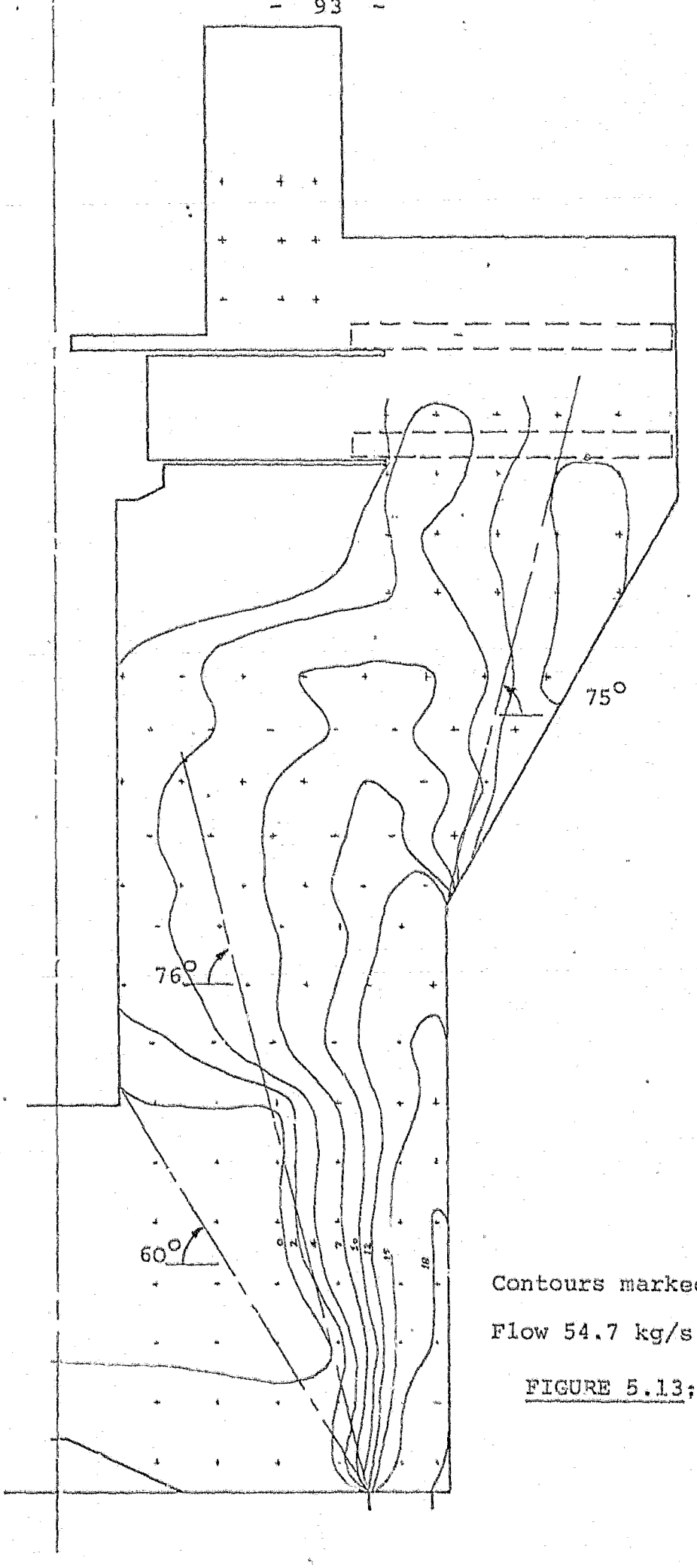
https://dspace.org/

A study of the parameters affecting the design of vertical spindle mills

De Wet Kruger, John Ivor

2015-03-05
http://hdl.handle.net/10539/17158

Downloaded from a DSpace repository. https://dspace.org/



Contours marked in ft/s

Flow 54.7 kg/s

FIGURE 5.13; Pitot traverse of model.

TEST 2

The middle of the mill (in the region above the table) forms an area of zero, or reverse, flow - which is logical since this is the area where the feed is introduced, as well as being a large dead region. A cone of approxiamtely 60° included angle can be taken as representing this dead region, and hence any design incorporating a return of oversize particles to this region will ensure that the particles fall back onto the table for further grinding (see Figure 5.14).

A Coanda effect was noticeable up the sides; this would lead to high wear when the air was carrying particles picked up off the table. It also meant that the velocity at the point of body divergence was high, which would lead to problems in returning separator oversize back on to the table. The working principle of the separator is that any oversize particles will fall down the sides of the cone section and on to the table, their being too large to be entrained at the velocity at that point in the mill. However, a local high velocity will immediately entrain large particles and cause a local recirculating load which will only decrease when the load is too high to be supported, and ultimately collapses on to the table. This leads to irregular mill operation.

If the divergence recirculating boundary is extended, it will be seen that the separator blades are doing very little, if any, work in the region corresponding to the outer 20% of the radius and all the classification is being achieved in the inner 80% of the blade. In fact, if the blades were shortened, it is doubtful whether any significant size change would take place,

and the blades could be effectively speeded up without overloading the drive. Typical blade wear is shown in Figure 5.15.

This series of model tests led to the following conclusions:

(i) The flow distribution at the louvre ports was uneven.
(ii) The Coanda effect was linked to this distribution, and hence high wear could be expected.
(iii) There were zero or reverse flow regions within the mill.
(iv) The separator blades were not being effectively utilised.
(v) The flow pattern did not change significantly within the operating flow range.

The following series of tests was based on the information gained from the pitot traverses. A series of cones (as shown in Figure 5.16) was installed in the model and the flow observed in certain areas (due to the difficulty of inserting a pitot no pitot readings were taken). The result was an improvement in flow at the throat and a reduced Coanda effect.

In order to assess the probability of particle entrainment in the dead zone between the mill body and the inserted cone at the enlargement of the mill body from point A upwards (see Figure 5.16), sand was then introduced as a feed into the model. It was found by collecting the sand trapped behind the insert at point A that approximately 10% of the mass had recirculated despite the fact that the velocity of water through

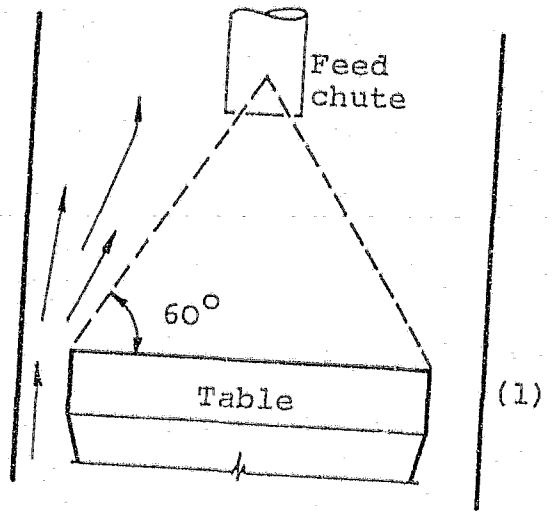


FIGURE 5.14: Dead space above table

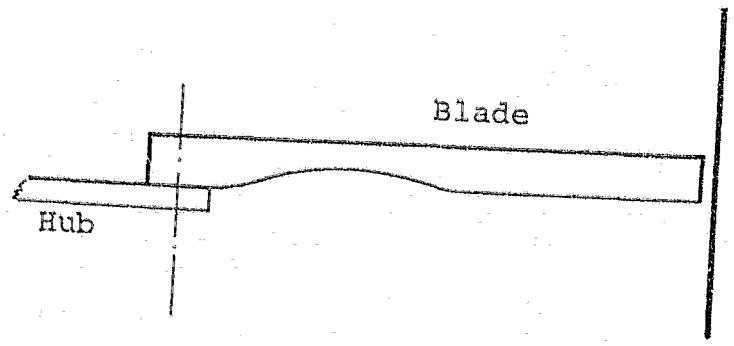


FIGURE 5.15: Separator blade wear

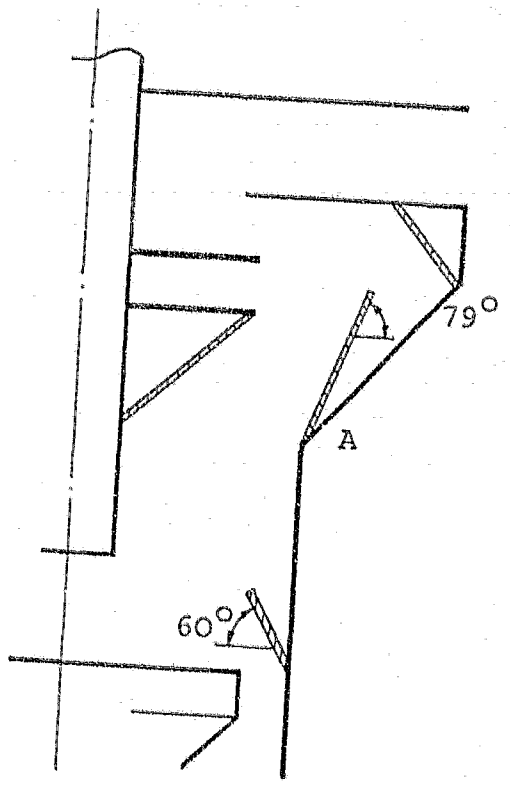


FIGURE 5.16: Test cone inserts

the separator was higher than the free fall velocity by a factor of approximatley 14.

This pointed to the fact that natural separation was taking place without the aid of the separtor and that if this oversize material could be channelled back onto the table without building up in the reverse flow zone, then the load in the air zone would be considerably less.

5.6 SLICE MODEL TESTS

It was realised that to investigate the various configurations within the mill, a simplified model would be required in which quick changes could be brought about, and in which the flow pattern could be easily observed. For this purpose it was decided to use a slice model.

This model was made out of two sheets of 230 x 510 x 6 mm clear perspex mounted at an angle of 3^{o} to each other. The mill profile, tc a scale of 1/8, was milled out of one of the sheets of perspex, and inserts for separator discs, roll covers and other modifications made. To remove the inserts, the top perspex sheet was able to be unscrewed from the bottom sheet and the inserts taken out of their slotted positions and replaced by blanks. 3 mm brass screws and G clamps ensured that no water leaked past the inserts which thus provided a good seal between top and bottom sheets.

The model was mounted on a hydraulic bench which incorporated a weigh tank and a sump. A pump circulated the water through the model via a 20 mm hose and regulating valve. The water entered the model through the throat, or louvre, and left at the mill outlet on its way, via a hose, to the sump (Figure 5.17).

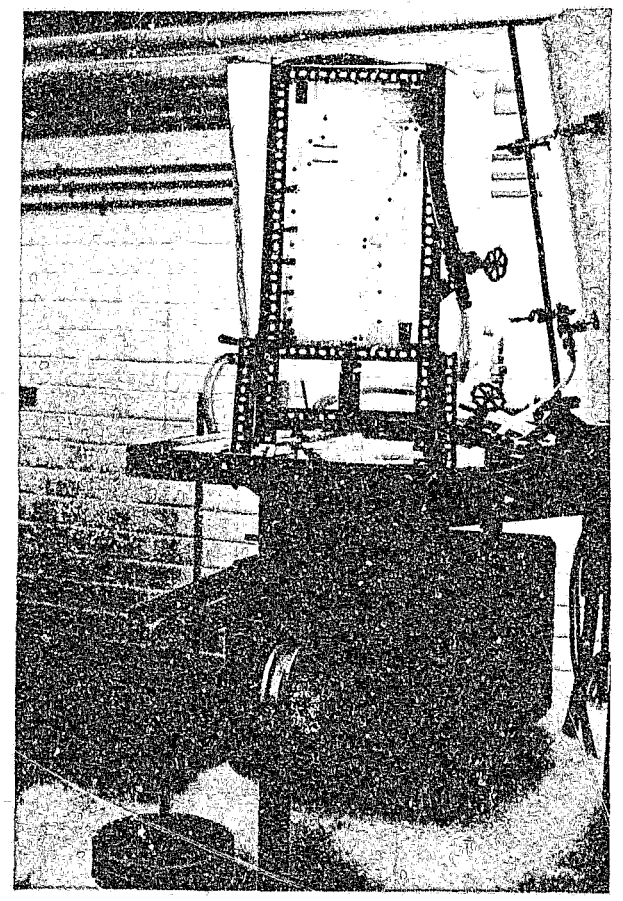


FIGURE 5.17: The slice model mounted on the hydraulic bench

A few packets of washing detergent and green ink were added to the water in the sump and this mixture was pumped through the model in an aerated form. To achieve this, a 6 mm compressed air line was connected to the circuit just before the regulating valve.

A 1000 W Sylvania light was mounted behind the model and its light diffused by hanging tracing paper between it and the model. This enabled one to see the flow patterns in the model clearly when viewing from the opposite side, since any disturbance in the flow in the model caused more intense foaming at the point of turbulence. Various photographs of the different flow patterns were then taken.

5.7 JET ATTACHMENT ABOVE THE THROAT

The slice model and the 1/6 water scale model both showed the Coanda effect above the throat. Sawyer (B13) has analysed the re-attachment of a jet both flowing parallel to a flat plate and inclined to the plate. His analysis agrees well with the measurements of Bourque, and of Miller and Comings (B13). Briefly, the notation for the jet was as shown in Figures 5.18 to 5.21. It will be seen that the re-attachment point moves further downstream as the angle increases, as would be expected.

The l/t ratio for the mill is in the order of 10 (for a condition where the re-attachment point is past the point A of body divergence); this corresponds to a ject angle of approximately 30^{o} and since it was not possible to move the existing throat inboard, i.e.

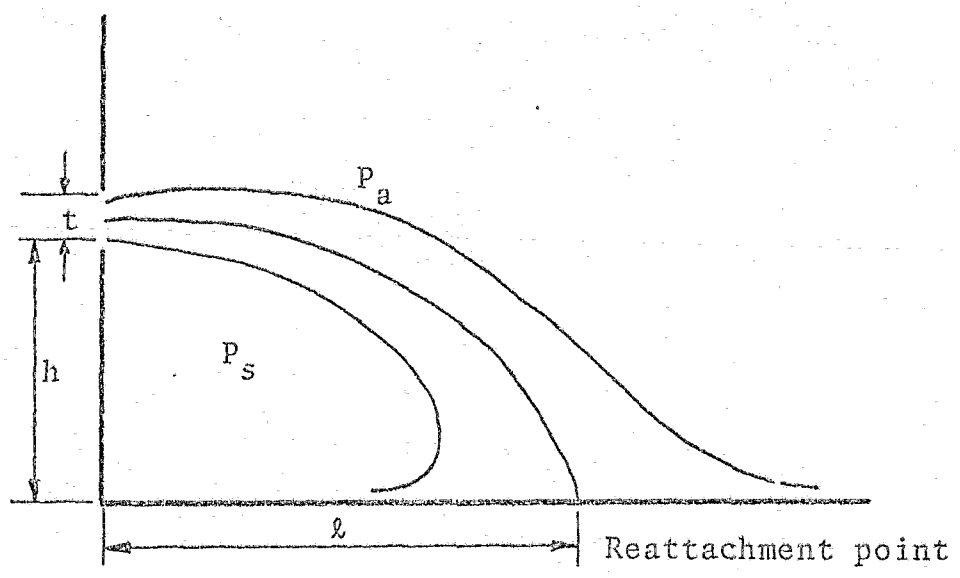


FIGURE 5.18:

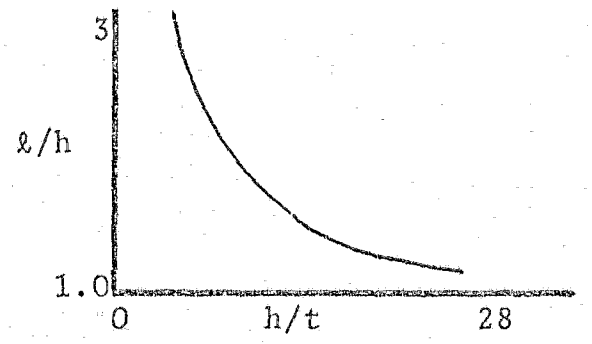


FIGURE 5.19:

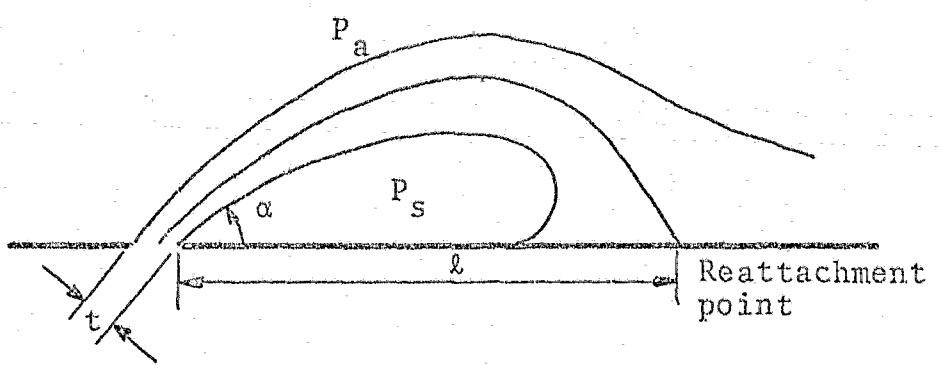
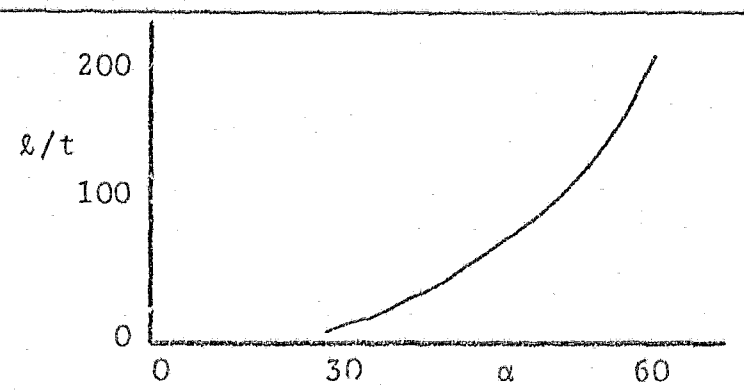


FIGURE 5.20:



FIGURES 5.18 to 5.21: Jet attachment data (from B 13)

increase the h/t ratio, the slice model throat cones were designed to make possible various jet angles to avoid the Coanda effect.

5.8 RESULTS

The model was constructed so that various geometries within the mill could be altered. These involved (i) the separator hub discs, and (ii) the recess behind the rolls (which was not considered in the perspex 1/6th scale model). The effects of coal flow across the table and particle recirculation in the separator zone were not simulated. The mill outlet was taken as discharging as shown although this pattern would change for the opposite side of the mill since the discharge is not symmetrical around the mill top. The effect of swirl flow due to the louvre inclination and separator rotation were also not amenable to simulation in this model. In addition to the perspex inserts in the model, use was made of plasticine to form various boundaries within the model. Although a number of configurations were tested, it was not assumed that these would all be practically acceptable from the point of view of cost and possible wear. The main aim was merely to observe the flows - irrespective of other considerations.

FIGURES 5.22 - 5.39: Slice Model Visualisation Results

FIGURES 5.22 TO 5.30

These show the flow patterns with various configurations of separator blade hubs and roll cover recess. The Coanda effect can be clearly seen as well as the flow breakaway at the conical divergence. There appears to be a narrow flow area through the blades which confirms the previous pitot traverse results. Figure 5.29 indicates flow across about 78% of the separator radius, as compared with 80% in the traverse results.

There is also a recirculation within the roll cover, although with the roll casting and assembly in place, there will be much less free space behind the roll. The fact that corresponding wear does take place on the prototype confirms this observation.

Another feature brought out by these photographs is the abundance of dead space, e.g. in corners and between separator disc hubs. All of these areas will be high wear zones if particle recirculation takes place.

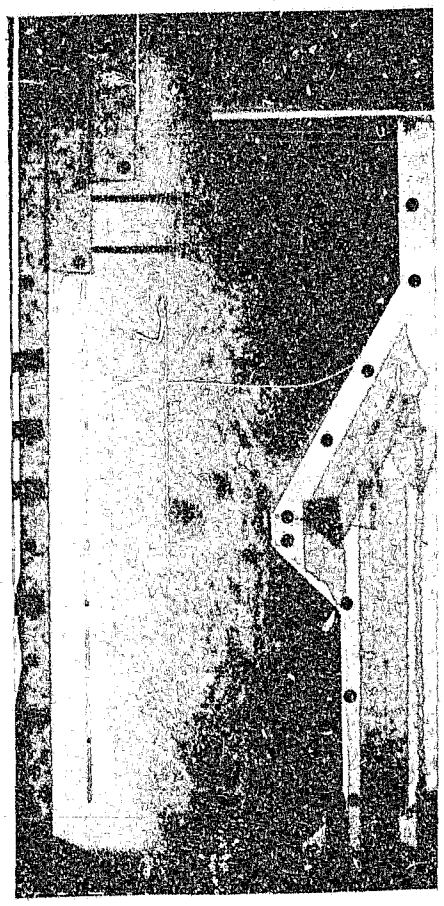


FIGURE 5.22

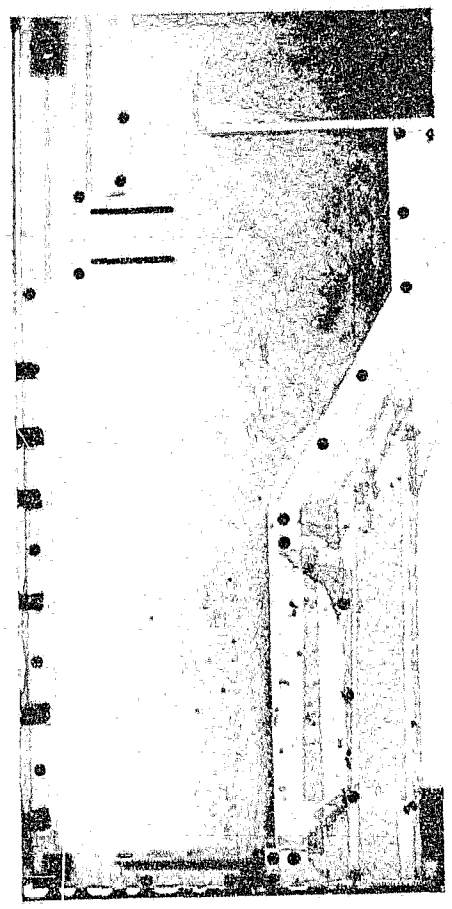


FIGURE 5.23

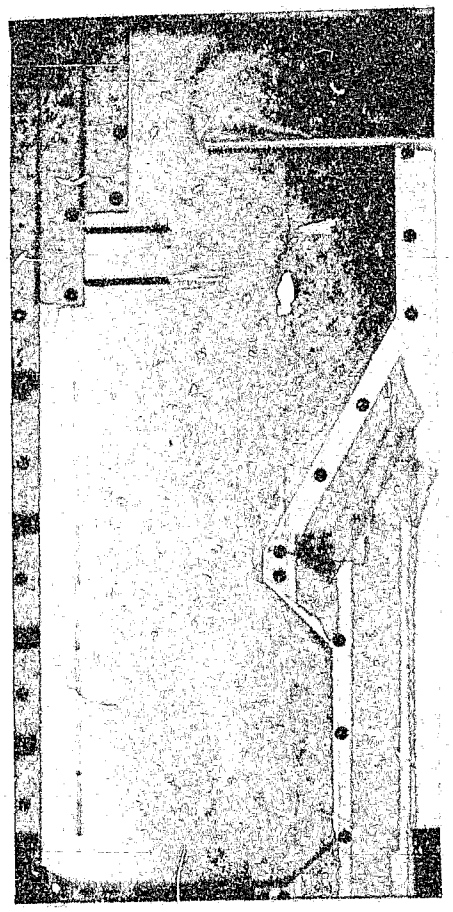


FIGURE 5.24

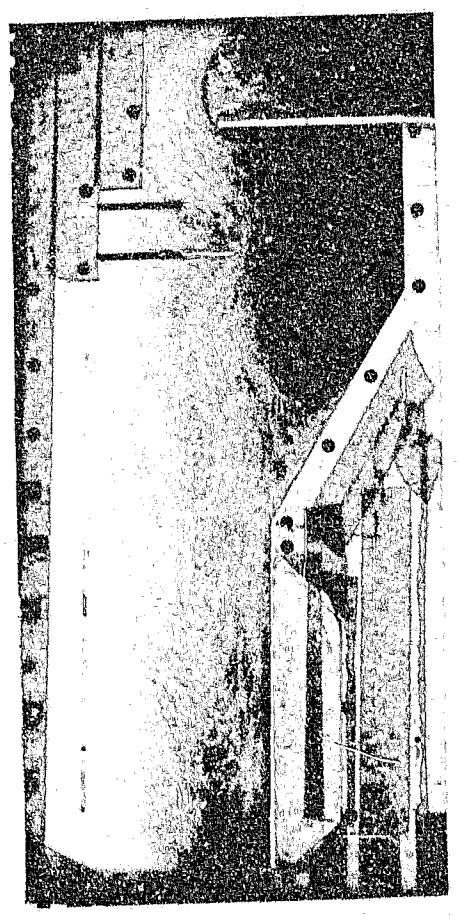


FIGURE 5.25

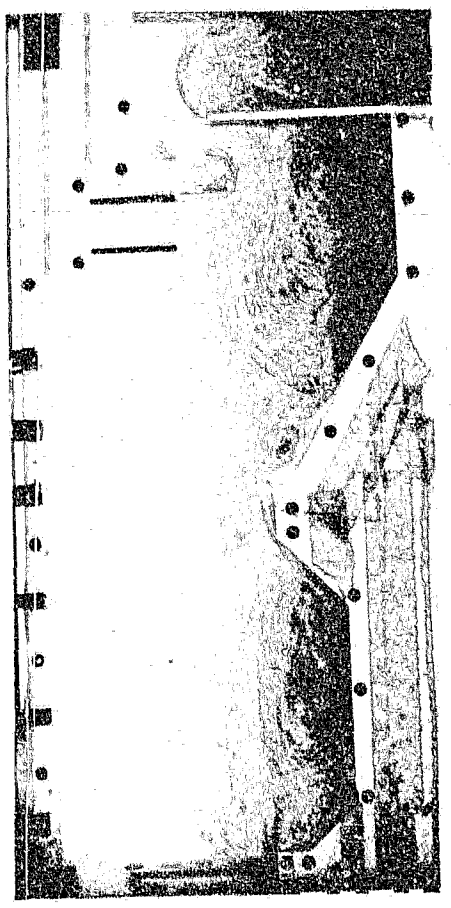


FIGURE 5.26

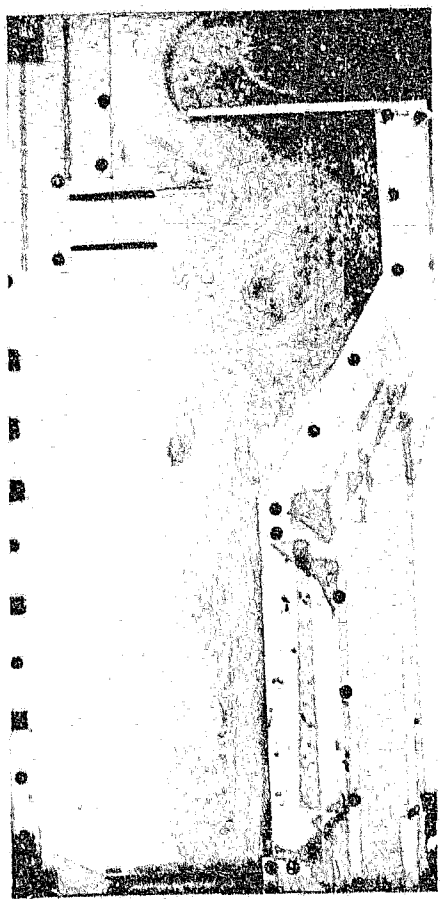


FIGURE 5.27

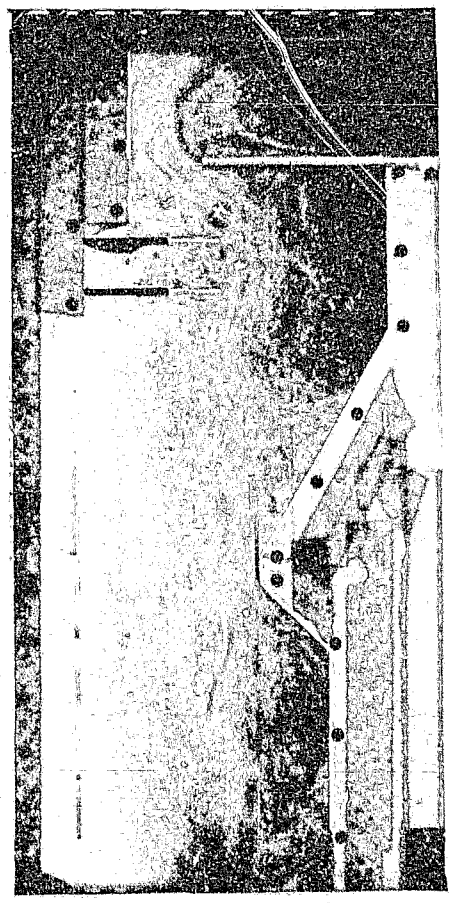


FIGURE 5.28

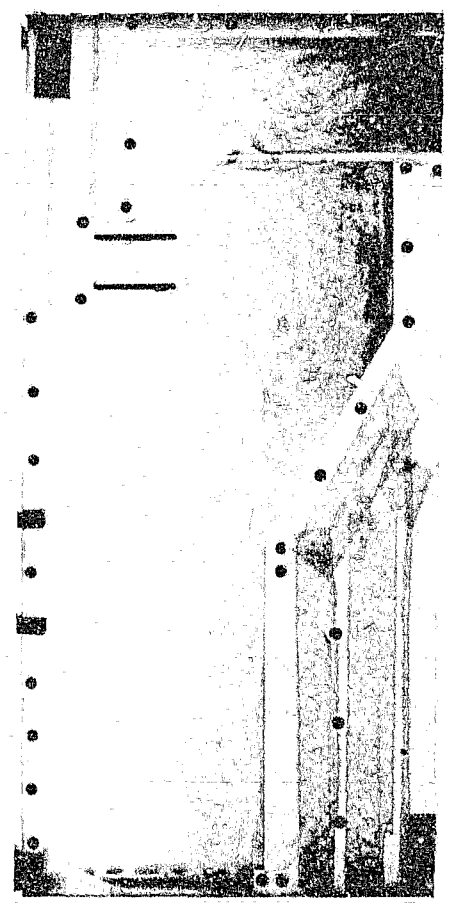


FIGURE 5.29

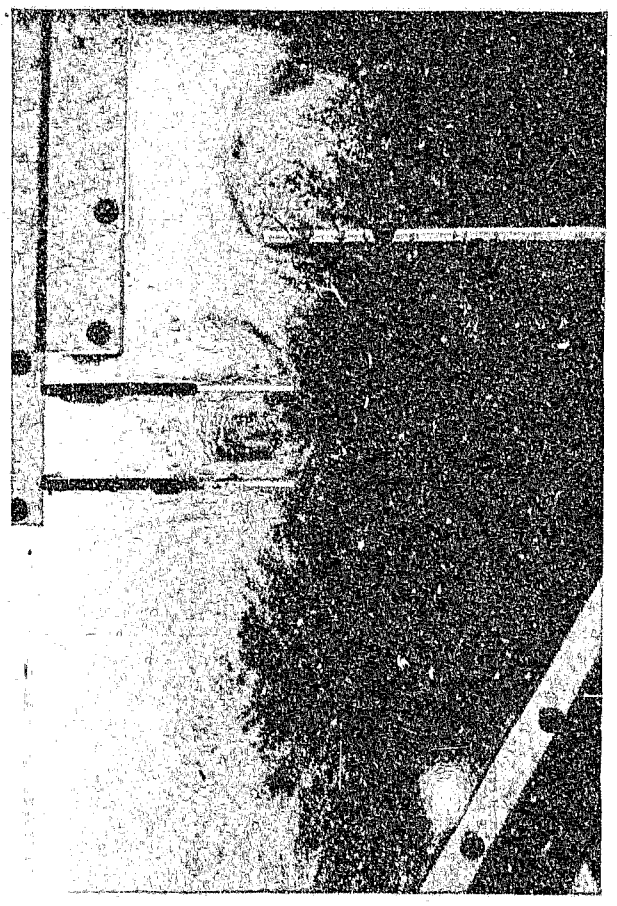


FIGURE 5.30

FIGURES 5.31 TO 5.36

In order to minimise the Coanda effect, the effect of various values of throat jet angle was investigated, the angles being $\alpha = 10^{o}$, 22^{o} and 28^{o} to the vertical - the latter corresponding to the cone angle of the insert above the throat of the 1/6th scale perspex model. At jet angle $\alpha = 10^{o}$, the jet attaches itself within an 1/t range of 6 to 8. From the curves given by Sawyer (B13) this is also obvious. At $\alpha = 22^{o}$, there appears to be no attachment to the vertical wall and the recirculating zone behind the throat (roll cover) is less intense.

At $\alpha = 28^{o}$, the nozzle would appear to give high particle impact on the central feed chute but at the same time allowing heavier particles to fall back onto the table for further grinding.

As far as the flow straighteners are concerned, the effect of these must be viewed more from an experimental rather than practical point of view. It is possible to get reverse flow on the conical sections (Figure 5.34) at discharge at the divergence. Whether particles could cross the high velocity flow stream onto the table is debatable.

The elimination of the dead spaces has had a streamlining effect on the flow and should be beneficial from a pressure drop and wear point of view.

The flow pattern through the separator is slightly wider with the 22^{o} jet and the insert configuration of Figure 5.35. By restricting the turbulence region, a wider band is obtained.

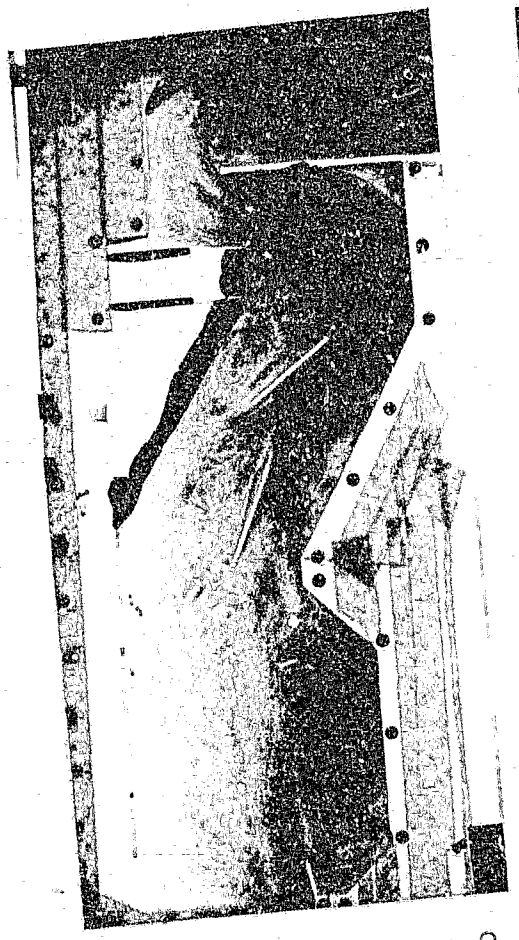


FIGURE 5.31 $\alpha = 10^{o}$



FIGURE 5.32 $\alpha = 10^{o}$

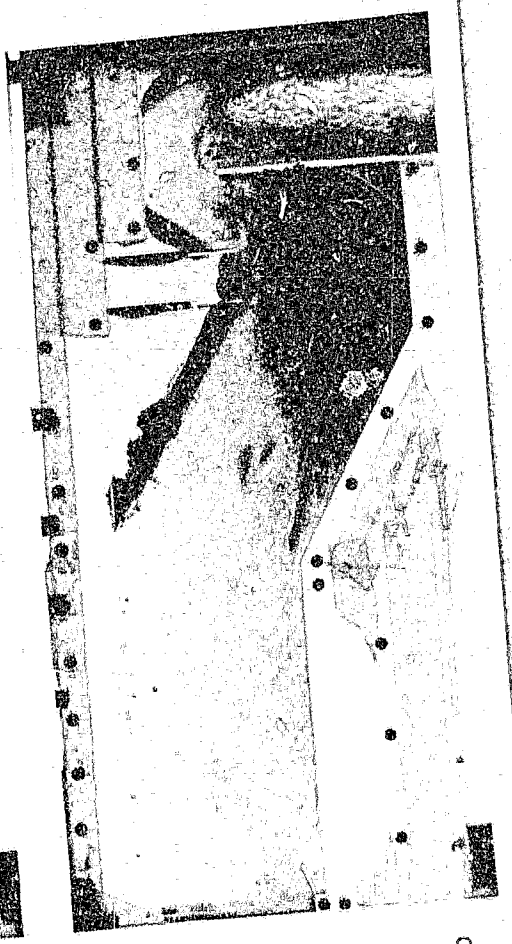


FIGURE 5.33 $\alpha = 22^{o}$

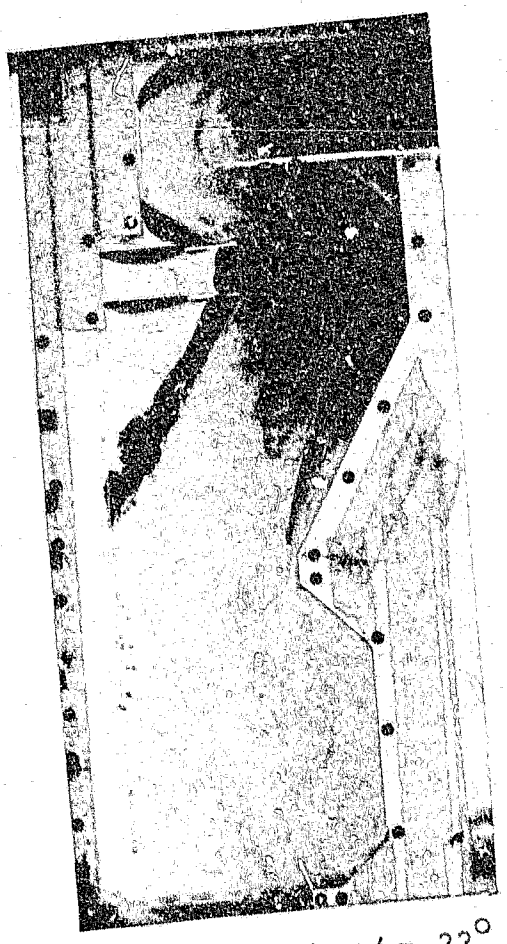


FIGURE 5.34 $\alpha = 22^{o}$



FIGURE 5.35 $\alpha = 28^{o}$

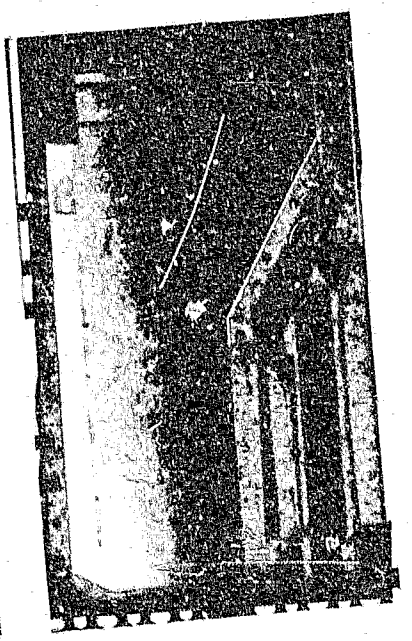


FIGURE 5.36

FIGURES 5.37 TO 5.39

Further internal configurations were tested as shown here. A static classifier shape (Figure 5.37) will return oversize particles to the centre of the table (which is ideal). By correct positioning, smaller turbulence zones can be obtained. Note that the 22^{o} jet is used here.

By lowering the cone (Figure 5.39) and inserting a flow straightener (Figure 5.38), it is possible to present a wider flow area to the separator. The problem of returning the oversize still remains.

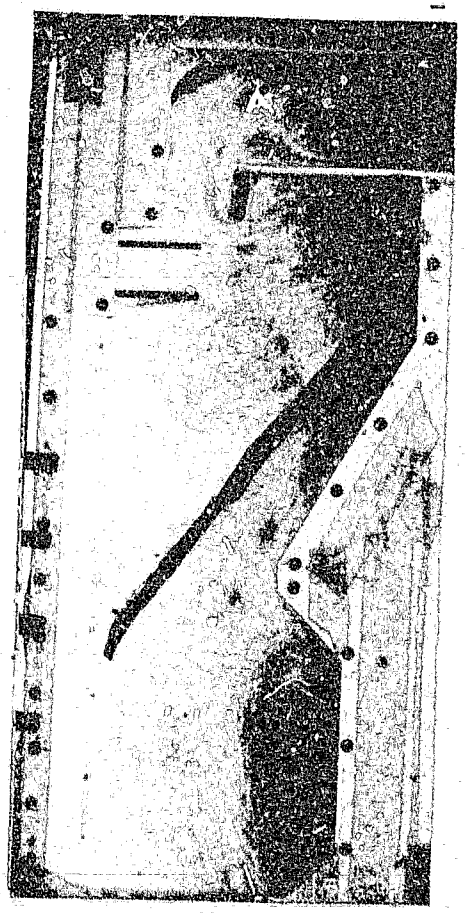


FIGURE 5.37 $\alpha = 22^{\circ}$

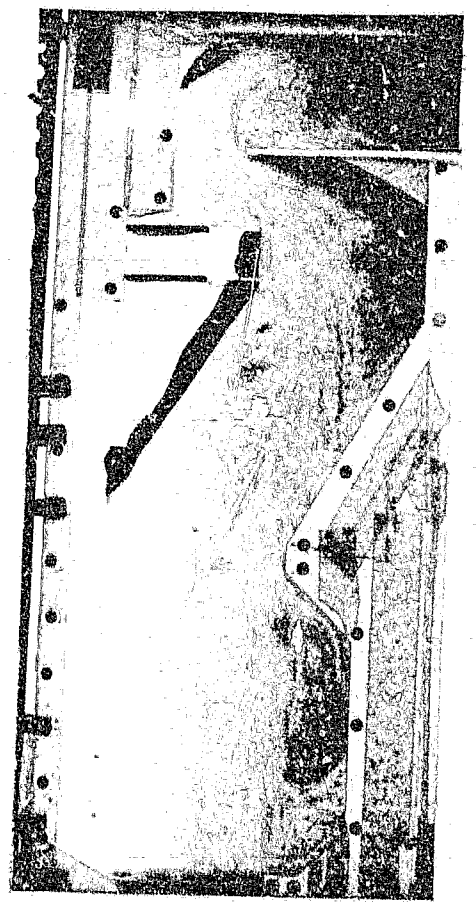


FIGURE 5.38

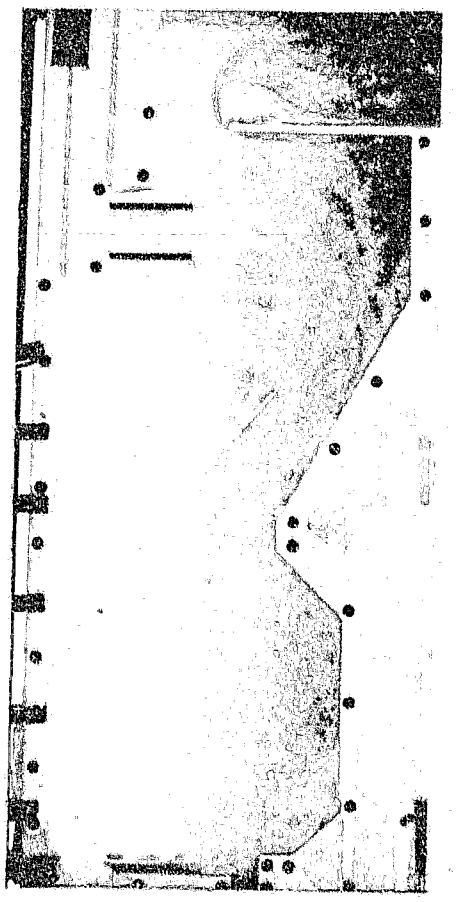


FIGURE 5.39

5.9 CONCLUSIONS

1. The slice model proved a most adaptable method of visualising this type of model flow as far as interchangeability of configurations and ease of recording results was concerned.

2. The existence of a Coanda effect and a recirculating zone at the body divergence section were confirmed. By directing the throat jet inwards at 22^{o} to 28^{o} the Coanda effect could be eliminated and a slightly wider flow area presented to the separator.

3. Corners and dead spaces should be avoided since these give rise to vortices and resultant high wear rates. A high recirculating area appeared to exist behind the throat in the roll cover recess. (A bypass type louvre, as discussed in Chapter 7, would suppress this effect).

4. Flow straighteners appeared to give wider distribution across the separator, but the practical implications of such installations would be high wear on these items.

5 Returning the separator oversize via an inner cone (Figure 5.37) would prevent the high recirculation evident in the separator region and, in conjunction with the diverted throat, enable oversize particles to fall back onto the table through a low velocity zone.

CHAPTER 6

FLUIDISED BED TESTS

6.0 EARLY DEVELOPMENT OF FLUIDIZATION TECHNIQUES

Fluidization in its crudest form has been known for over a century, but it has only been during the last few decades that it has found widespread industrial and scientific use. The first large scale use of fluidization in the United States dates to 1940 when the petroleum industry started intense research into catalytic cracking of oil vapours using this new process. The older method had been to regenerate a fixed bed by a system of back-washing developed in 1937. In order to reduce the complexity of the older process, the fluidized bed concept was then developed, whereby the gas was blown through the bed at a velocity high enough to keep it in suspended motion. The immediate advantages of this process were:

- Temperature control of the cracking process: owing to the intense agitation produced, localised high temperatures were minimised and the product was spread more evenly.

- Continuity of operation: the bed behaved like a liquid, making additions and withdrawals easy, whilst ensuring good mixing almost immediately.

- Good heat transfer: a large surface area in good contact with the catalyst was readily available, and although transfer coefficients were not as high, the transfer rates were better than had previously been achieved.

- Catalysis: a definite level of catalytic activity could be maintained because a catalyst could be added or withdrawn continuously.

The disadvantages were:

- Higher pressure drop: since the mass of the bed was supported this led to a higher pressure drop than for kilns or trays.

- If a uniform temperature gradient was required through the bed, a fluidized bed was unsuitable.

- Attrition of the bed particles led to carry-over and subsequent recovery. Consequently, a recovery vessel usually had to be included in the system.

- Fluidization was only possible if no liquids or slag formed during process reactions. Thus hydrocarbon synthesis could not be handled due to wax formation.

Although it would appear that the principle of fluidization has revolutionised the petroleum industry, its uses have been important in many other industrial and scientific developments, especially in the pulverised fuel application, and in the mechanical handling of powders and dilute phase material. The Airslide conveyor is one of the many patented devices which followed on the successful use of a fluid bed; another is the air-activated blender which incorporates a stirrer in a fluidized bed.

6.1 APPLICATION TO GRINDING

The grinding mills used in modern power stations are operated on similar lines to a chemical fluidized reactor, in that they are also air-swept, the difference being that the amount of carry-over in the former is considerably

higher. However, the principles involved are the same, namely, heat transfer occurs and there is continuity of operation and particle size separation.

(i) Heat Transfer: Since the coal is not always dry or even of constant moisture content, it has to be dried out considerably before combustion will be stable and the pulverised coal will not agglomerate and form hard deposits. The fluidising air is therefore preheated before entering the mill so that as the coal is crushed on the mill table and swept up, it is simultaneously dried. Although the moisture will still go into the furnace, combustion efficiency will be improved both by preheating the pulverised coal and by drying it.

(ii) Continuity of operation: The furnace is designed to burn a certain size range of particle continuously to maintain stable combustion, and to give good burnout efficiency, and hence good boiler efficiency. The coal is therefore fed continuously into the mill and an equal amount swept out in a pulverised state.

(iii) Particle size separation: The largest size swept into the furnace from the mill can theoretically be determined from free-fall velocity considerations if all the particles are of the same density and shape. In practice this does not happen and localised high velocities in the system pick up particles larger than desired for combustion. The design of the system therefore requires a configuration which will as far as possible utilise the particle cut-off size for a particular air flow; this size is higher than the limiting size for combustion since system resistance has to be over-

come downstream of the mill, thus necessitating higher air velocities in the mill. For this reason mills have a classifying circuit which returns the oversize particles for further grinding.

Investigators have tackled many aspects of a fluid bed and several well established formulae have been used to predict pressure drops, velocity relationships and carry-over from mixed beds. An important point about all these equations is their unpredictability when applied to systems handling unusual shapes and sizes even when so-called shape factors have been applied.

Two phenomena for which there has yet been no satisfactory explanation are channelling and slugging; these can cause serious problems in plant processes since by their existence they negate the advantages of a fluid bed as explained previously. Channelling occurs when the gas passed through the bed along a preferred path and its effect is self-propagating. It is usually caused by a poor fluidizing medium distribution. Slugging usually occurs at the onset of fluidization and the whole bed seems to bubble, with slugs of material and gas alternately rising and breaking the fluid-solid interface surface. Both these phenomena seem to be present in gas-solid systems to a greater extent than in liquid-solid ones. For example, Leva (F5) found that 36 to 72 mesh coal powder started slugging at 0.19 m/s when fluidized with air in a 64 mm tube.

6.2 MECHANISM OF OPERATION OF FLUID BED

Considerable experimental data is available for a wide variety of fluidized beds, the main investigations being into the influence of pressure drops, fluid velocity fraction voids and particle shape factors. Other pheno-

mena such as heat transfer and mass transfer will not be dealt with although they are of importance to the chemical industry.

When a screen-supported bed of particles in a tube is subjected to an upward flow of fluid at gradually increasing velocity, the following is observed:

(i) The bed remains stationary, with an increase in pressure drop across the bed as the velocity increases (Figure 6.1). Various authors have reported that the bed adjusts to the assemblage with the lowest resistance, ie, cubic, without becoming fluidized until the maximum allowable void fraction exists. At this point the bed has the appearance of a boiling viscous fluid and the pressure drop across the bed will be caused by the bed mass plus that due to the empty tube friction (which will be small by comparison). Due to the static friction, and possibly electrostatic charges, the pressure drop/velocity curve displays hysteresis, but once the bed is fluidized beyond the "minimum fluidization" point, the pressure drop remains almost constant.

(ii) The bed continues to expand with increasing fluidizing velocity until the void fraction is 1.0, at which point the velocity of the fluid corresponds to the free-fall velocity of a single particle in the bed, and above which velocity the particles will be transported out of the fluidizing tube or chamber.

The three phases are therefore: (a) fixed bed; (b) minimum fluidization; and (c) expanded bed.

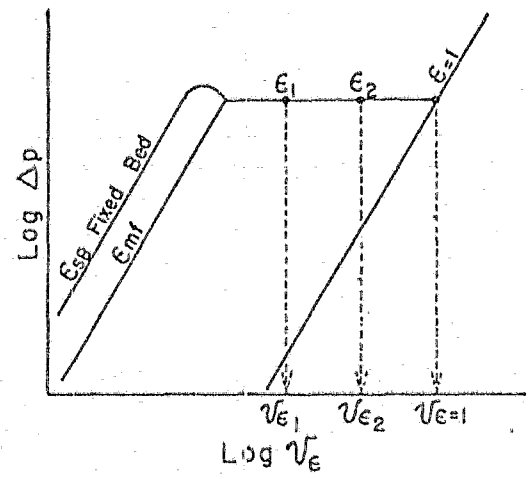


FIGURE 6.1: Typical representation of the fluidisation curve (from F7)

6.3 PARTICULATE AND AGGREGATIVE FLOW

The physical phenomena associated with the fluid flow passing through the bed have been described by various observers as resulting from a uniform expansion of the bed, allowing greater ease of passage of the fluid through the widening interstices, or the formation of bubbles rising through the bed analogous to bubbles rising in a liquid. These two forms of flow have been termed particulate and aggregative respectively. Particulate flow is common to solid-liquid systems whereas aggregative flow occurs mainly when gas is the fluidizing medium, although certain solid-liquid systems do display aggregative tendencies. As can be expected, the particulate form of flow has been studied more thoroughly due to ease of observation and it has resulted in more rigid, or accurate, equations than the aggregative state.

6.4 DENSE AND DILUTE PHASES

If a bed is fluidized to a void fraction of 0.95 - 0.98 and particles are added to the bed from the top of the fluidizing tube, they will remain uniformly suspended in the bed until a stage is reached at which the bed concentration is such that the whole bed collapses to the bottom of the tube and behaves as a shallow dense bed. The concentration, or voidage, at which this occurs is a function of the particle-to-fluid density and particle size. Zenz (F7) explains the transition from dilute to dense phase as follows: any object submerged in a flowing fluid will generate a turbulent wake, the size of which will depend on the size and shape of the object and the properties of the fluid. It is also known that induced turbulence reduces the drag coefficient so that a high fluid velocity is required to keep the particle in suspension if turbu-

lence is induced on the upstream side. Suppose the particles are in a very dilute concentration 100 diameters apart with wakes of 20 diameters in length. By increasing the concentration, the distance between particles will decrease until the particles fall into each other's wake, thereby reducing their drag coefficient and requiring a higher velocity to keep them suspended. As the velocity remains constant, the bed will collapse to its dense phase.

6.5 FIXED BED

When a bed is prepared in a tube or container, the physical properties of the material will govern the behaviour of the bed when air is passed through it.

The pressure drop of a fluid through a length L of packed spheres is represented by

$$\frac{\Delta P}{L} = \frac{2 f \rho_f v_o^2}{d} \quad . . . . . (6.1)$$

where f, the friction factor, depends on Re, and voidage ε is defined as

$$\varepsilon = 1 - \frac{M_s}{A L (\rho_s - \rho_f)}$$

ε is therefore the fraction of volume occupied by the fluid. Blake (F6) proposed the following relationship for fixed beds:

$$f \propto \frac{(1 - \varepsilon)^{3-n}}{\varepsilon^3} / Re^{2-n}$$

At low values of Re, n = 1, so where ΔP does not depend on ρ_f, f may be expected to vary as $(1 - \varepsilon)^2/\varepsilon^3$ Re and at high Re (n = 2), where ρ_f is unimportant, as $(1 - \varepsilon)/\varepsilon^3$. Experimentally, the expression holds for low Re but not for high Re.

Carman (F6) studied low Re flow and found that

$$f = C(1 - \varepsilon)^2/\varepsilon^3 \, Re$$

with about 10% of scatter. This can be combined with equation (6.1) to give

$$\Delta P = \frac{2 C v_o L \mu (1 - \varepsilon)^2}{d^2 \varepsilon^3} \quad . \quad . \quad . \quad . \quad . \quad . \quad . \quad (6.2)$$

Values of 2 C have been reported as follows (F6):

Carman	878
Lewis et al	752
Bureau of Mines	976

Oman and Watson (F6) experimented with a wide range of materials and shapes of beds, both loosely and closely packed. They found a 25% increase in f in going from a loose to a dense packing arrangement when the size and shape were uniform.

Ergin (F6) proposed the equation

$$\frac{\Delta P}{L} = \frac{2401 \quad (1 - \varepsilon)^2}{\varepsilon^3} \cdot \frac{\mu v_o}{d^2} + 28 \left(\frac{1 - \varepsilon}{\varepsilon^3}\right) \frac{G v_o}{d}$$

This accounts for the total energy as being equal to the sum of the viscous energy loss (first term on right hand side) and kinetic energy loss (second term).

6.6 MINIMUM FLUIDIZATION

By the definition of voidage ε, the minimum fluidization voidage ε_{mf} is given by

$$\varepsilon_{mf} = 1 - \frac{M_s}{A\, L_{mf}\, (\rho_s - \rho_f)}$$

Typical values are given in Figure 6.2.

Also

$$\Delta P = L_{mf}\, (1 - \varepsilon_{mf})\, (\rho_s - \rho_f)\, g \quad . \quad . \quad . \quad . \quad . \quad (6.3)$$

From an operational point of view, it is important to establish the system parameters at this point - in the mill application it would represent the point where rejection could begin if all the particles were similar. ε_{mf} will thus be related to fluidizing velocity, particle size and density. Leva (F6) gives the following equation based on equation (6.3) and the fixed bed pressure drop equation:

$$\Delta P = \frac{2\, f_m\, G^2\, L\, (1 - \varepsilon)^{3-n}}{d\, \phi_s^{\,3-n}\, \varepsilon^3\, \rho_f} \quad . \quad . \quad . \quad . \quad . \quad . \quad (6.4)$$

$$\therefore\ G_{mf}^2 = \frac{d\, g\, (\rho_s - \rho_f)\, \varepsilon_{mf}^3\, \phi_s^{\,3-n}\, \rho_f}{2\, f_m\, (1 - \varepsilon_{mf})^{2-n}} \quad . \quad . \quad . \quad (6.5)$$

For Re $<$ 10, $f_m = 100/Re$ and $n = 1$, and since $G_{mf} = \rho_s\, v_o$,

$$G_{mf} = \frac{0{,}0?4\, d^2\, g\, \rho_f\, (\rho_s - \rho_f)\, \phi_s^{\,2}\, \varepsilon_{mf}^{\,3}}{\mu\, (1 - \varepsilon_{mf})} \quad . \quad . \quad . \quad (6.6)$$

Using data correlation for Re $<$ 5,0 and the correlation of Figure 6.3, Leva (F6) eliminated ϕ_s and ε_{mf} from equation (6.6) above to give

$$G_{mf} = \frac{3357\, d^{1.82}}{\mu^{0.88}} \left[\rho_f\, (\rho_s - \rho_f)\right]^{0.94} \quad . \quad . \quad . \quad (6.7)$$

Miller and Logwinuk (F6) derived a slightly different form by dimensional analysis:

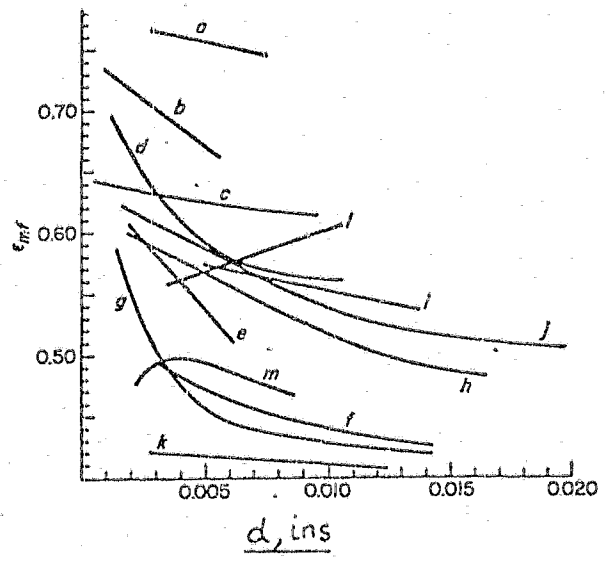


FIGURE 6.2: Values of ε_{mf} in relation to d. (a) Soft brick; (b) Absorption carbon; (c) Broken Raschig rings; (d) Coal and glass powder; (e) Carborundum; (f) Sand; (g) Round sand; (h) Sharp sand; (i) Fischer-Tropsch catalyst; (j) Anthracite coal; (k) Mixed round sand; (l) Coke; (m) Carborundum. (from F6)

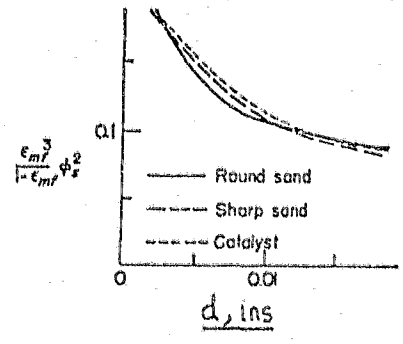


FIGURE 6.3: Correlation between the product of the voidage function and the square of the shape factor with particle diameter (from F6)

$$G_{mf} = \frac{0.0298\ d^2\ (\rho_s - \rho_f)^{0.9}\ \rho_f^{1.1}\ g}{\mu} \quad . \quad . \quad . \quad . \quad (6.8)$$

The Miller-Logwinuk equation is shown in relation to other equations in Figure 6.4. Wilhelm and Kwauk (F6) correlated their data by relating $K_{\Delta P}$ and $K_{\Delta\rho}$ to Re:

$$K_{\Delta P} = \frac{d^3\ \rho_f\ \Delta P}{2\ \mu^2\ L_{mf}}$$

$$K_{\Delta\rho} = \frac{d^3\ g\ \rho_f\ (\rho_s - \rho_f)}{2\ \mu^2}$$

A set of curves (Figure 6.5) enables G_{mf} to be found, point B being the minimum fluidization point. Finally, a more recent correlation due to Bourgeois and Grenier (F4) incorporates the Fluidization Number F_n (= $2\ K_{\Delta\rho}$):

$$F_n = \frac{g\ \rho_f\ (\rho_s - \rho_f)\ d^3}{\mu^2} \quad . \quad . \quad . \quad . \quad . \quad . \quad . \quad . \quad (6.9)$$

For air the following relationships were determined:

$$R = \frac{Re_t}{Re_{mf}} = 26.6 - 2.3 \log F_n \text{ for } 4 \times 10^4 < F_n < 8 \times 10^6$$

$$R = 10.8 \text{ for } F_n > 8 \times 10^6$$

The equations for water are:

$$\text{For } 50 < F_n < 2 \times 10^4,\ R = 132.8 - 47.7 \log F_n + 4.6\ (\log F_n)^2$$

$$\text{For } 2 \times 10^4 < F_n < 10^6,\ R = 26.0 - 2.7 \log F_n$$

$$\text{For } 10^6 < F_n,\ R = 9.0$$

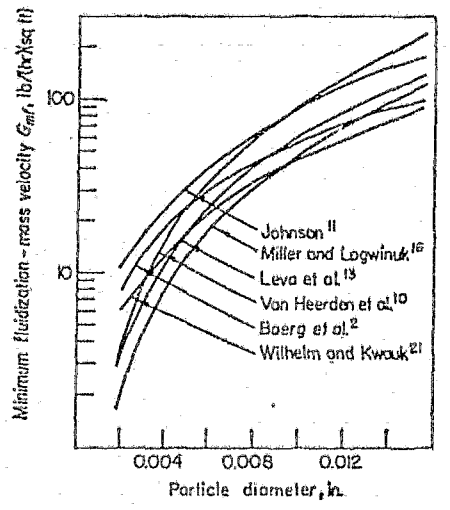


FIGURE 6.4: Comparison of correlations for predicting onset of fluidisation (from F6)

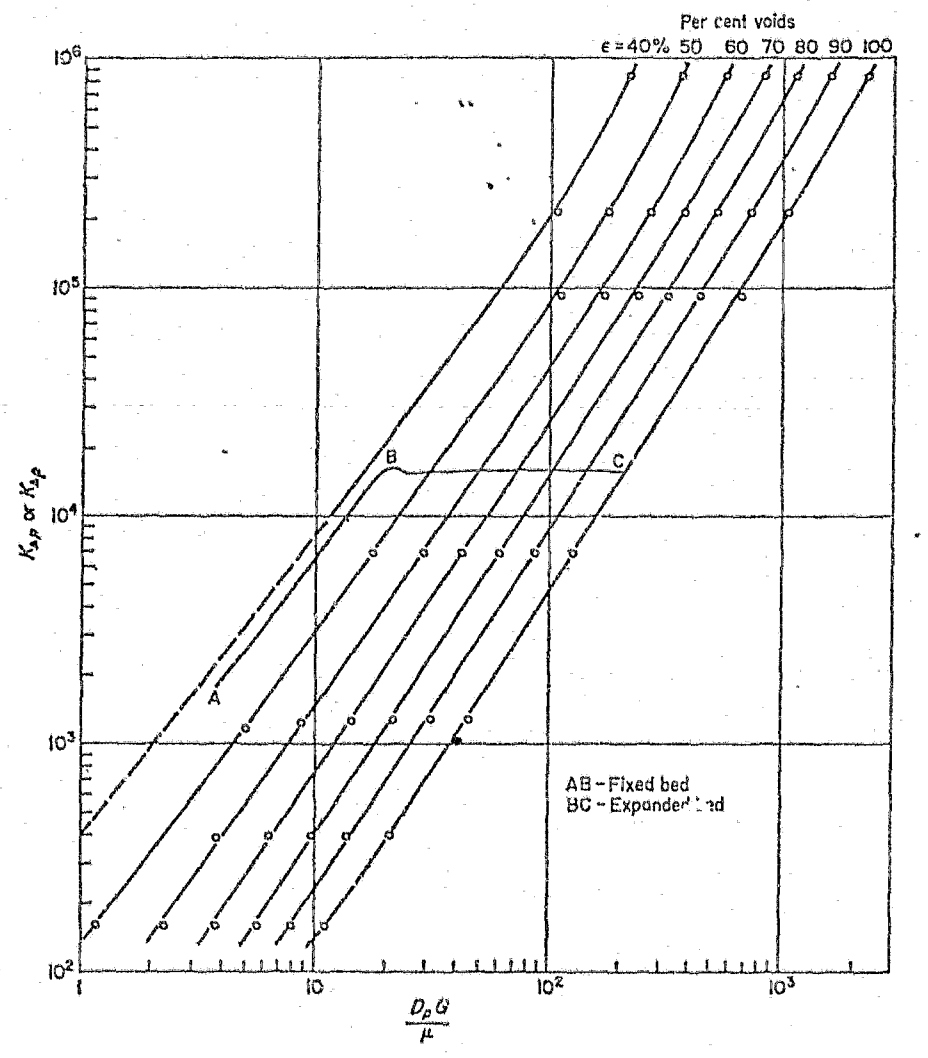


FIGURE 6.5: The generalised correlation of Wilhelm and Kwauk for predicting the onset of fluidisation and bed expansion (from F6)

6.7 EXPANDED BED

Once the initial bed movement has taken place, the bed expands upwards until the voidage approaches unity. Slugging phenomena as previously discussed can take place, but considering a uniform expansion, the fluidization curve appears as shown in Figure 6.1. Here ΔP is the pressure drop across the expanded bed.

6.7.1 Solid-Liquid Systems

For expansion in the laminar range the Hawksley-Vand equation has been confirmed by Harratty and Bandukwala (F4) and the Brinkman equation (F6) has experimental support. These equations are:

Hawksley-Vand: $$v_o/v_{\varepsilon=1} = \varepsilon^2 e^{-2.5(1-\varepsilon)/[1-(39/64)(1-\varepsilon)]} \quad . \quad . \quad . \quad . \quad (6.10)$$

Brinkman: $$v_o/v_{\varepsilon=1} = 1 + \frac{3}{4}(1-\varepsilon)\left[1 - \sqrt{\frac{8}{1-\varepsilon} - 3}\right] \quad . \quad . \quad . \quad . \quad (6.11)$$

Here v_o is the superficial velocity or the velocity of fluid in the tube, and $v_{\varepsilon=1}$ is the particle terminal velocity.

If equation (6.2) is applied in the expanded range, and replacing L by its equivalent $(1 - \varepsilon_{mf})/(1 - \varepsilon_o)$, and provided that no slugging occurs, we have

$$\Delta P = \frac{976\, G \mu \left[\frac{1 - \varepsilon_{mf}}{1 - \varepsilon_o}\right](1 - \varepsilon_o)^2}{d^2 \phi_s^2 \rho_f \varepsilon_o^3} \quad . \quad . \quad . \quad . \quad (6.12)$$

This equation can be tested by plotting Re against $(1-\varepsilon_o)/\varepsilon_o^3$. A log-log plot will yield a line of negative slope. Leva (F6) gives references which show general agreement with the above equation up to $\varepsilon = 0.80$, after which deviation occurs.

To predict transition and turbulent range expansion, Richardson and Zaki (F9) investigated fluidization and sedimentation data in the light of the following dimensionless variables:

$$\frac{v_f}{v_t} = F\left[\frac{d\, v_f\, \rho_f}{\mu}\,,\ \frac{d}{D_t}\,,\ \varepsilon\right] \qquad \ldots\ldots\ldots \quad (6.13)$$

By presenting the data in the form

$$\frac{v_f}{v_t} = \varepsilon^m\, F\left(\frac{d}{D_t}\,,\ \frac{d\, v_f\, \rho_f}{\mu}\right) \qquad \ldots\ldots\ldots \quad (6.14)$$

straight lines should emerge on a log-log plot of v_f vs ε.

Richardson and Zaki's equations give

$m = (4.35 + 17.5\ d/D_t)\ Re^{-0.03}$ for $0.2 < Re < 1$

$m = (4.45 + 18\ d/D_t)\ Re^{-0.1}$ for $1 < Re < 200$

$m = 4.45\ Re^{-0.1}$ for $200 < Re < 500$

$m = 2.39$ for $Re > 500$

Andrieu (F6) studied the effects of particle size on the slope m by specially prepared fluidizing sand mixtures. The coarser the mixture, ie, larger the average particle size, the lower the value of m.

6.7.2 Solid-Air Systems

These are more complex due to the slugging phenomena mentioned previously. The change in slope of m can be seen from Figure 6.6.

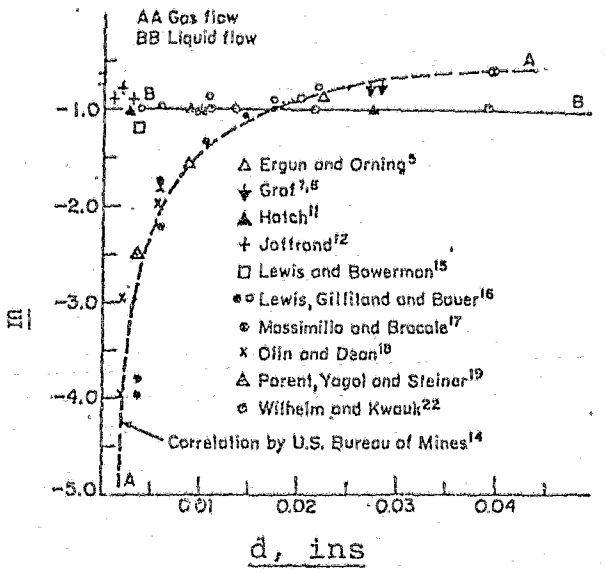


FIGURE 6.6: Slope values from gas- and liquid-fluidized data in relation to particle size (from F6)

6.8 EXPERIMENTAL APPARATUS

Basically the same apparatus was used for both air and water experiments. The equipment was readily available, having been used in previous laboratory tests.

6.8.1 Air Fluidization (Figure 6.7)

A 34 mm I.D. clear perspex tube 1 676 mm long was mounted on a metal pot base (which was half-filled with porcelain beads) which acted as a calming section for the incoming fluid. The top cover plate had a machined venturi type nozzle leading into the perspex tube, the latter being positioned and sealed with bolts and an O-ring on the lower flange of the tube. A 150 mesh phosphor-bronze

screen was also clamped in this flange to serve as a datum from which bed heights could be measured by means of a ruler clamped onto the tube. 36 pressure tappings were drilled into the tube, those numbered 1-24 being spaced 25 mm apart from the bottom and those numbered 25-36 being spaced 50 mm apart. Clear plastic tubing 1 mm I.D. was countersunk into the perspex and connected onto hyperdermic needles which were in turn connected onto a bank of inclined water manometers by 5 mm rubber tubing.

The fluidizing air was taken from the laboratory air main and controlled through a filter and regulating valve. The flow was measured by means of an orifice and a water manometer. Different sized orifice plates were used to obtain reasonable scale readings at low flows. Temperature and pressure were read upstream of the orifice and at the base of the particle bed.

6.8.2 Water Fluidization Figures 6.8 and 6.9)

The same pot base and perspex tube were used. These were mounted on a hydraulic bench incorporating a counter-balanced weigh-tank for measuring flows. Water was pumped from the sump through a regulating valve and into the pot base, and the flow measured either in the weigh-tank or in a graduated beaker over a timed interval. Water temperature was recorded at the tube outlet.

6.9 BED PREPARATION

The method of bed preparation is responsible for one of the important errors that occurs in measuring fixed bed parameters since the type of material, its shape and size are so widely varying. Smaller particles tend to pack more tightly, as do spherical materials, and external effects, such as electrostatic charges, tend to result

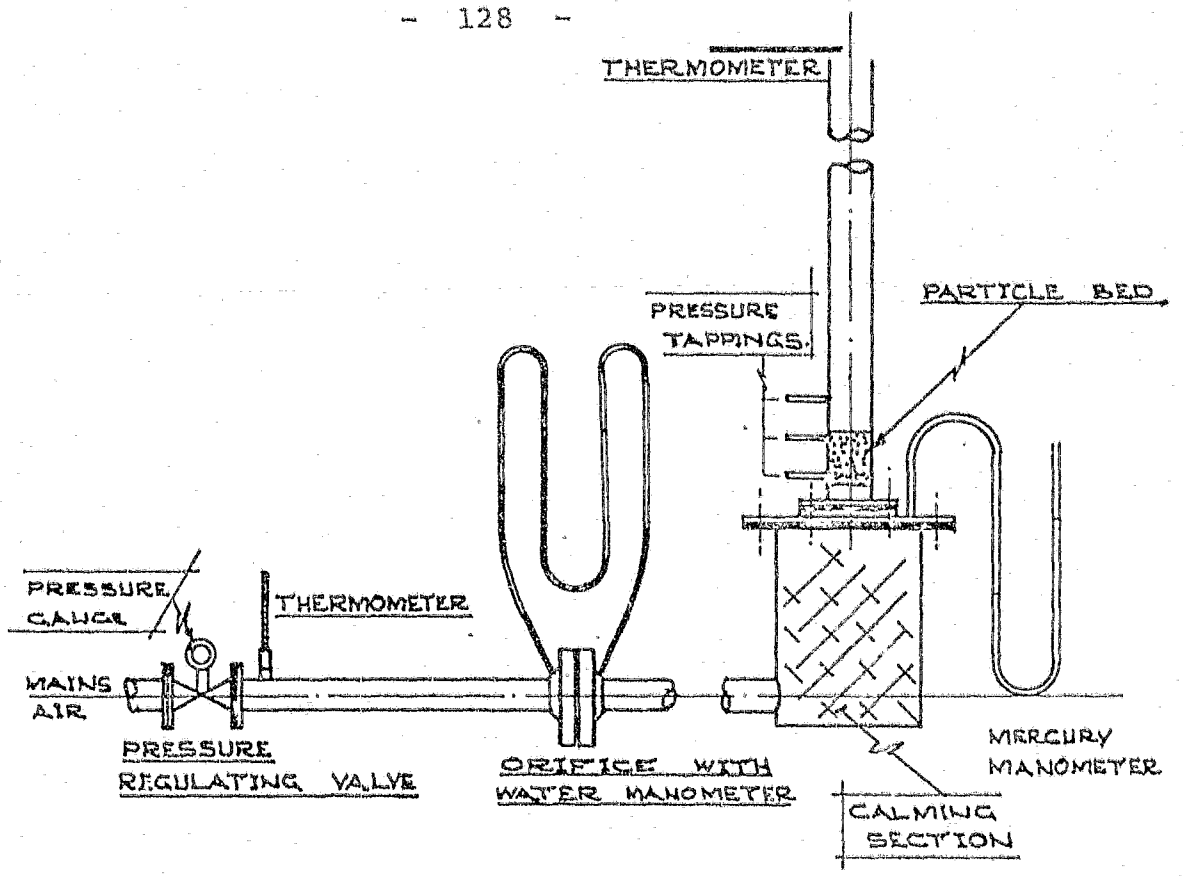


FIGURE 6.7: Air fluidization

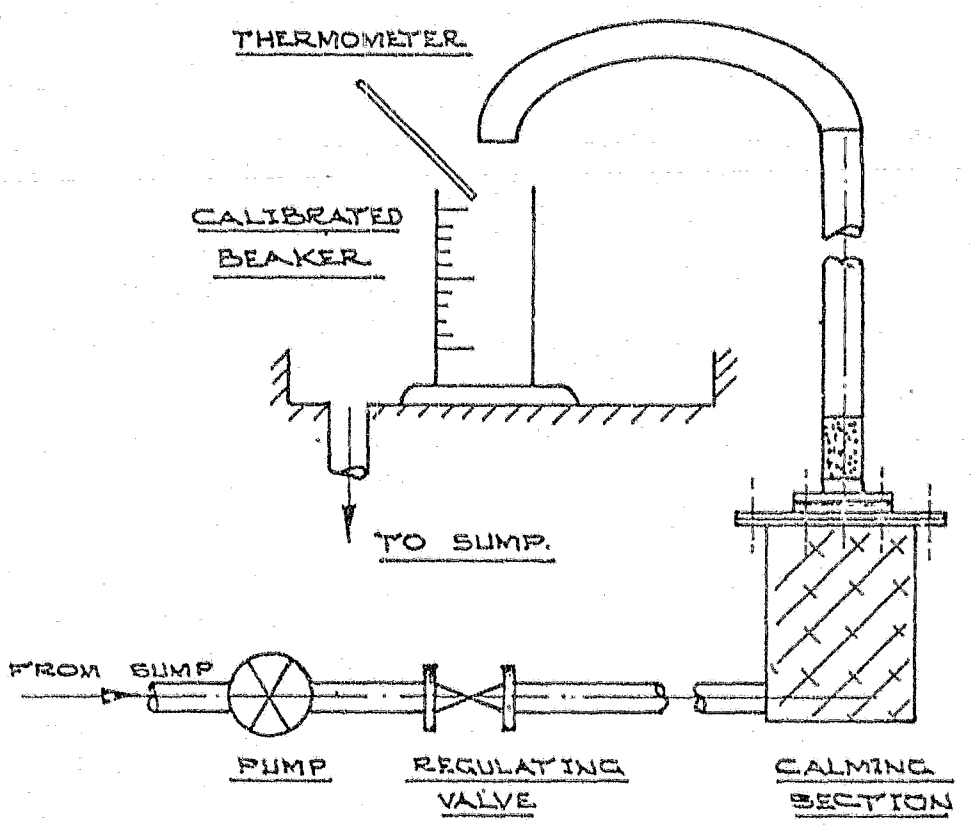


FIGURE 6.8: Water fluidization

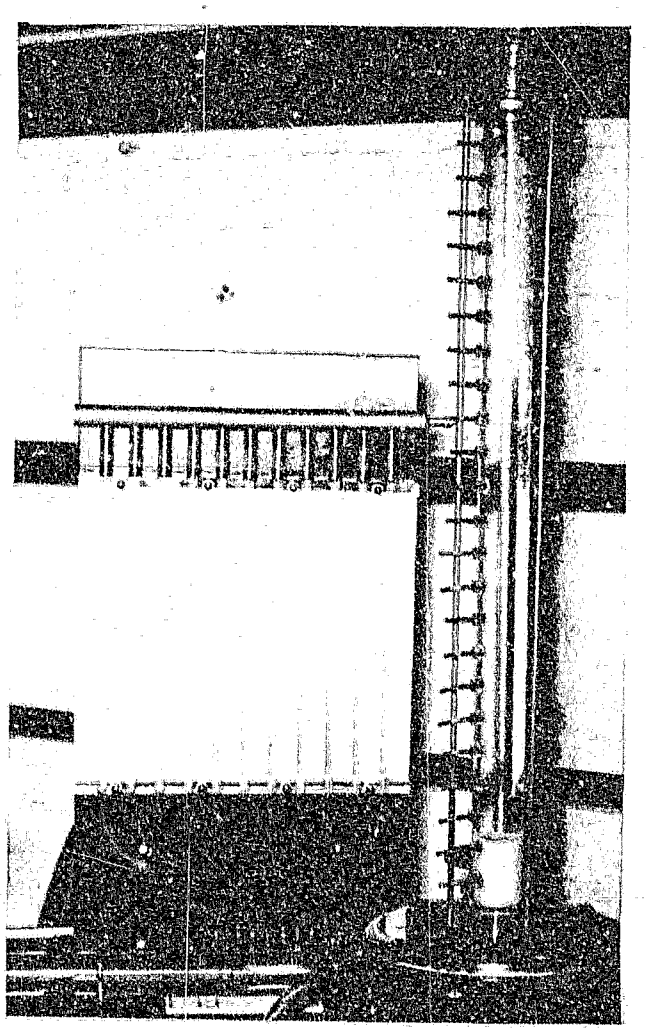


FIGURE 6.9: The experimental rig (Water-Solid)

in an uneven distribution throughout the bed. The bed was therefore prepared in the same way for each test by pouring the sample onto the mesh from the top of the tube and tapping it gently. This height was read as the fixed bed height and checked again after the test had been run. Generally the two readings corresponded very well.

6.10 SAMPLE PREPARATION

The samples used were:

Spherical steel shot	- 0.81 and 1.50 mm ø
Spherical polystyrene beads	- 1.24 mm ø
Sand	- 0.66 mm ø
Rectangular plastic beads	- 3.89 x 3.63 x 2.02 mm

The steel shot was rolled down a 5° incline to remove any irregular shapes from the sample, while the sand was sieved to determine the size range and to remove the fine dust particles. The density was determined by the water displacement method, since the samples were not considered porous.

Free-fall velocities in water were measured using a sampled number of particles from the size distribution sample. The particles were timed falling over a measured distance in a tall flask, taking into account the acceleration distance and the wall effect in the final results.

The typical particle size of the sample was determined by measuring a certain number of the particles with a micrometer and taking the arithmetic average, since the size distribution was not wide enough to introduce significant errors with this method. Prior to each test the sample was weighed dry.

6.11 GENERAL PROCEDURE

After the bed had been prepared, the fluidizing medium was regulated through it at set flows, the following being measured for each flow:

- Bed height.
- Fluid flow.
- Pressure drop at the various tappings.
- Movement of the bed.
- Fluidizing medium temperature.

This procedure was followed until the bed had expanded to the predetermined desired values. At some bed heights, the fluidized bed became very unstable, displaying slugging tendencies; when this occurred the limits were measured, and if possible, the upper limit of velocity for slugging was then exceeded and a steady bed obtained at the higher voidages.

6.12 RESULTS

6.12.1 Particle Size

Where particles are not spherical, a consistent method has to be found for determining the particle diameter or dimension to best fit the available empirical equations. The steel shot and polystyrene beads were spherical but the plastic beads and sand were rectangular and irregular respectively.

The sand free-fall velocity in water was used to obtain the average particle size from the curves of Johnstone et al and of Martin (F6), who used the mean projected area of the particles plotted for sand. Based on a velocity in water of 8.26×10^{-3} m/s, a size of d = 0.66 mm was

obtained with C_D = 1.47. This corresponded well with the observed grading of approximately 80% through 22 mesh B.S.S., which has an aperture of 710 μm.

The plastic beads had a water terminal velocity of 4.53 x 10^{-3} m/s which corresponds to an equivalent sphere of d = 2.77 mm. If the boundary effect correction factor (C_W) of Francis and Ladenburg (F6) is applied, C_W = 1.08, and the free-fall velocity becomes 4.53 x 10^{-3} x 1.08 = 4.90 x 10^{-3} m/s, this giving an equivalent sphere d of 3.00 mm (with C_D = 0.81). This was the value used.

The data in Table 6.1 gives reasonable agreement between the visual indication of v_t and the experimental pressure drop/terminal velocity indication (Figure 6.23). The terminal velocities were calculated from the equation

$$v_t = \sqrt{\frac{4\ d\ (\rho_s - \rho_f)\ g}{3\ C_D\ \rho_f}}$$

TABLE 6.1: Free-fall Velocity Data

Fluidizing medium: 1) air, 2) water

Particles	0.81 mm ø steel	1.50 mm ø steel	3.00 mm ø plastic beads	1.24 mm ø polystyrene	0.66 mm ø sand
Density, kg/m^3	7 724	7 724	1 071	1 024	2 615
Calculated free-fall velocity, m/s 1)	12.29	18.60	-	3.80	-
2)	0.317	0.52	0.054	0.008	0.099
Experimental free-fall velocity, m/s 1)	12.27	19.2	not tested	slugging	slugging
2)	0.387	0.493	0.045	0.007	0.089

6.12.2 Fixed Beds

Generally, ε will be lower if the particles are added to the bed slowly and allowed to settle and if the particles have a smooth surface. Loosest packing arrangements are obtained by adding particles to a column containing the fluidizing fluid, but the bed will settle with a resulting increase in pressure drop.

Packed bed voidage values obtained during the tests are given in Table 6.2.

TABLE 6.2: Packed Bed Voidages

d, mm	Air	Water
0.81 (steel)	0.34, 0.37, 0.43, 0.44, 0.41	0.43, 0.44
1.50 (steel)	0.36	0.43, 0.44
0.66 (sand)	0.42	0.48, 0.51
3.00 (equivalent) (plastic beads)	Not tested	0.43, 0.47, 0.49
1.24 (polystyrene beads)	0.44	0.46

Generally, the voidages are higher for the water beds, due probably to the smaller buoyant mass of the particles. The polystyrene beads, which were the lightest of the materials tested, showed little variation. By taking the bed pressure drop over successive intervals, as shown in Figure 6.10, the constant 2 C in equation (6.2) could be evaluated at different points in the overall bed.

Figure 6.11 shows 2 C plotted against the superficial tube velocity v_o for a fixed bed. Two particle diameters, namely,

1.5 mm and 0.81 mm, were used. For the larger particles, the lower region of the bed had a lower 2 C value, whereas for the smaller particles, the 2 C value was higher. In other words, the bed packing is not uniform and the pressure drop is not necessarily proportional to the bed height. However, the overall bed pressure drop gives a value of 2 C = 976 which relates well to the Bureau of Mines results (F6).

The bed packing density seemed to be fairly uniform, as shown in the Figure 6.12 results of bed height vs bed mass. The steel shot packing tended to be denser in the air beds. (The bed mass was measured in air.) A similar trend appears for the sand sample.

If the bed is restrained (ie, by placing a mesh screen over the bed) and the velocity is slowly increased, the overall bed pressure drop curve displays two distinct lines intersecting at v_{mf}, the minimum fluidization velocity (Figure 6.13). Theoretically the curve above v_{mf} should be a parabola since ΔP is proportional to velocity squared.

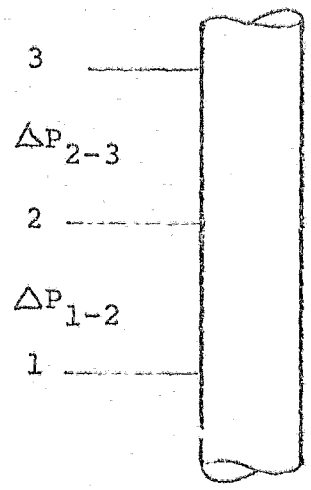


FIGURE 6.10: Pressure drop nomenclature

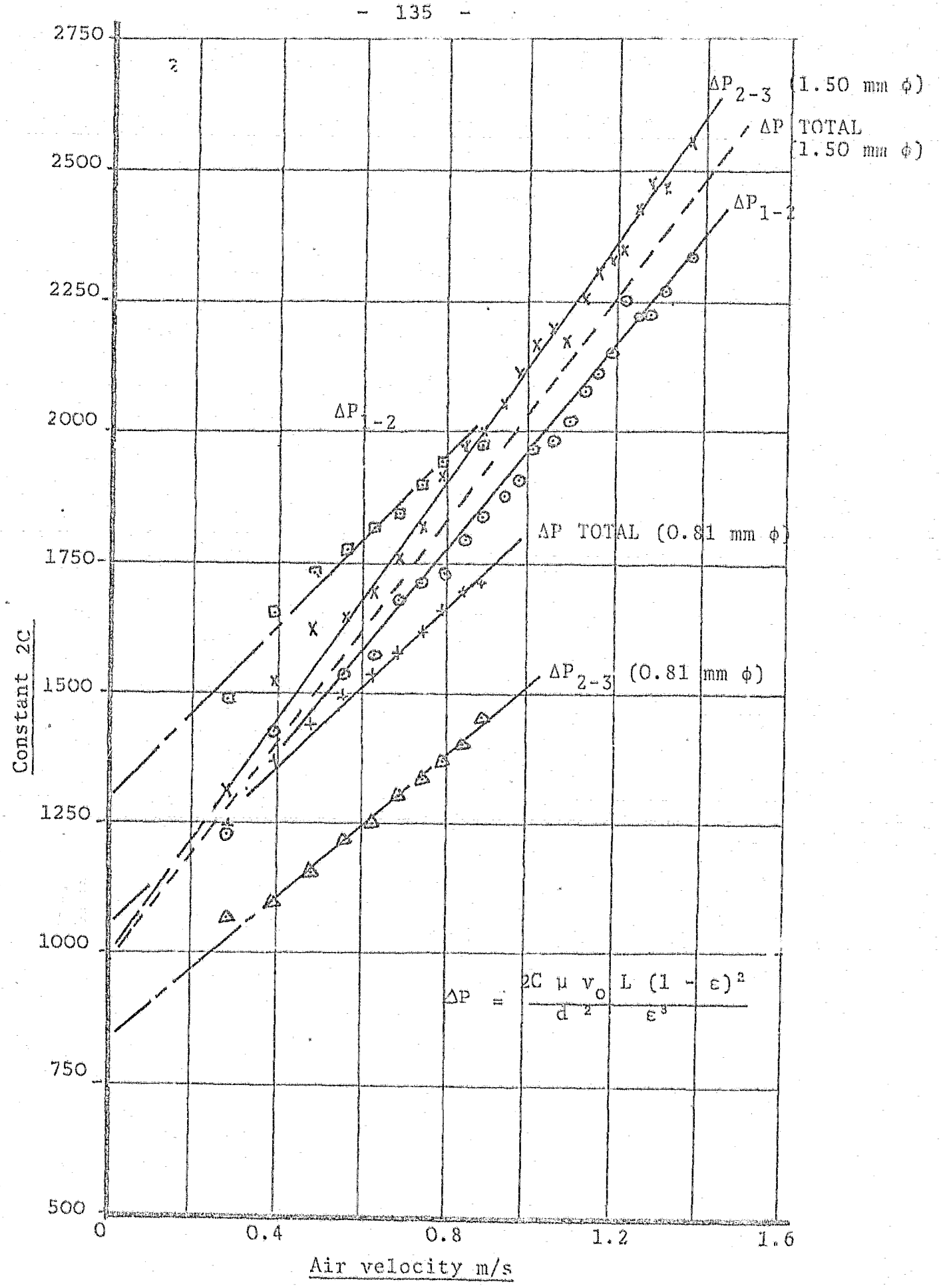


FIGURE 6.11: Constant 2C vs air velocity

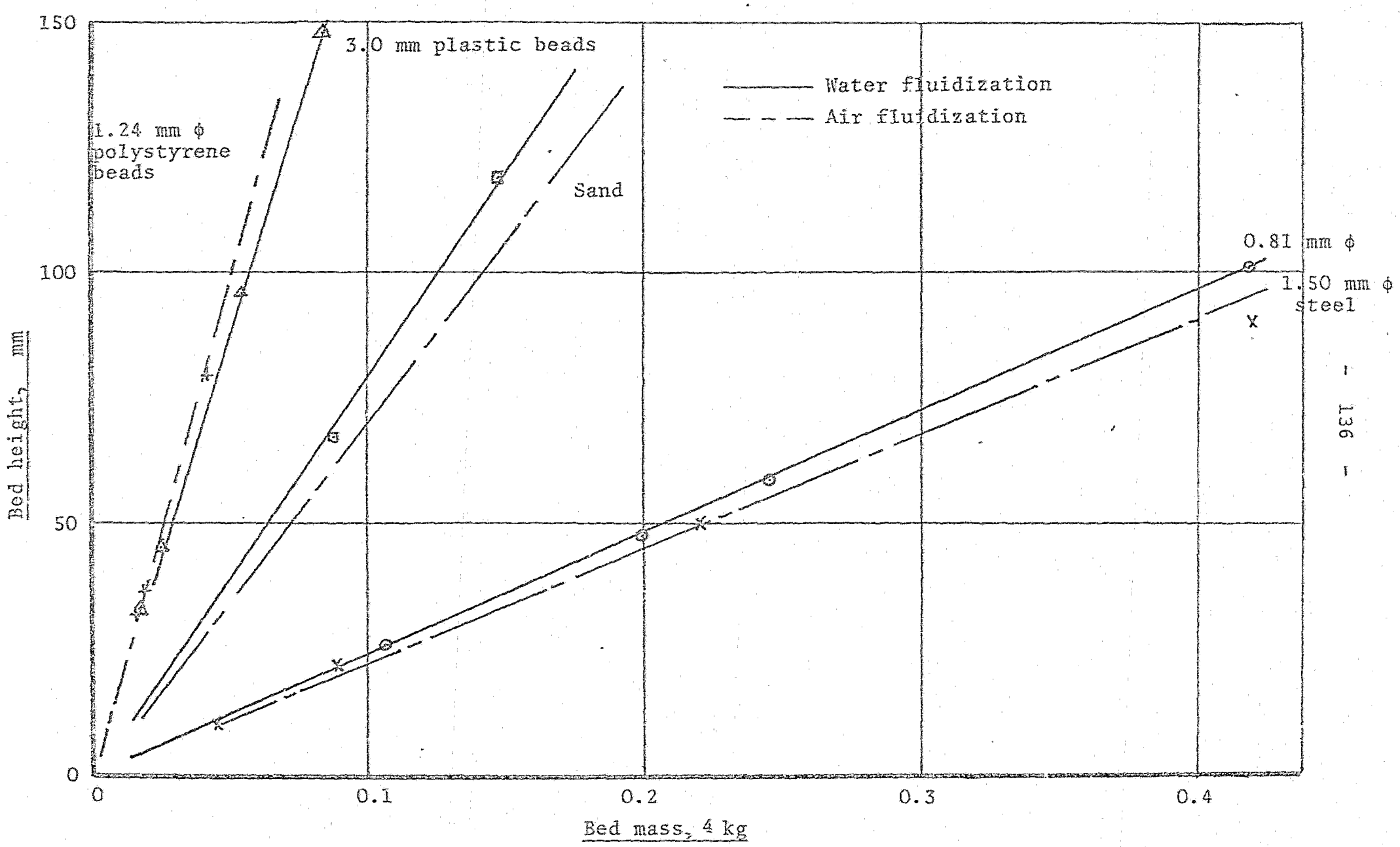


FIGURE 6.12: Bed height vs bed mass

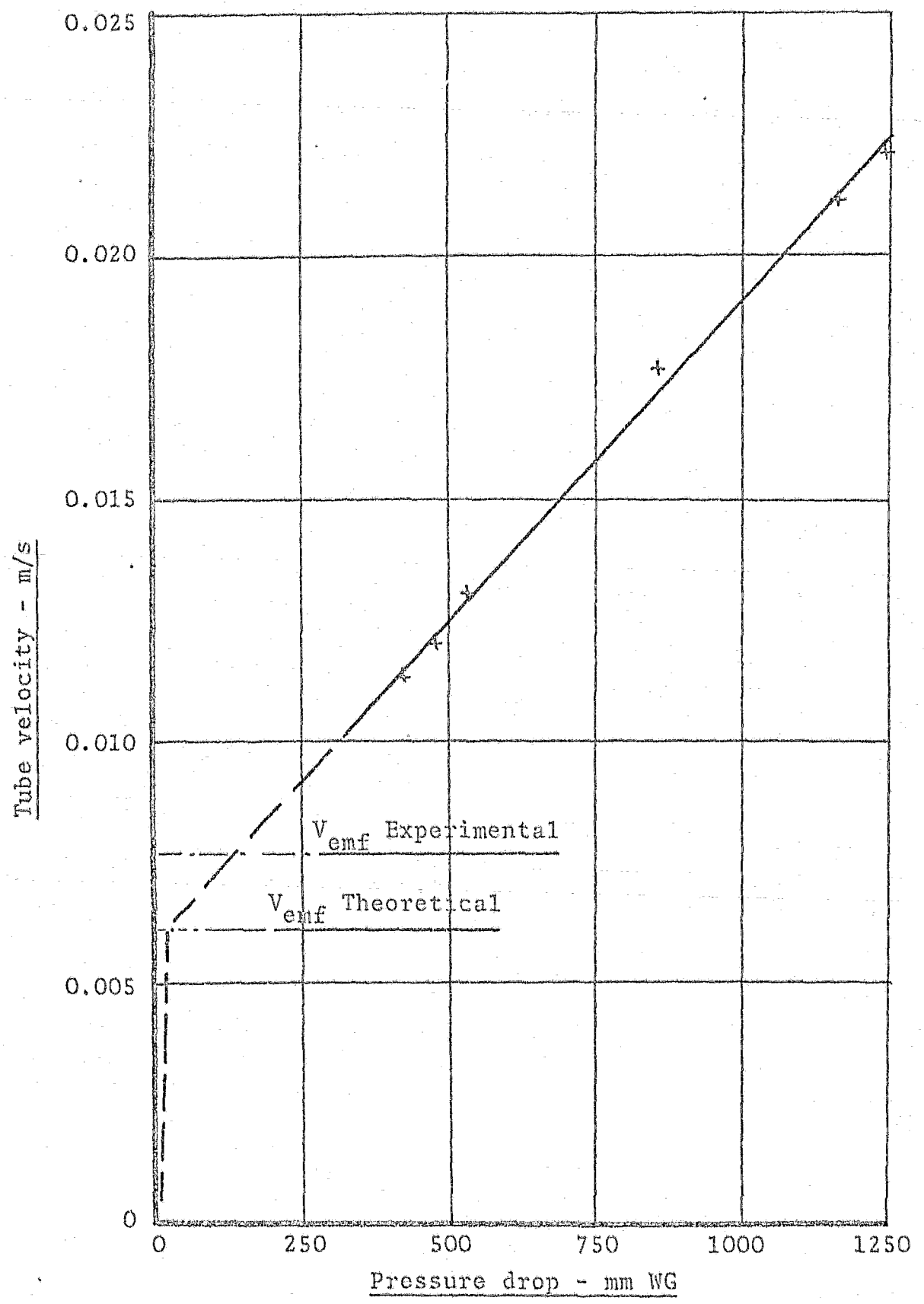


FIGURE 6.13: Pressure drop through a packed restrained column

6.12.3 Slugging

As mentioned above slugging occurs mainly in gas-solid systems. This was confirmed by observations in this series of tests.

Figure 6.14 is the typical pressure drop curve for a slugging bed at various points within the bed. The pressure peaks indicate the slugging region and it would appear that curve 2, corresponding to pressure tapping 2 at 38 mm above the screen, is where slugging starts. The pressure surge seems to be damped as it travels to the surface indicating that external pressure tapping points will probably not detect a slugging bed, and that a visual verification is necessary. This point is important when considering mill operation. As the bed expands and slugging starts, the frequency of slug or bubble formation increases to a point and then decreases as the bubbles become larger. Figure 6.15 shows this peak frequency plotted as a function of air velocity ratio. This was for one particular size of particle. The static bed height also appears to be a function of peak frequency, as shown in Figure 6.16. In fact, the peak frequency is inversely proportional to the static bed height. For this experiment 1.50 and 0.81 mm ø steel shot was used. The results may be expressed in the equation

$$1/L = 2.4 \times 10^{-4} H - 0.02$$

As the bed height is increased it appears that the frequency will remain at a maximum value of about 100, indicating a bad slugging region since with the lower frequency the slugs tend to be larger. The fluidizing tube diameter was not altered in these tests and if the results of Agarwal and Storrow (F6) are indicative for steel, the incipient velocity for slugging should increase slightly with

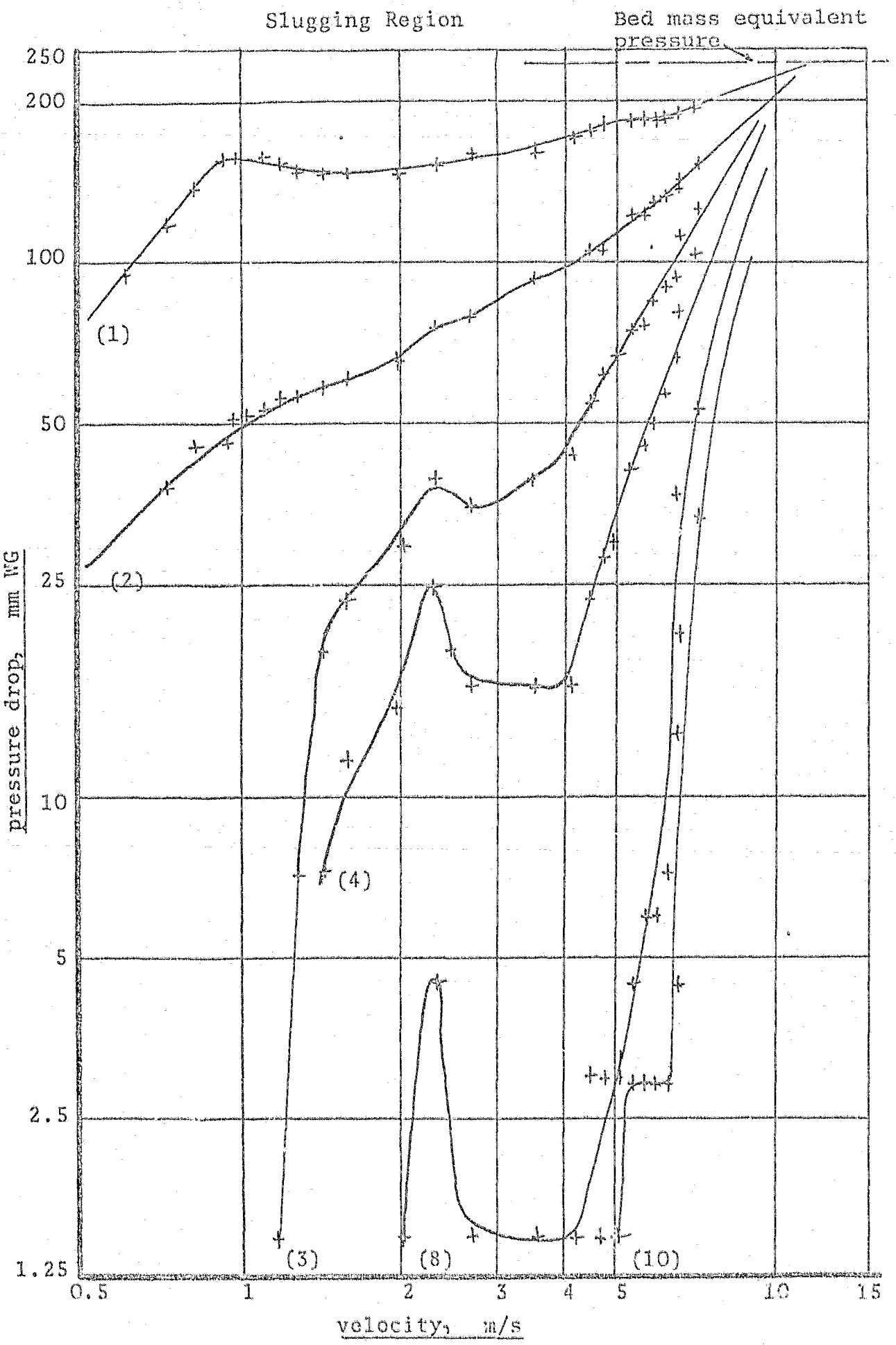


FIGURE 6.14: Pressure drop - velocity curves for an air fluidized bed

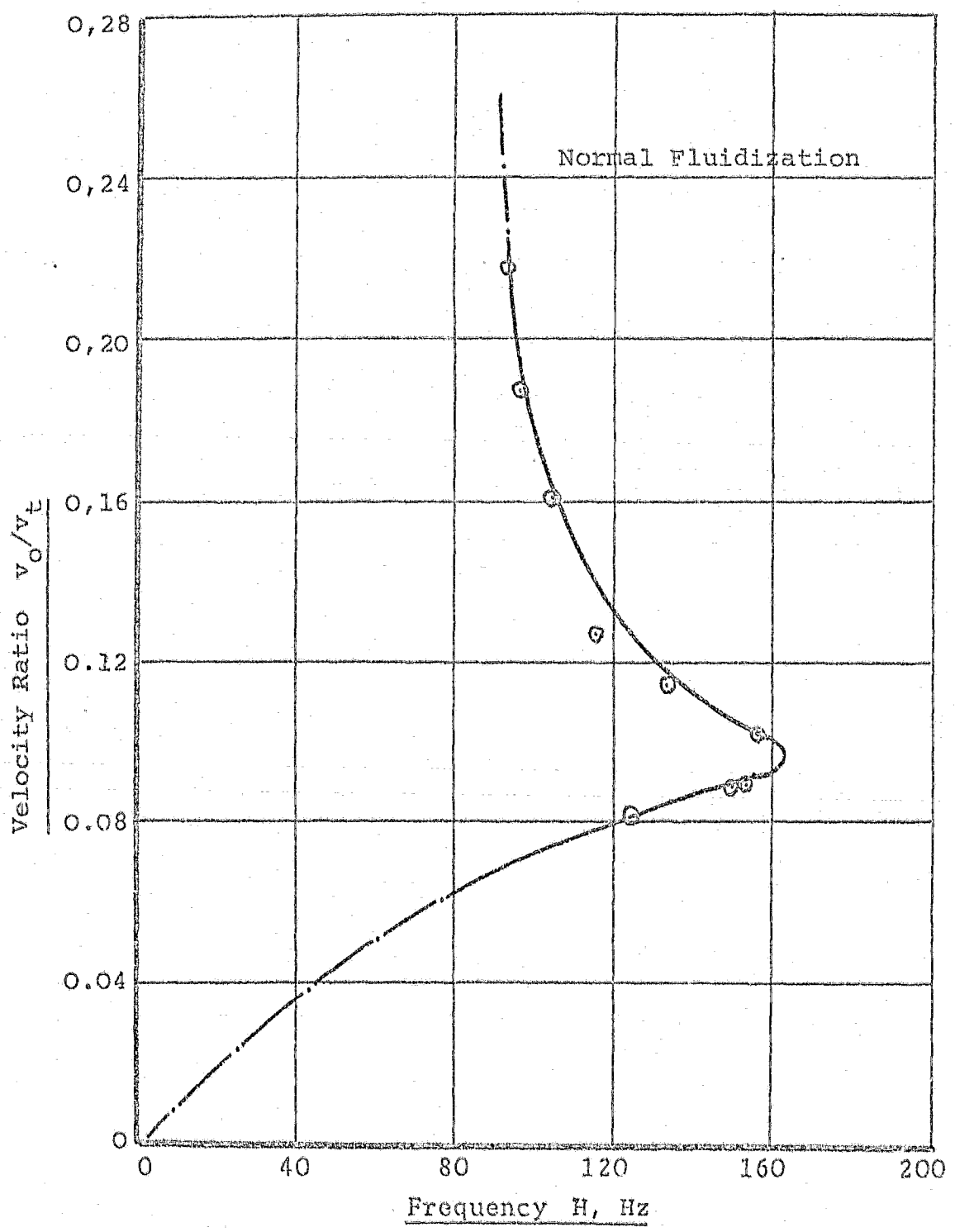
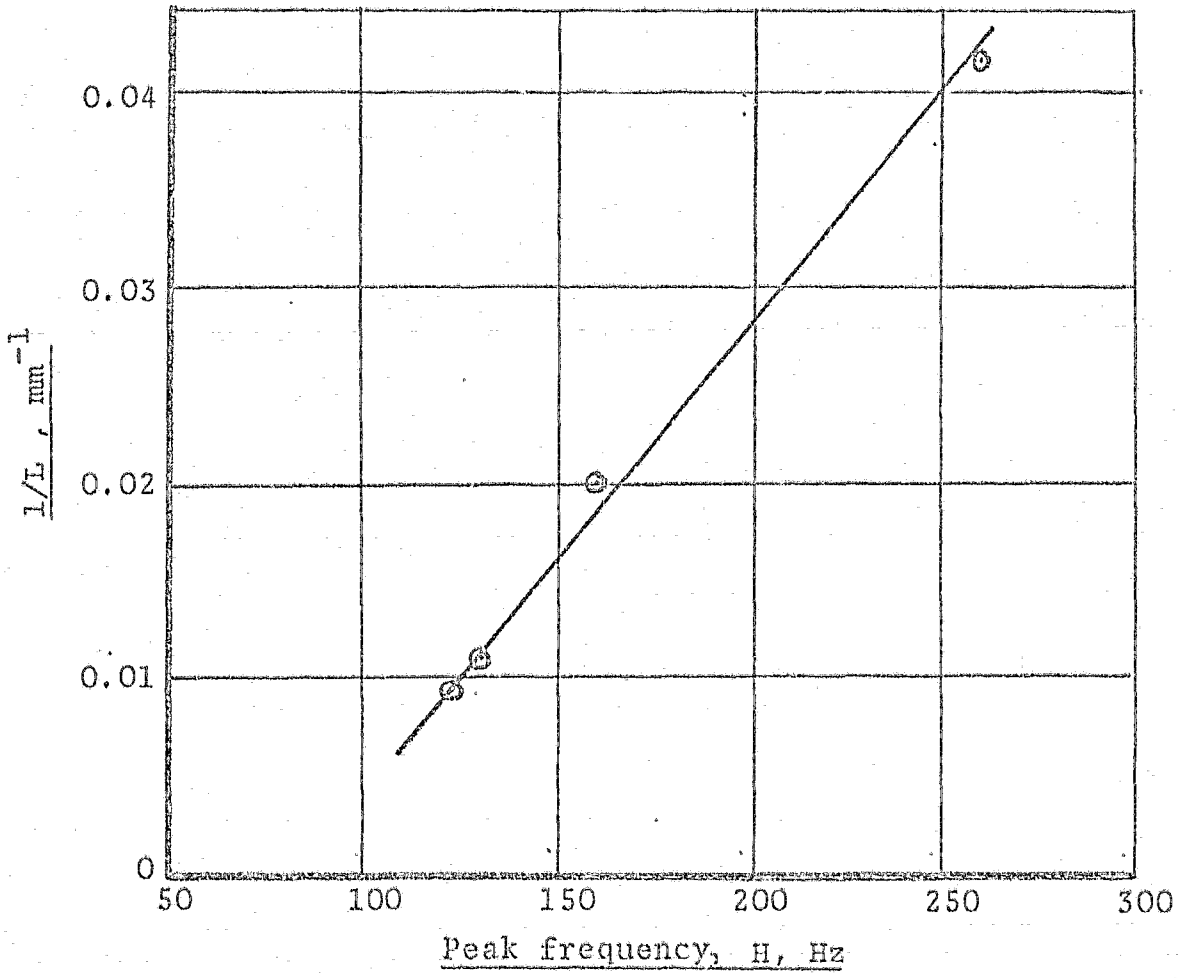


FIGURE 6.15 : Frequency vs velocity ratio for a particular bed height



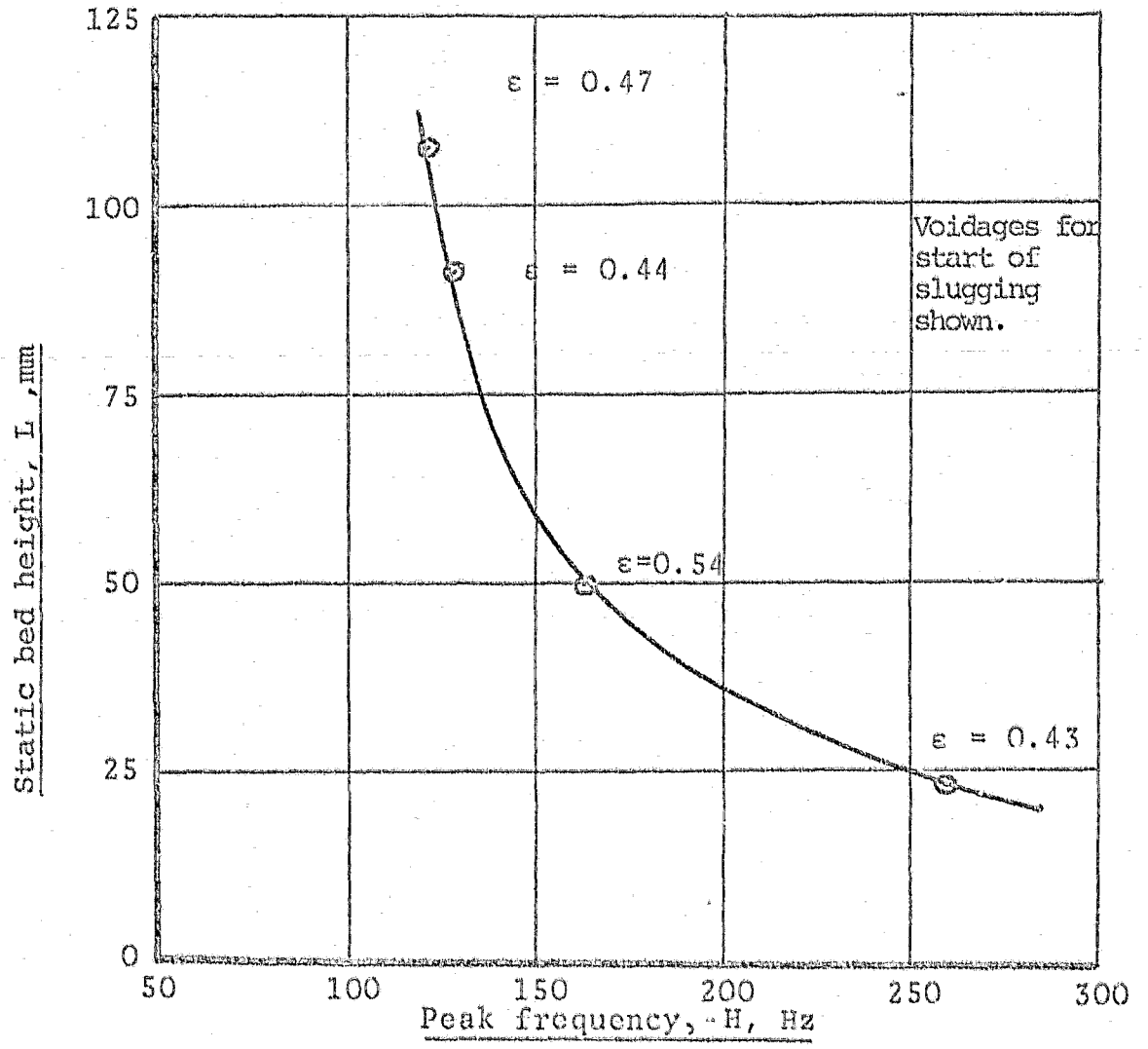


FIGURE 6.16: Peak frequency vs bed height

tube diameter. For increasing bed height, the incipient velocity decreased.

6.12.4 Minimum Fluidization

Table 6.3 gives comparisons of the minimum fluidization velocity derived from the equations discussed in Section 6.6. It will be noticed from the table that with the available air results, the most reliable equations appear to be those of Leva (6.2), and of Bourgeois and Grenier (6.9). The Miller-Logwinuk equation (6.8) gives high results for air fluidization.

The figures for water fluidization show good agreement between the Leva (6.2) and Bourgeois-Grenier (6.9) equations and the experimental results.

TABLE 6.3: Minimum Fluidization Velocity Data

Fluidizing medium : 1) air, 2) water
Velocities in m/s are shown.

d		These results	Leva (Eqn. 6.2)	Miller-Logwinuk (Eqn. 6.8)	Bourgeois-Grenier (Eqn. 6.9)
0.81 mm ø steel	1)	1.006	0.936	1.418	0.826
	2)	2.96×10^{-2}	2.15×10^{-2}	4.51×10^{-2}	2.33×10^{-2}
1.24 mm ø polystyrene	1)	<0.610	0.482	0.540	0.244
1.50 mm ø steel	1)	1.402-1.738	1.628	3.326	1.427
	2)	5.09×10^{-2}	3.29×10^{-2}	1.534×10^{-1}	4.48×10^{-2}
		5.70×10^{-2}			

6.12.5 Expanded Bed (Liquid-Solid)
Hawksley-Vand and Brinkman Equations (Equations 6.10 and 6.11) (Figures 6.17 and 6.20)

Although the experimental values of Re were above the laminar region, the test points were plotted as though these equations held. The air-solid results plotted in Figure 6.20 tend to fall closer to the Brinkman equation whereas for liquid-solids the results are more in line with the Hawksley-Vand equation. What the curves definitely show is that the voidage is not a linear function of superficial (tube) velocity.

Using equation (6.12) gives the slopes for various materials tested in Table 6.4. Figure 6.18 shows the plotted test results. (For reference, refer also to Figure 6.6.)

TABLE 6.4: Expanded Bed Results (from Figure 6.18)

MATERIAL	Re	SLOPE	ε
Sand	0-16.5 16.5 up	-1.11 -0.445	0.48-0.67 0.67 up
Polystyrene beads	0-1.25 1.25 up	-2.05 -0.63	0.46-0.608 0.608 up
Steel shot 1.5 mm ø	70-200	-0.657	0.434-0.63
Steel shot 0.81 mm ø	25-120	-0.719	0.43-0.65
Plastic beads	18-70 70 up	-0.60 -0.21	0.53-0.73 0.76 up

The curves of Figure 6.18 show a definite slope change occurring in the region of $(1 - \varepsilon)/\varepsilon^3 = 0.65$ upwards ($\varepsilon = 0.74$). It is interesting to note that the sand and polystyrene curves with the lowest Re gave higher nega-

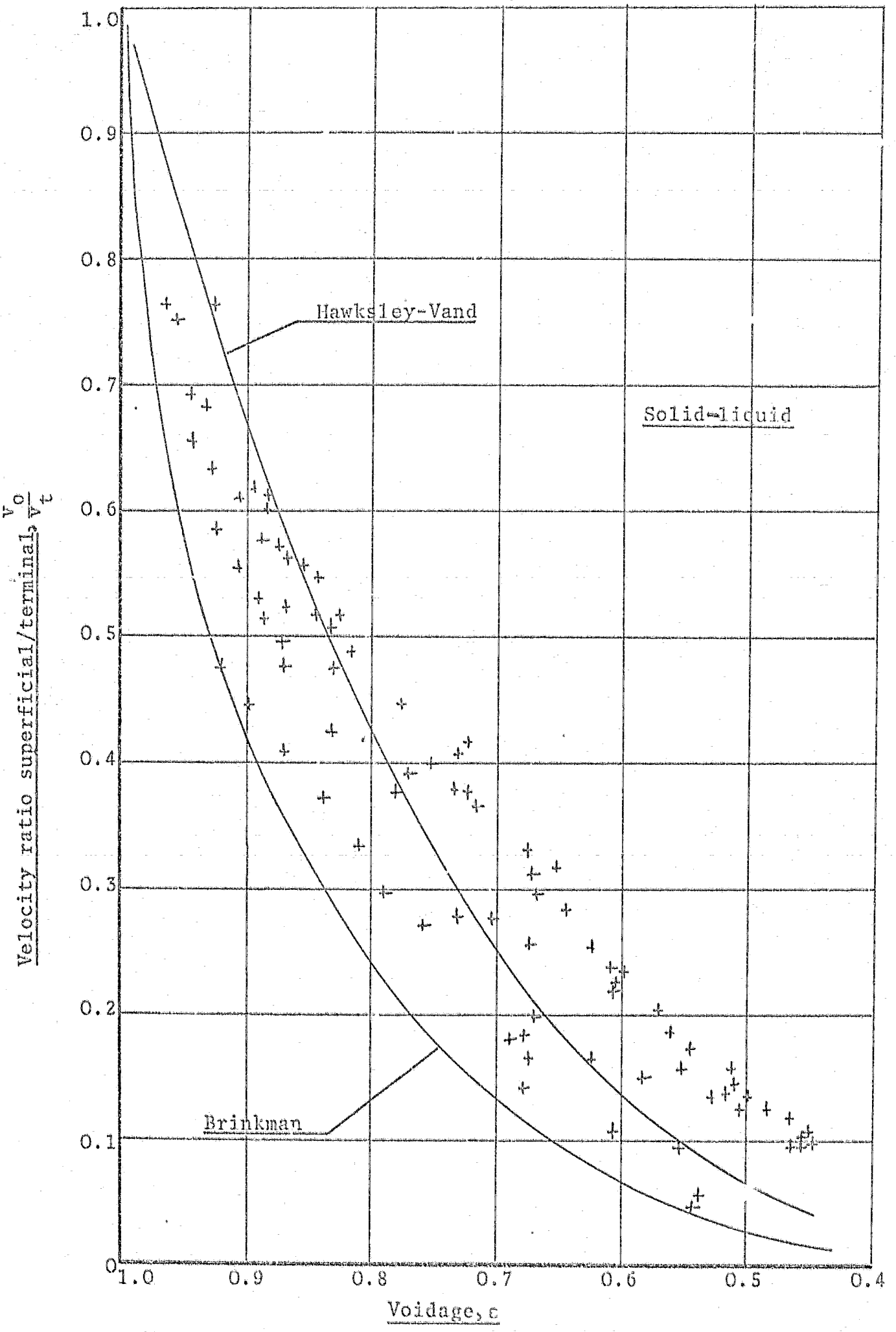


FIGURE 6.17: Voidage vs velocity ratio with theoretical curves superimposed

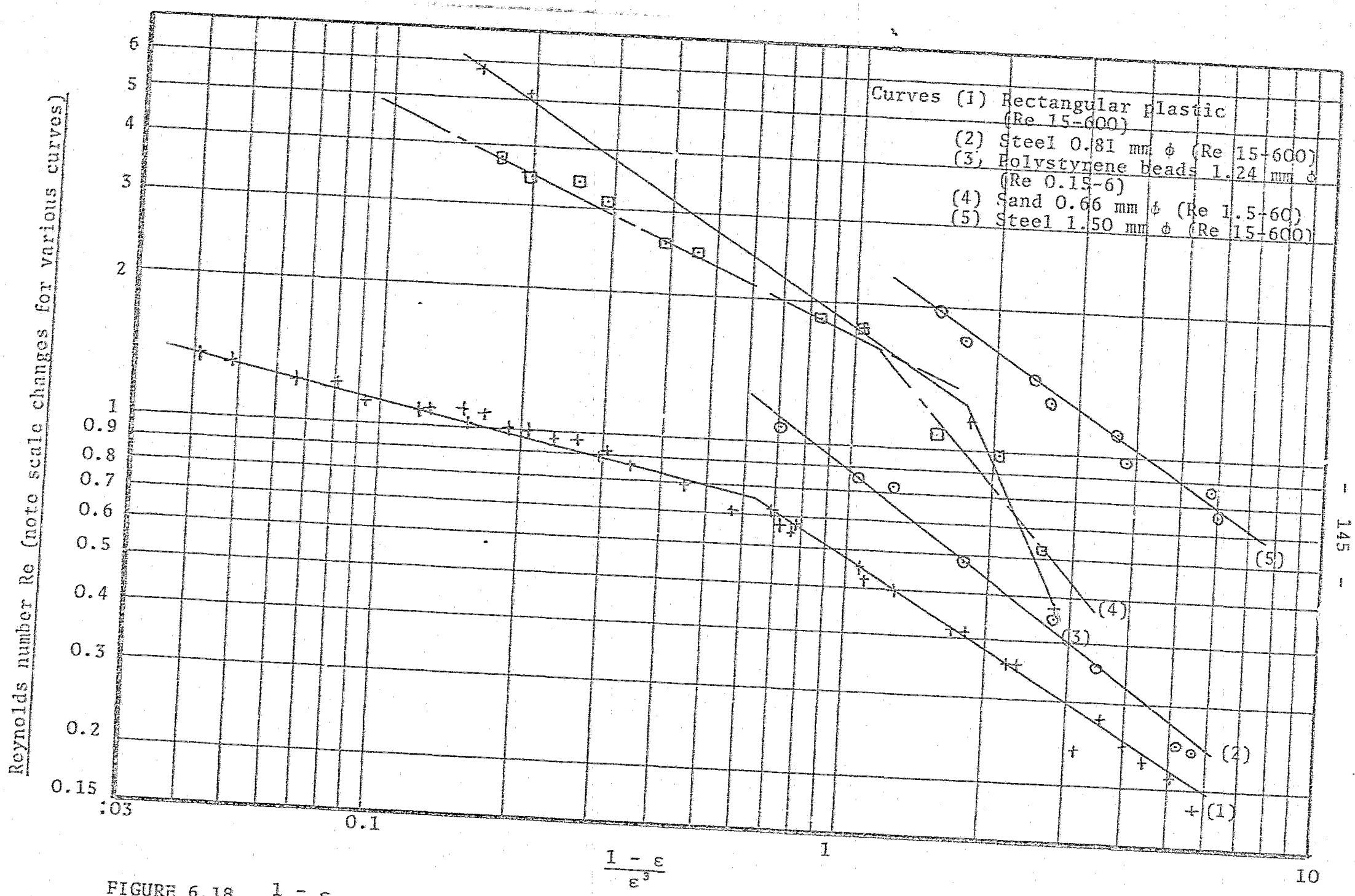


FIGURE 6.18. $\frac{1-\varepsilon}{\varepsilon^3}$ vs Reynolds number for solid-liquid expansion

TABLE 6.5: Experimental Results of Richardson and Zaki Equation (Equation 6.14)

	LAMINAR		TRANSITION		TURBULENT	
AUTHOR (F6)	EXPERIMENT	R-Z EQN.	EXPERIMENT	R-Z EQN.	EXPERIMENT	R-Z EQN.
Jottrand	5.1	4.9	-	-	-	-
Johnson	5.1	4.8	-	-	-	-
Verschoor	4.3	4.5	-	-	-	-
Hatch	4.0	4.4	-	-	-	-
Lewis et al	-	-	3.8	4.1	-	-
Young	-	-	3.8	3.6	-	-
Wilhelm & Kwauk	-	-	3.1	3.3	-	-
Wilhelm & Kwauk	-	-	-	-	2.7	2.5
Wilhelm & Kwauk	-	-	-	-	2.5	2.39
Fong (F3)	4.6	4.45	2.8	4.06	-	-
Lewis & Bowerman	8.33	2.94	-	-	-	-
These results	8.51	5.34-4.98	2.4	5.10-3.00	2.86.	2.39
	-	-	4.3	-	3.44	2.39

tive slopes. The results are therefore strongly flow regime dependent. The laminar flow range was assumed in the derivation of the equation, and turbulent and transition range results will therefore be of doubtful value.

Richardson-Zaki Equation (Equation 6.14) (Figure 6.19)

Generally, the test results, as shown in Table 6.5, were in line with the Richardson-Zaki correlations in that the same trend was apparent (high m in laminar and low m in turbulent flow). The high laminar value obtained in these tests is illustrated only by the first test point for polystyrene beads, and if this is ignored and the upper part of the curve considered, a slope of 4.33 emerges, which is more in line with other data.

It is interesting to note the trend in Table 6.6 showing Figure 6.18 curve slopes against particles diameter.

TABLE 6.6: Experimental Slope and Particle Size Comparison

m	d, mm
5.14	0.66
3.38	0.81
4.33	1.24
3.02	1.50
2.41	3.00

It would appear that particle size has a larger influence on the d/D_t ratio of the Richardson-Zaki equation.

In conclusion it may be stated that the Richardson-Zaki correlations give a reasonably reliable result throughout

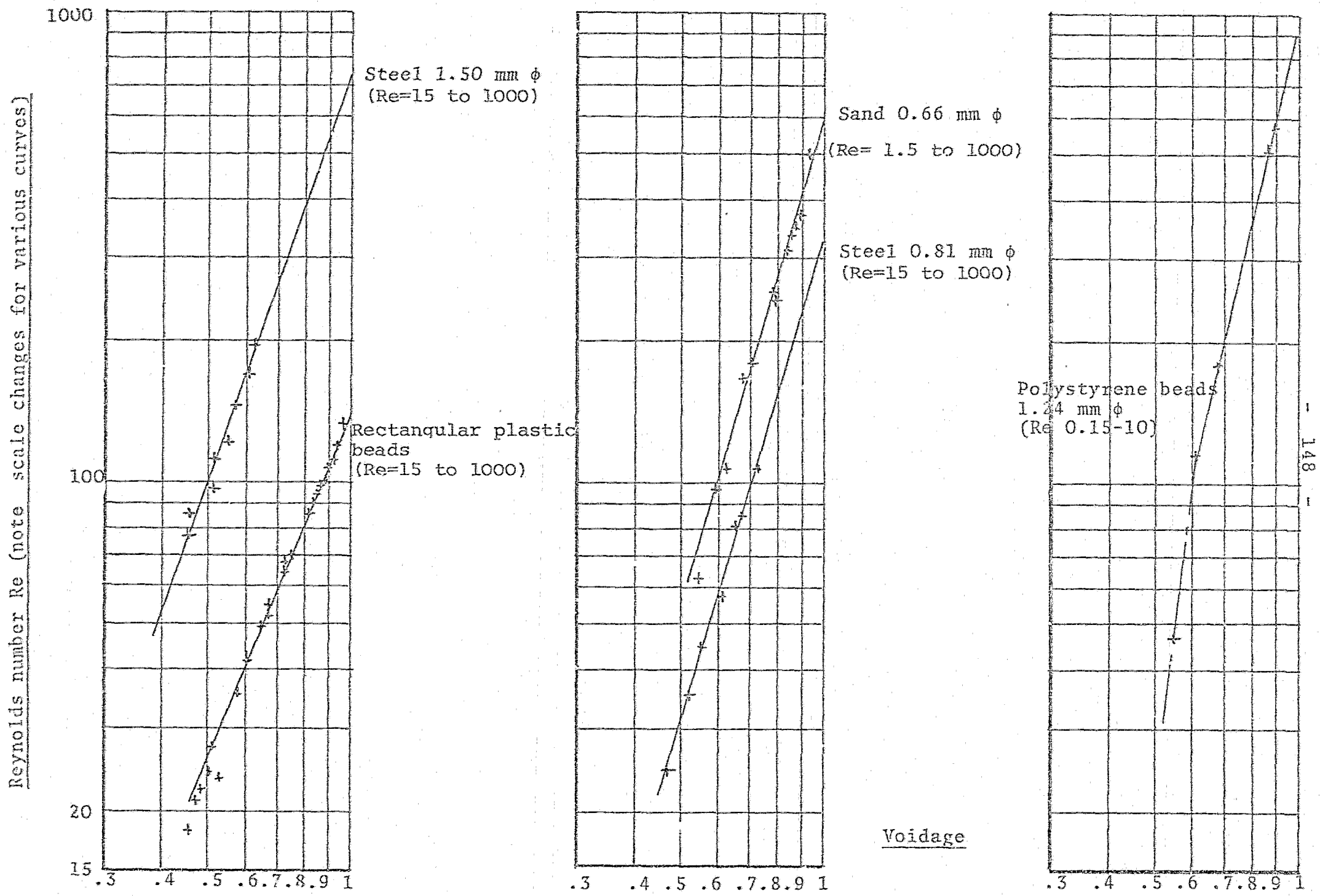


FIGURE 6.19 : Voidage vs Reynolds number for solid liquid expansion

the flow regimes approaching $\varepsilon = 1$. The curves may also be usefully used to establish particle terminal velocity by extending the line to $\varepsilon = 1$ in Figure 6.18.

6.12.6 Expanded Bed (Solid-Air)

The Hawksley-Vand and Brinkman equations for solid-air results are plotted in Figure 6.20. It is clear that no definite relationship can be established (besides which the equations are for laminar flow). The gap between $\varepsilon = 0.55$ and $\varepsilon = 0.75$ occurred because of slugging in that range.

If the same plot as Figure 6.18 is used for the same solids, much flatter curves result (Figure 6.21). The values of m obtained are shown in Table 6.7.

TABLE 6.7: Experimental Results from Figure 6.21

d, mm	m
0.66	-0.45
0.81	-0.48
1.24	-0.52 to -0.53

Figure 6.22 shows the expansion curves for a uniformly expanding bed with no slugging. Where the curves intersect the bed mass pressure equivalent is the particle terminal velocity.

6.13 CONCLUSIONS

The fluid bed tests were conducted mainly to become familiar with the parameters and phenomena associated with fluidization, with the aim of applying this knowledge to the principles of operation of an air-swept mill.

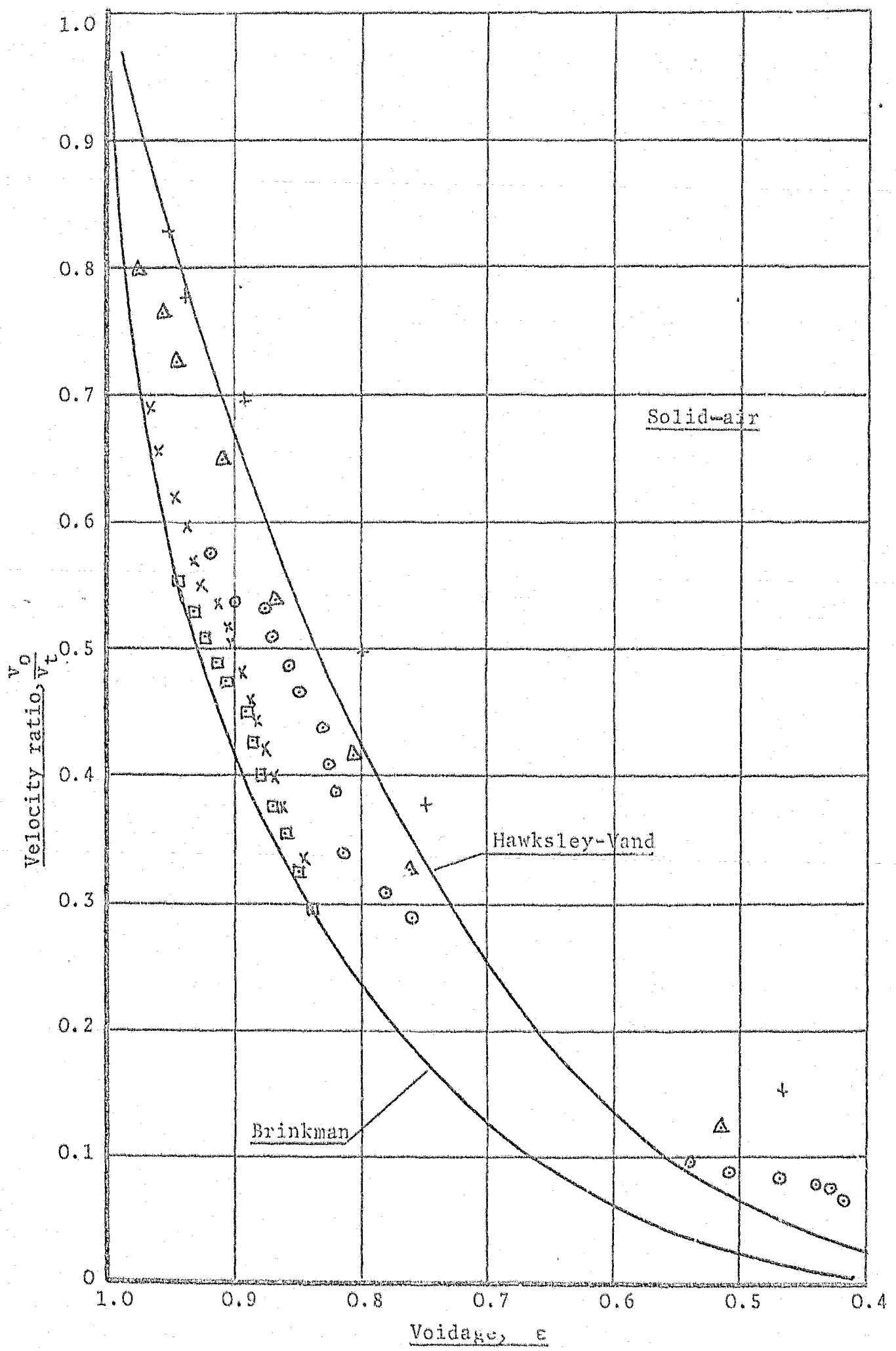


FIGURE 6.20: Voidage of an expanding bed

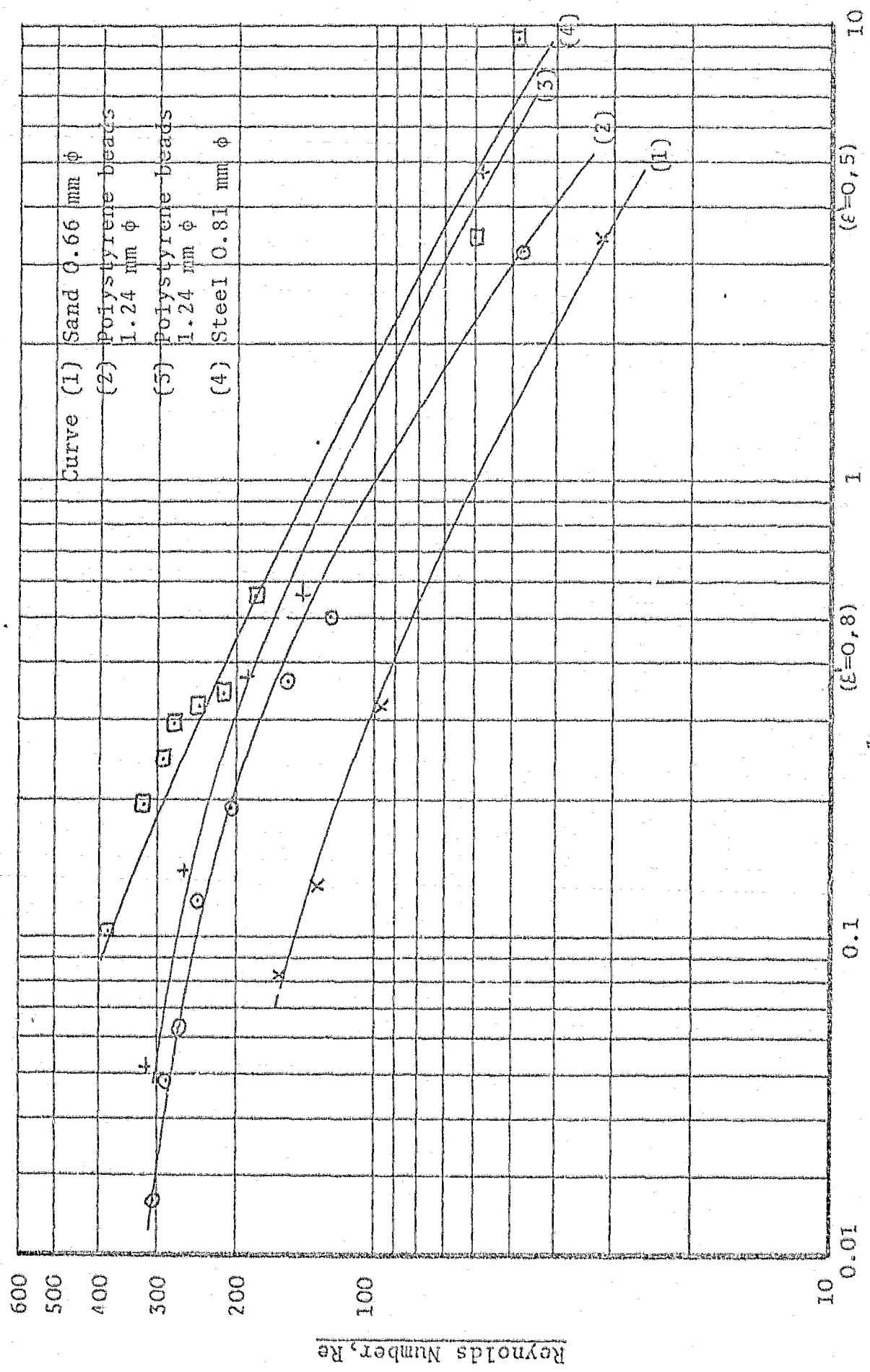


FIGURE 6.21: $\frac{1-\varepsilon}{\varepsilon^3}$ vs Reynolds number for solid-air expansion

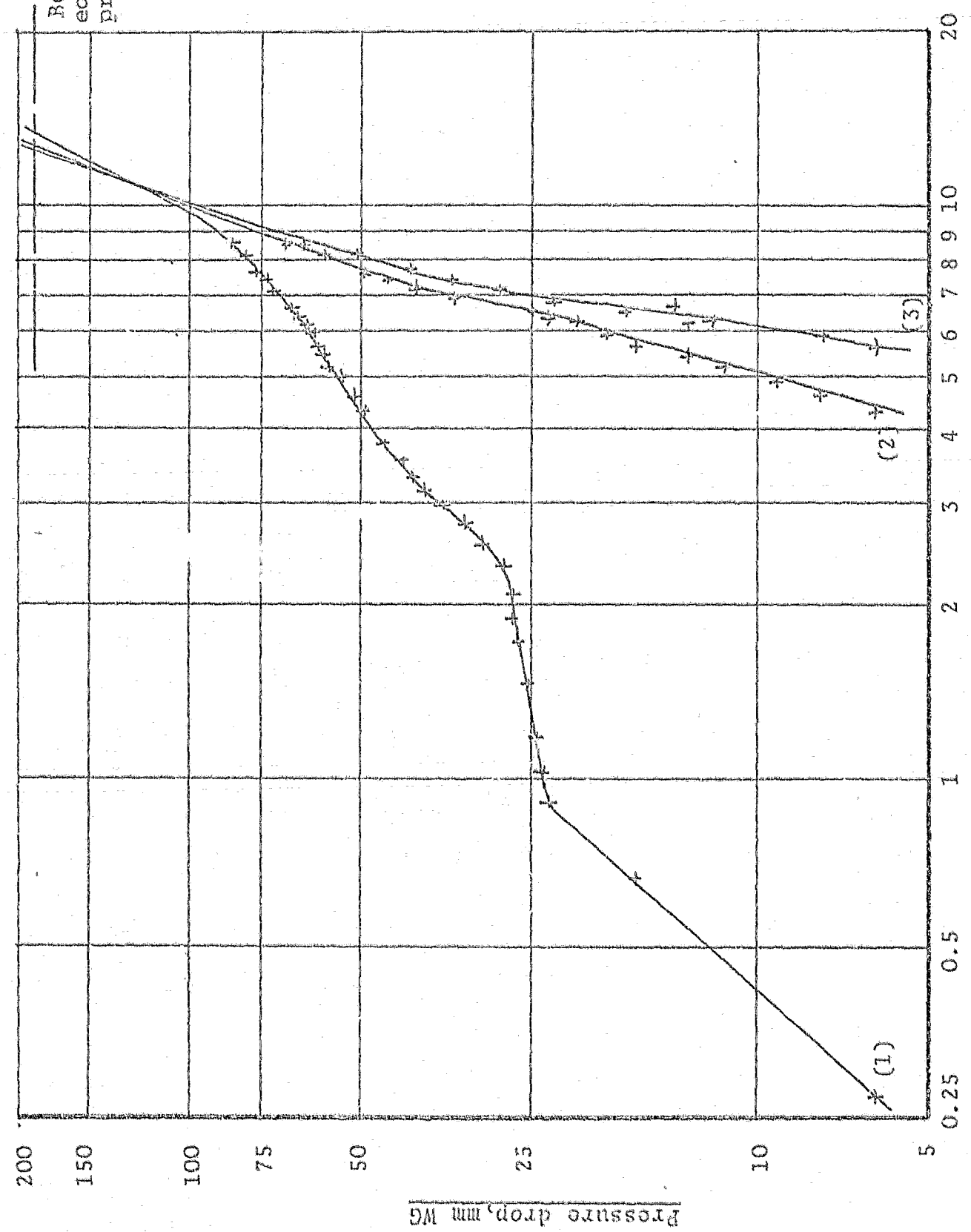


FIGURE 6.22: Bed expansion curve with no slugging

The results obtained agreed reasonably well with existing data, although in some instances the values of such parameters as tube diameter and particle size and shape were not identical. The results obtained by the use of a correlation equation will show greater or lesser scatter depending on which shape factor is applied. The slugging phenomenon was observed to be more prevalent in gas-solid systems which is normal.

The relationship of slugging frequency to velocity ratio has not been noted in the literature.

Although an actual mill is characterised by a continual addition to and withdrawal from the fluid bed, and the velocity is much higher, certain principles and parameters can be utilised to describe and optimise the operation of the fluid bed, especially directly above the throat. Considering the results in this light, the most useful equation for gas-solid systems appears to be equation (6.12). However, the possibility of slugging occurring in a mill has not been ruled out although the pressure indications from typical operating conditions do not suggest that this phenomenon occurs. Localised slugging above the throat in the high voidage area would not be observed by pressure fluctuations at the mill outlet due to the damping action within the main body of the mill.

CHAPTER 7

INDUSTRIAL TESTS

7.0 INTRODUCTION

Industrial tests were carried out at two power stations, namely Arnot and Camden. Due to the fact that these tests were conducted whilst the plants were being commissioned and adjusted, some results could not be confirmed by a second series of tests and therefore the results must be seen more as a trend rather than specific figures for these mills and plants. Similarly, some tests had to be abandoned due to further unavailability of plant for testing.

This chapter is divided into two sections, dealing with the Arnot and the Camden tests, respectively.

7.1 ARNOT TESTS

7.1.1 Introduction

The Loesche LM 18 pressure mills (Figure 7.1) are installed at Arnot Power Station in the Eastern Transvaal. The design throughput is 35.5 t/h of 25 mm feed coal of approximately 8% total moisture, grinding to 95-96% minus 100 mesh. Each mill supplies eight burners, all being on the same horizontal level.

7.1.2 Principle of Operation

A variable speed, totally enclosed table feeder, with fixed radial arm for sweeping coal off the table, feeds coal to the mill. The arm is manually adjustable to give optimum response to the feeder signal. The two free-running hydraulically and pneumatically loaded rolls grind the coal. Stationary vane-type louvre throats around the edge of the table discharge the hot P.A. into the mill to sweep up the coal spillage into the body of the mill. Some oversize particles will fall back on to the grinding table in the lower velocity area of the grinding chamber, whilst the rest of the oversize is conveyed into the static multi-vane separator.

Here oversize is centrifuged out of the main air/pulverised fuel stream and gravity discharged through flaps at the bottom of the separator on to the table for regrinding. The vanes are manually adjustable. The air/pulverised fuel stream of the required fineness leaves the mill via a single exit pipe which then splits into eight individual pipes, one to each burner.

7.1.3 Testing Programme

Together with the Loesche mills at the Grootvlei Power Station, the mills at Arnot were the first Loesche mills to operate in South Africa. Numerous design problems were encountered which were aggravated by the poor quality of coal being ground. The Continental approach to rejection of material from a mill is that usually only tramp iron, etc., comes through with the coal, and thus is not of a large enough quantity to affect overall design. Therefore, when coal high in reject material was used in the South African power station, these mills did not perform satisfactorily.

The problems relevant to this investigation were:

- Velocities were too low in the louvre, resulting in high rejection rates.
- High wear rates resulted from increased velocities used to cut down rejects.
- The fineness of the pulverised fuel was poor.
- The feed coal was highly abrasive and not to size specification.

A programme was therefore initiated to examine mill performance, using the information gained from the mill model studies, and to confirm certain visual wear effects apparent in the mill body.

The areas to be investigated were:

Louvre throat design
Temperature gradient
Voidage
Separator performance
Roll pressure and speed
Coal properties in relation to wear

7.1.4 Throat Design

The original louvre was designed for a certain air/fuel ratio at a maximum rated output, but at this ratio the rejection rate was extremely high. Coupled with this was the inadequate size of the reject boxes (for the reasons stated above), so that under pressure this reject material was being blown all over the mill basement. This resulted in reject box fires and mill shutdowns.

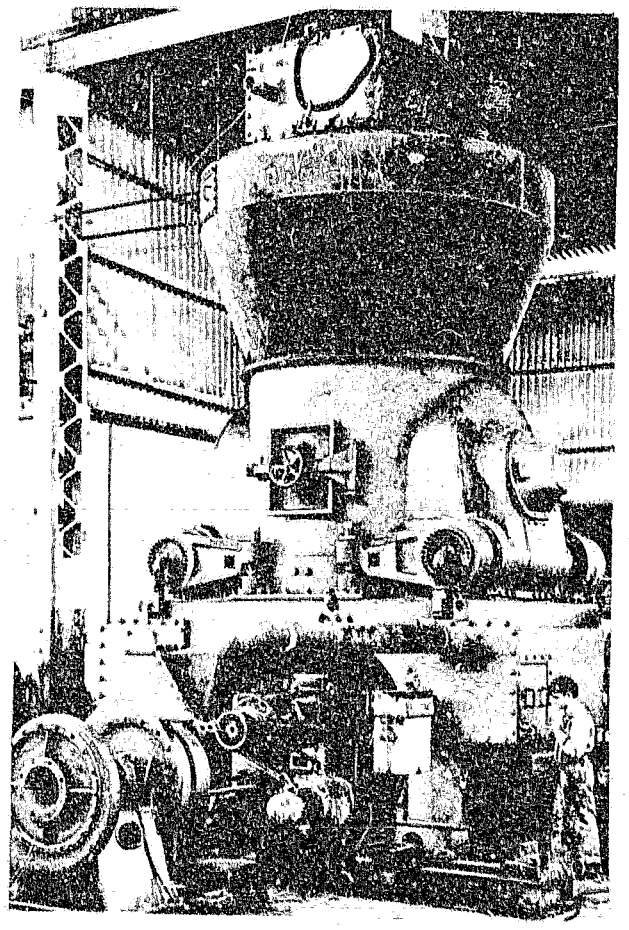


FIGURE 7.1: LM18 mill undergoing works testing

7.1.4.1 Throat Pressure Drop

The pressure drop through the mill is measured at pressure tapping points at the mill inlet before the throat, and at the mill outlet after the separator. As is shown by the figures in Table 7.1, the throat pressure drop is a large proportion of the total mill diff for air only.

TABLE 7.1: Clean air pressure drops

P.A. pressure (mill inlet), mm WC	Pressure at tapping above throat, mm WG	Mill outlet pressure mm WG
896	343	338
213	76	69

For practical considerations, it is allowable to assume that the throat pressure drop due to air only is equal to the mill diff without introducing significant errors.

Pressure Drop

The loss at the throat is caused by the entrance and exit losses:

$$\triangle P_T = \triangle P_{ent} + \triangle P_{exit}$$

When calculating an entrance loss, the effect of the vena contracta has to be considered, and this is expressed by the ratio

$$\frac{A_c}{A_{mi}} = C_c$$

where A_c is the area of the vena contracta, and A_{mi} is the mill inlet area before the throat.

The loss is therefore

$$\triangle P_{ent} = \frac{v^2_{mi}}{2g} \left(\frac{1}{C_c^2} - 1\right) = K_6 \frac{v_T^2}{2g}$$

Similarly the exit loss can be expressed as

$$\Delta P_{exit} = \frac{v_T^2}{2g} \left(1 - \frac{A_T}{A_{mb}}\right)^2$$

where A_{mb} = area of mill body into which throat discharges.

Since $\frac{A_T}{A_{mb}} \ll 1$

$$\Delta P_{exit} \approx \frac{v_T^2}{2g}$$

and the total pressure loss is therefore

$$\Delta P_T = \frac{v_T^2}{2g} (K_6 + 1) = K_7 \frac{v_T^2}{2g}$$

where K_7 is known as the 'throat K factor'. It is apparent that the entrance loss is subject to greater variation than the exit loss due to the inverse relationship $(\frac{1}{C_c^2} - 1)$, and this was verified by the Arnot test results.

7.1.4.2 Experimental Approach

By measuring the P.A. diff and mill diff for various flows of air (without coal) through the mill, a straight line relationship results. (The temperature should be constant throughout the mill for such a test.) Since the P.A. venturi had already been calibrated by a pitot search across the duct, the mass air flow rate could be calculated from

$$v = K_8 \sqrt{\frac{\Delta P_{P.A.}}{\rho_{P.A.}}}$$

so that

$$M = K_9 \sqrt{\Delta P_{P.A.} \rho_{P.A.}}$$

Knowing the throat area, the throat velocity could be cal-

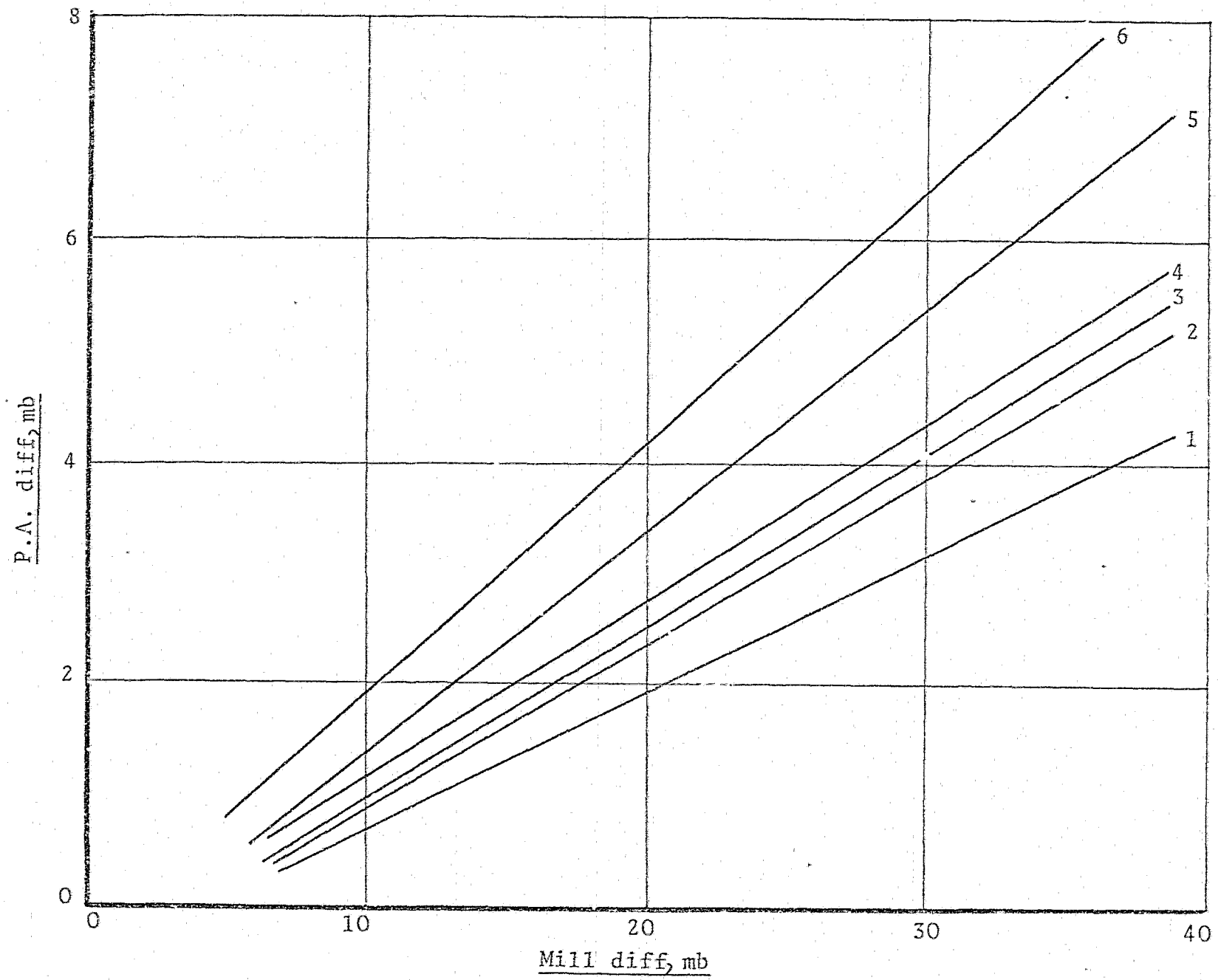
culated since K_9 had been determined experimentally. For each type of louvre, the P.A. diff - mill diff curves were plotted (Figure 7.2). As would be expected, the aerofoil louvre had the lowest resistance since it had the lowest velocity, but when the K factor was taken note of (see following section), it had a higher resistance than the vertical louvre with rounded inlet edges. (The various shapes of louvres are shown in Figs 7.3 to 7.5.)

The effect of rounding the throat inlet edges can be clearly seen by the drop in the value of the K factor. For a discharge restricted by means of a 65^{o} conical armour ring with the 48 mm throat vertical louvre rounded inlet edges, the value of K = 1.71. That is, the K factor has increased from 1.10 to 1.71 by diverting the outlet flow inwards.

When the bypass cone was installed on the 48 mm vertical louvre with rounded inlet edges, the K factor dropped to 1.37 (Figure 7.5). This cone does not hinder the throat expansion to the same extent as the 65^{o} cone, hence the lower pressure drop. A chamfered plate welded into the vertical square-edged louvre gave an indication of the benefit of rounded edges (K = 1.94 in Figure 7.5).

It can therefore be stated from the foregoing results that the inlet configuration and geometry determines the K factor of the throat, and for optimum results, ie, lowest pressure drop, a low K factor should be designed into the louvre. A well-rounded entrance and minimum exit restriction should be provided.

The Loesche original louvre had an aerofoil section as shown in cross-section in Figure 7.6. The fact that the smallest area is at the section 1 - 1 means that material falling off the table was being fluidized well inside the louvre, so resulting in high wear in this area. The vanes



curve	d, mm	Ports blanked	Louvre type
2	48	4	Vert
4	75	6	Vert
6	110	0	45° vanes
1	48	0	Vert
3	48	0	Vert
5	63	0	Vert

FIGURE 7.2 : Mill diff vs P.A. diff for various louvre configurations

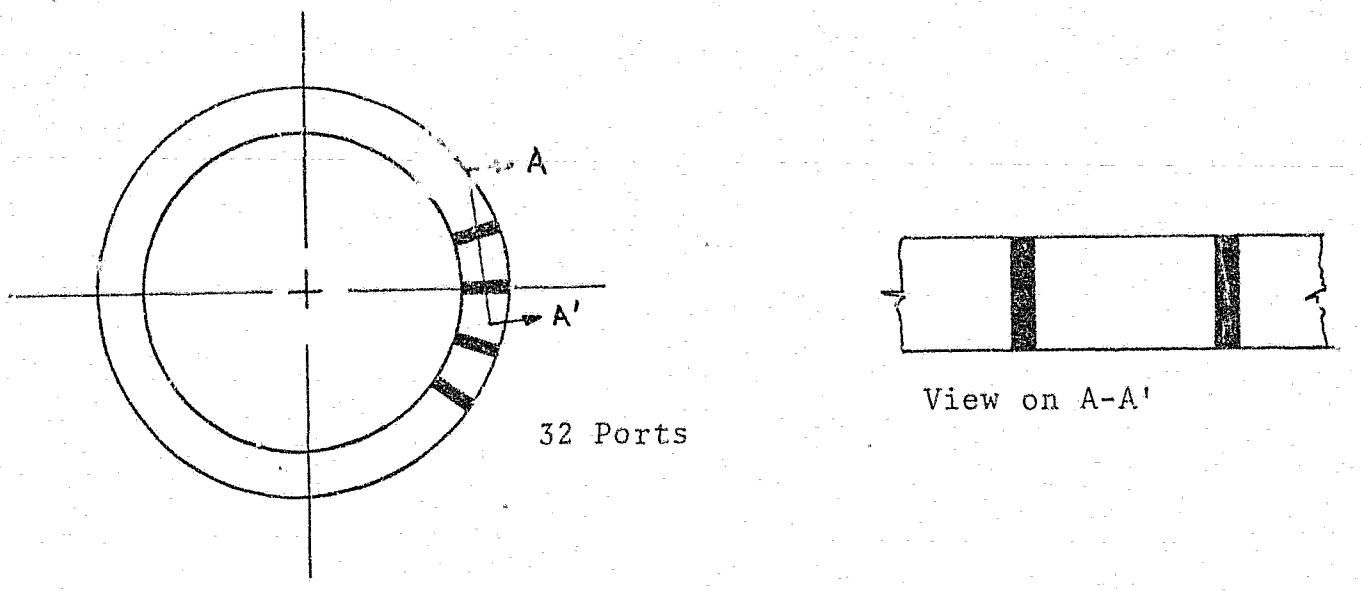
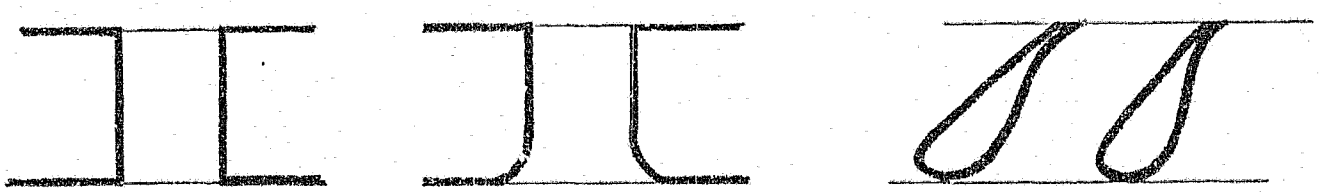


FIGURE 7.3 : Vertical square inlet edged louvre

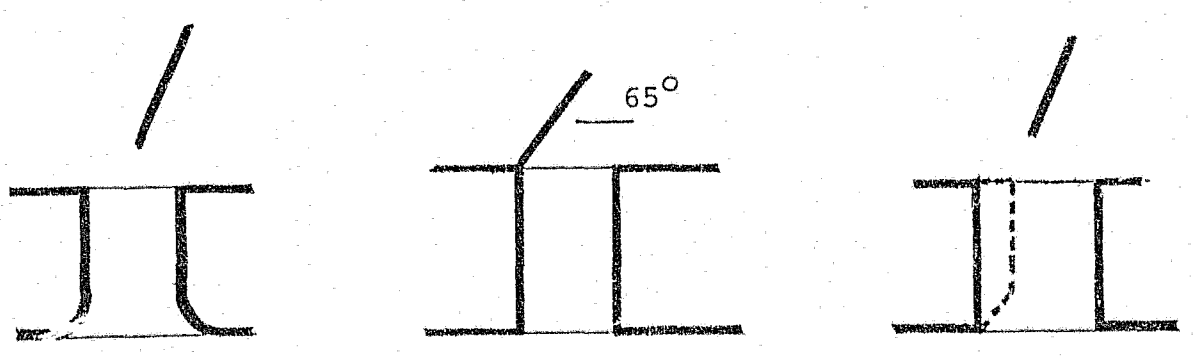


K = 2.01
Vertical square inlet edges

K = 1.10
Vertical rounded inlet edges

K = 1.19
Loesche aerofoil louvre

FIGURE 7.4: The K factors for various shapes tested



K = 1.37

K = 1.71

K = 1.94

FIGURE 7.5: Cone sections fitted above throat

also imparted a swirl component to the rising flow, causing scouring in the mill body. The idea of slanting the aerofoil vanes at 45^{o} was that coal particles thrown forcibly in a downwards direction from the table would have their momentum broken by impact on the vanes, which would result in a lower pressure drop.

The first tests were aimed at increasing louvre velocity by blanking a number of ports, since narrowing the louvre would have restricted the fall of reject lumps into the reject boxes. However, the actual effect was to build up material on the blanked ports, but with no resulting fineness increase. Wear was still high. It was then thought that the high velocities at the throat were responsible for large particles being flung up into the separator area where they were entrained. To prevent this happening, the armour ring configuration was slightly changed.

The original armour ring with an angle to the vertical of approximately 10^{o} appeared as shown in Figure 7.7. A mild steel cone was then rolled and installed above the louvre to give a larger diversion to the air stream. The angle was now $\alpha = 65^{o}$, which corresponded to the slice model configuration (Figures 7.8 and 7.11). This ensured that the air/coal stream would be deflected over the table, thus affording an opportunity for the larger particles to fall out in the low velocity region above the table. This modification was successful in improving performance and cutting down wear on the mill sides.

Next, a series of variations to the inclined vane type louvre were tested, amongst them being the setting of the parallel vanes at 45^{o}, but these modifications were unsuccessful insofar as fineness and throughput did not improve.

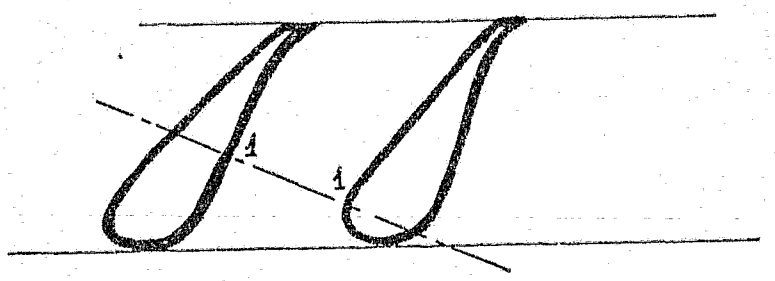


FIGURE 7.6: Original louvre throat configuration.

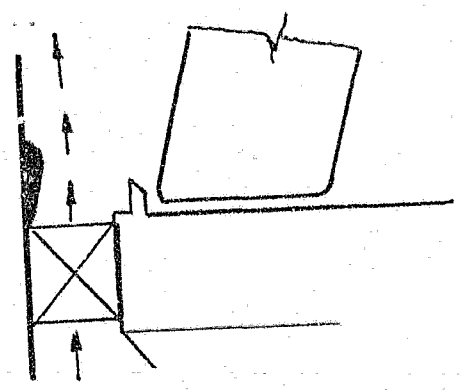


FIGURE 7.7 : Original armour ring

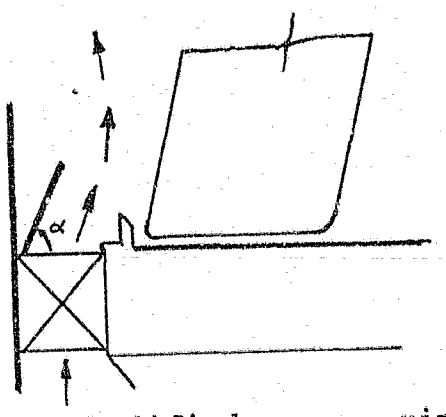


FIGURE 7.8: Modified armour ring

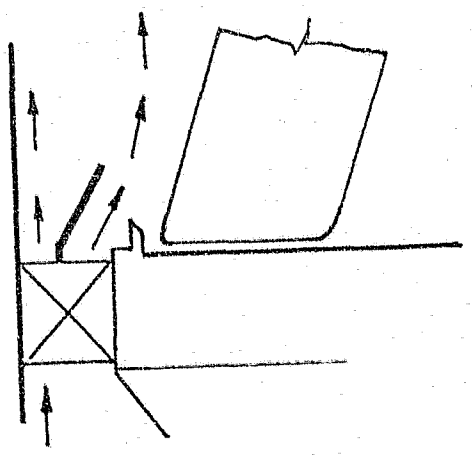


FIGURE 7.9 : Bypass cone

The next step was the installation of the vertical louvre shown in Figure 7.3, the vanes consisting of vertical mild steel plates. By using this type of louvre, the width had to be significantly reduced (the smallest gap tested being 48 mm) to keep the throat velocity high enough to minimise rejects since there was now no swirl component. A sharp entry edge gave a K factor of 2.01, but by rounding this edge, this factor was brought down to 1.10, ie, lower than for the aerofoil. The addition of a mild steel 65^{o} cone also increased the K factor to 1.71. Generally speaking, the fineness value improved, although a wider throat with some blanking had to be installed to prevent reject material lodging in the ports (a legacy of oversize feed coal).

The final configuration was termed the 'bypass cone' and appeared as shown in Figure 7.9 in elevation, the vertical louvre being still used.

This configuration allowed part of the P.A. to bypass the table spillage area and so sweep the sides of the mill body, thus preventing erosion. This cone was now at the same angle, ie, 65^{0}, as the armour ring and it was supported on lugs welded to the louvre vanes to provide a gap large enough for rejects to pass through.

Unfortunately, the coal sizing was very irregular and frequent blockages occurred. However, some tests showed an improvement in fineness and wear. The onload calibration curve was not altered, with the result that at lower loads, the mill rejected heavily, but this problem could easily have been solved if the previously derived curve results had been implemented on all the mills (which was not a feasible proposition at this stage).

It is worth noting that this principle was copied by ESCOM and applied to the Loesche Mills at Grootvlei Power Station,

using the original aerofoil type louvre. Prior to this change there had been extremely severe wear on the mill body, armour ring and louvres, although the coal was considered relatively low in abrasiveness when compared to that used at Arnot. These bypass cones were installed on all Boiler 5 mills at Grootvlei with very good results. Wear has been reported to be drastically cut, and maintenance reduced.

7.1.5 Comment on Full Scale Throat Tests

With reference to the slice model tests, it will be noted that the same principle was applied there, namely, diverting the air stream inwards so as to minimise the Coanda effect. This modification therefore came about as a result of studying visual effects by pitot traversing the flow, and of studying various arrangements in a slice model.

As explained previously, the throat bed voidage should be low. The bypass cone achieves this because of the relatively small throat area in the pick-up zone. It was noted during tests with this configuration that the reject material frequently contained a much larger percentage of small high density particles, this being possible because of the favourable size and density features at lower voidage. As far as operational pressure drop is concerned, this effect can be considered under two aspects:

1) Since the vertical throat should be clear of particles other than those falling into the reject box, the pressure drops over the zones 1 and 2 should be the same (see Figure 7.10):

$$\triangle P_T = \triangle P_1 = \triangle P_2$$

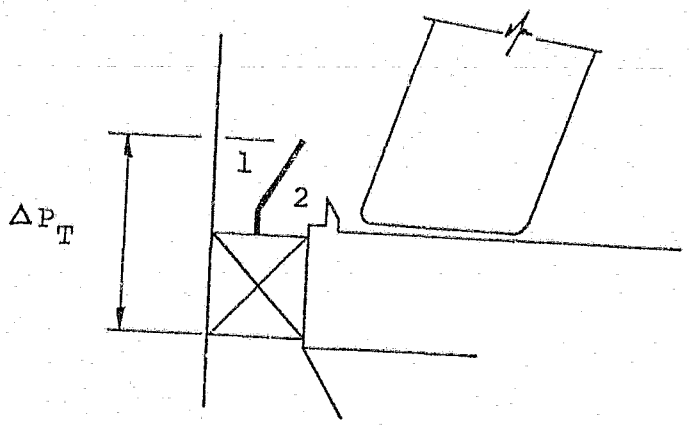


FIGURE 7.10: Bypass throat



FIGURE 7.11: The 65° mild steel armour ring in position

Now $\Delta P_1 = K_{10} v_1^2$

and $\Delta P_2 = K_{11} v_2^2 + L \rho_s (1 - \varepsilon_2) g$

$\therefore \quad K_{10} v_1^2 = K_{11} v_2^2 + L \rho_s (1 - \varepsilon_2) g$

Assuming $K_{10} = K_{11}$,

it follows that $v_1 > v_2$ for $\varepsilon < 1$.

2) As a result, the bypass air velocity will ensure that any large entrained particles will be knocked back into the low velocity area above the table and the fineness value should improve. On the tests conducted, an improvement in fineness was in fact noted.

7.1.6 Mill Operational Temperature gradient

Pressure tappings were drilled down the side of a mill at the vertical positions shown in Figure 7.12 (a). Stainless steel sheathed chrome-alumel thermocouples were installed in these tappings, protruding approximately 130 mm into the mill, and the outputs read on a potentiometer connected via a junction box. The feed and air flow rates were kept constant and the temperatures read for three different roll pressures. It was thought that by adjusting roll pressure, the recirculating load would increase, thereby giving a possible correlation.

The temperature gradient is shown in Figure 7.[illegible] (b). The roll pressure variation did not influence the temperature gradient profile. It was also noted that the temperature dropped rapidly over a short distance at the throat where the hot air entered the mill, thereby indi-

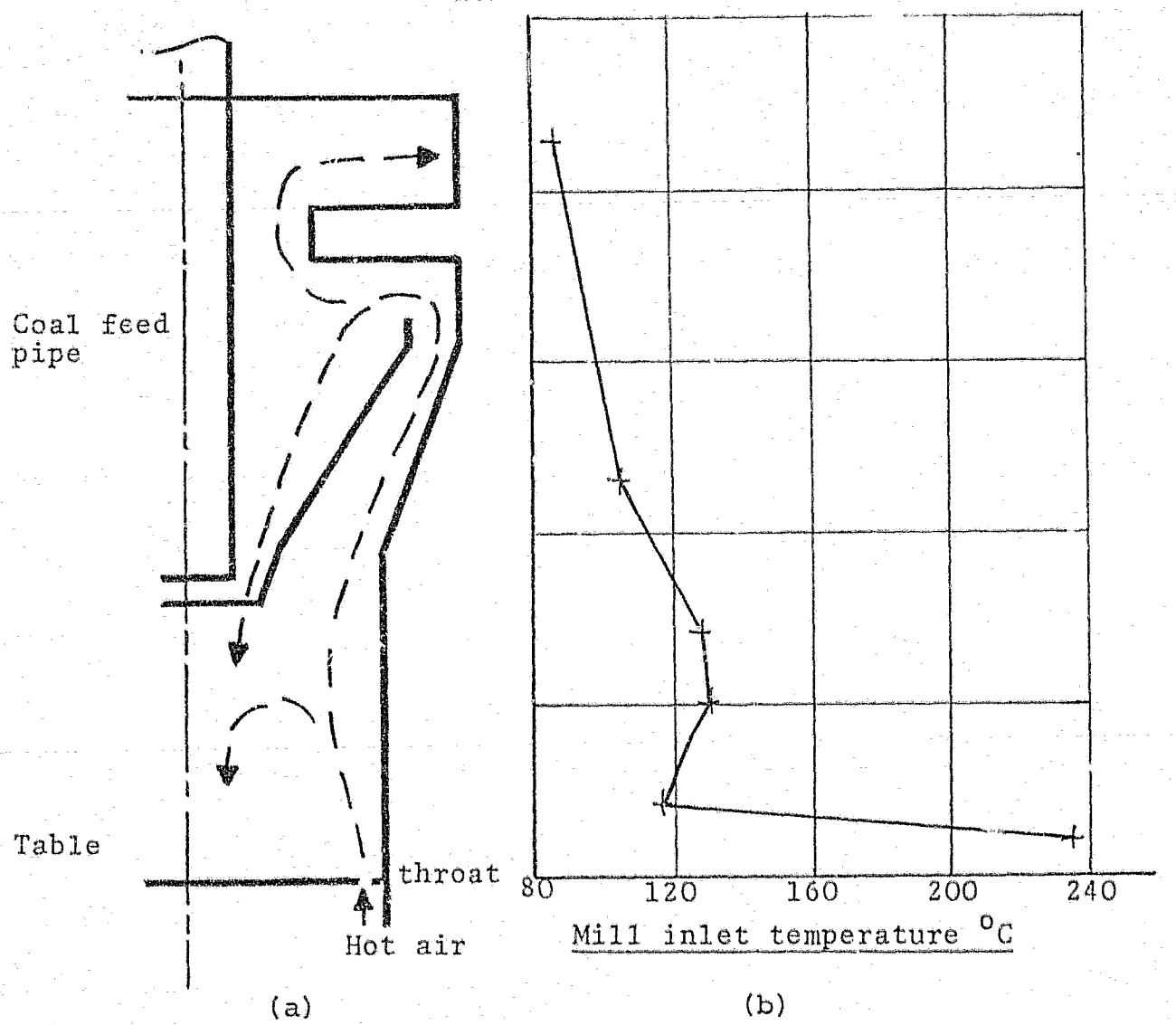


FIGURE 7.12: Experimentally measured temperature profile in Loesche LM18D mill

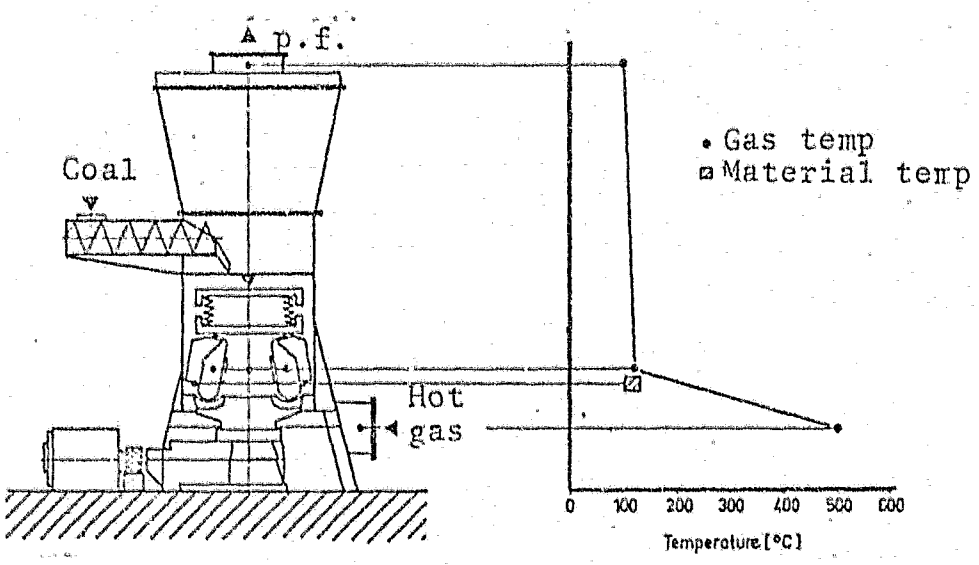


FIGURE 7.13: M.P.S. mill temperature profile

cating that the bulk of the drying action was carried out here.

These results are in line with the curve shown in Figure 7.13, as obtained by Keysselitz (M18) on a Babcock MPS mill. Here the temperature drop was even more pronounced since the feed to the mill must have had a high moisture content. It may, therefore, be assumed that when designing the grinding chamber, the temperature may be effectively taken as the mill outlet temperature without introducing any appreciable error.

7.1.7 Mill Operational Voidage

The same pressure tappings as described in 7.1.6 were used for this series of tests. Pitot-static probes were inserted at varying distances into the mill and the static pressures read on a bank of manometers. In this way, the pressure drop over a known length, and the voidage, could be calculated on the basis of the equation:

$$\Delta P = \rho_s L (1 - \varepsilon) g \quad . . . . . (7.1)$$

The results indicated a fairly uniform voidage increasing up to the separator as would be expected (Figure 7.14). The voidage at a point 450 mm above the throat was also measured. A voidage value of 0.8 was obtained. It is therefore apparent that the voidage changes markedly over a very short vertical distance, and hence the pressure drop over this short length constitutes 90 - 94% of the on-load mill diff.

7.1.8 Establishing Recirculating Load

Since particles are swept from the table to the separator, it follows that the recirculating load could be higher in

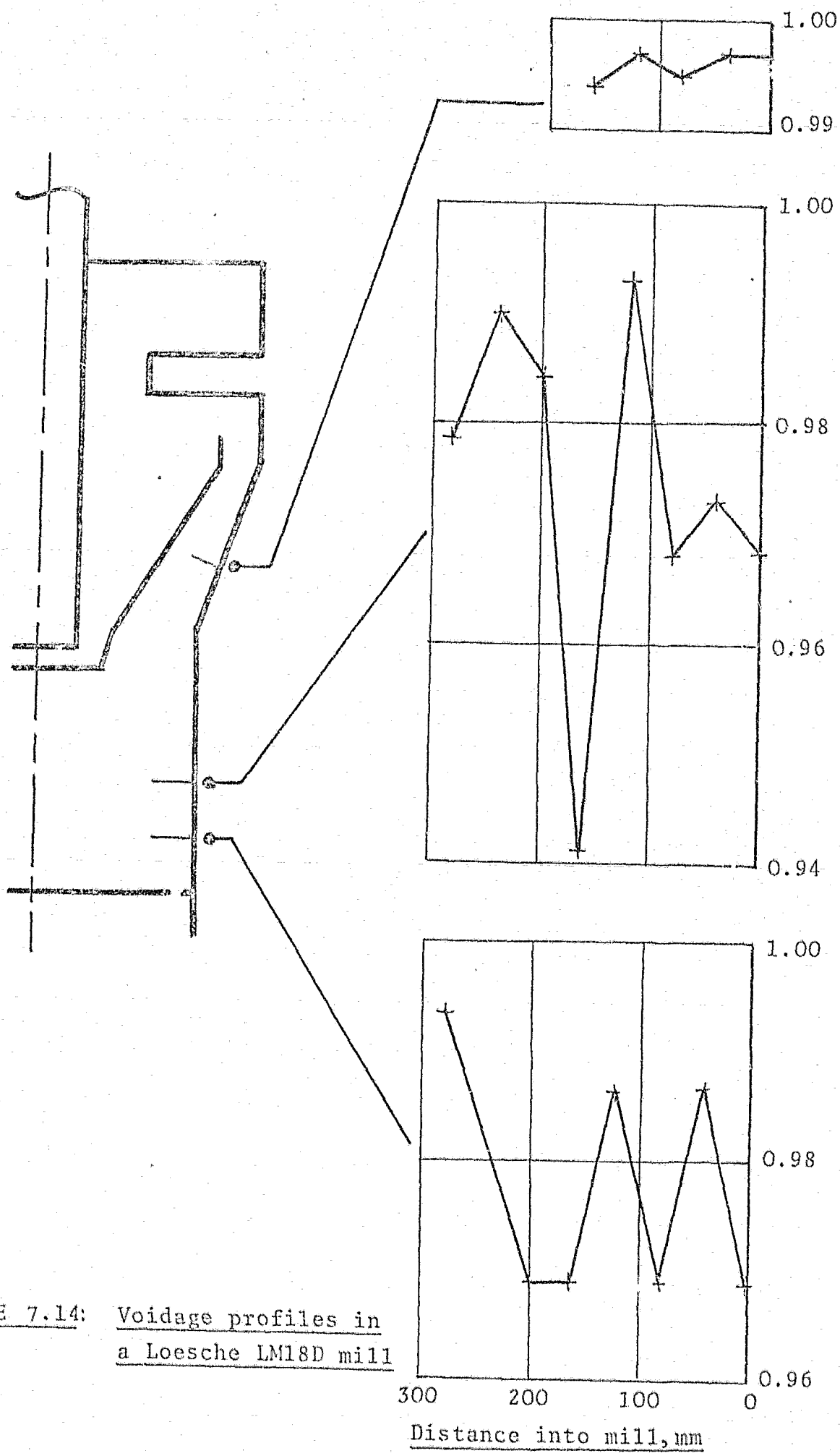


FIGURE 7.14: Voidage profiles in a Loesche LM18D mill

particular operating conditions. It is interesting from an operating and a design point of view to establish an easy and quick method of determining this recirculating load. Let T kg/s be the total coal mass passing to the separator at velocity v m/s.

Then voidage $\varepsilon = 1 - \frac{T}{v\ A\ \rho_s}$ . . . . . (7.2)

From Equation (7.1)

$$\Delta P = L \rho_s (1 - \varepsilon)\ g$$

By inserting two static pressure tappings in the dust stream ΔP can be measured and hence ε determined, and from (7.1), T can be determined.

The recirculating load R_L can then be calculated from

$$R_L = T/T_1$$

Typically, let A = 3 m^2,

ρ_s = 1500 kg/m^3

v = 8 m/s, and

mill output T_1 = 10 kg/s

so for a voidage of 0.996,

$$0.996 = 1 - \frac{T}{3 \times 1500 \times 8}$$

For T = 144 kg/s, $R_L = \frac{144}{10} = 14.4$.

By selecting two points between the separator and the mill body of approximately equal velocity, and at a separation large enough to give a reasonable pressure drop, the recirculating load can thus be calculated as shown

above. In the case of a whizzer type separator, this method cannot be used since the flow paths are not as clearly defined as with a static type separator.

7.1.9 Separator Velocity Traverse

After a few months' operation it became apparent by visual inspection of the mill interior that the wear on the mill conical shell was high. The wear pattern suggested a flow of particles sliding down the sides and being re-entrained at the point where the cone met the cylindrical shell. A pitot traverse on air only was therefore conducted utilising the points already drilled in the shell for the temperature and voidage tests, and Figure 7.15 shows a plot of lines of constant velocity. To the left is a curve showing the area profile or air path area between the inner and outer cones.

On first inspection the area would appear to decrease constantly, but in fact this particular design was incorrect in that the actual area increases between the lower and upper limits. (This point corresponds to the cramped velocity profiles in the central region of the cross-section.) The high velocity profile along the inside of the outer cone also suggests the Coanda effect. It is thus likely that this point was the source of the wear as there might have been recirculation of particles in the lower velocity area, as well as particles sliding back from the upper area of the separator into the high velocity Coanda profiles. Subsequent to the discovery of this incorrect area profile, all future designs have been checked to ensure that the velocity decreases uniformly from the bottom to the top of the separator cone.

It is interesting to compare these profiles with the slice model flows in Chapter 5 (Figure 5.37). The high velocity

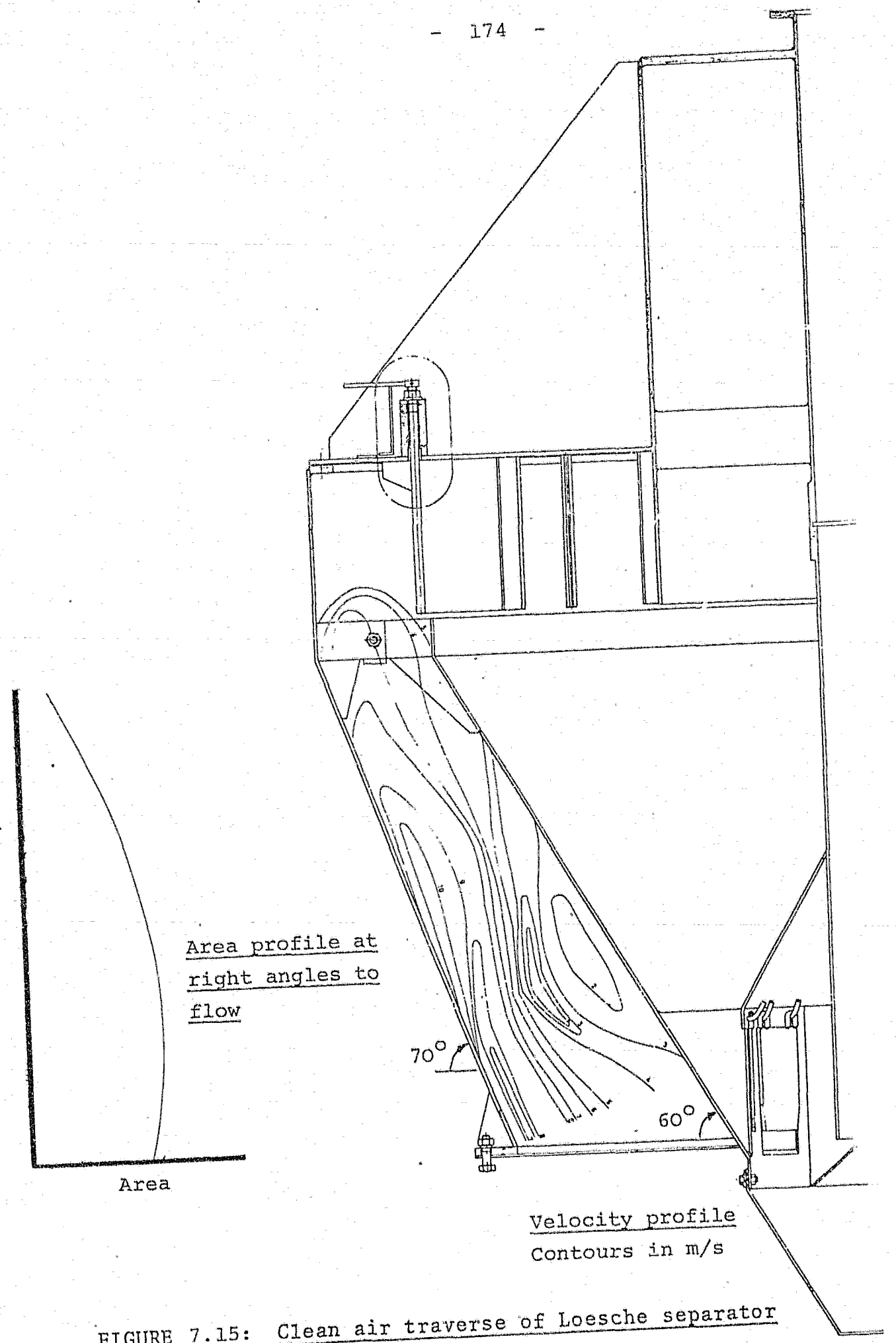


FIGURE 7.15: Clean air traverse of Loesche separator

area on the Lopulco Mills appears to be on the inner cone, perhaps due to the different angle of divergence from the vertical of the mill body (30^{o}, as opposed to 20^{o} for the Loesche design).

7.1.10 Separator Performance

The efficiency of a separator in giving an acceptably sized product depends on a number of parameters, these being as follows:

- inlet vane velocity
- outlet velocity
- outlet sleeve height
- cone geometry

In the Loesche separator the vanes are situated as shown in Figures 7.15 and 7.16. By assuming the velocity direction as parallel and horizontal to a vane, the paths of all vane flows form a circle of radius r. Now the centrifugal force on a particle travelling in direction v_{12} is proportional to v_{12}^2/r, so it will be noted that the greater the inclination of the vanes to the radius, the higher becomes the velocity due to the smaller area between the vanes. This is shown in Figure 7.17. For a larger inclination, r will therefore increase. Also plotted is the function v^2/r which takes the form of a parabola with a turning point at an inclination of approximately 34^{o}. (The velocity was taken as unity at zero inclination for ease of representation.)

It will also be noted that at an angle of 33^{o}, the vane flow impinges directly onto the outlet sleeve, an operational condition not very satisfactory from both a fineness and wear point of view. Thus the favourable centrifugal function v^2/r at angles lower than 33^{o} must be dis-

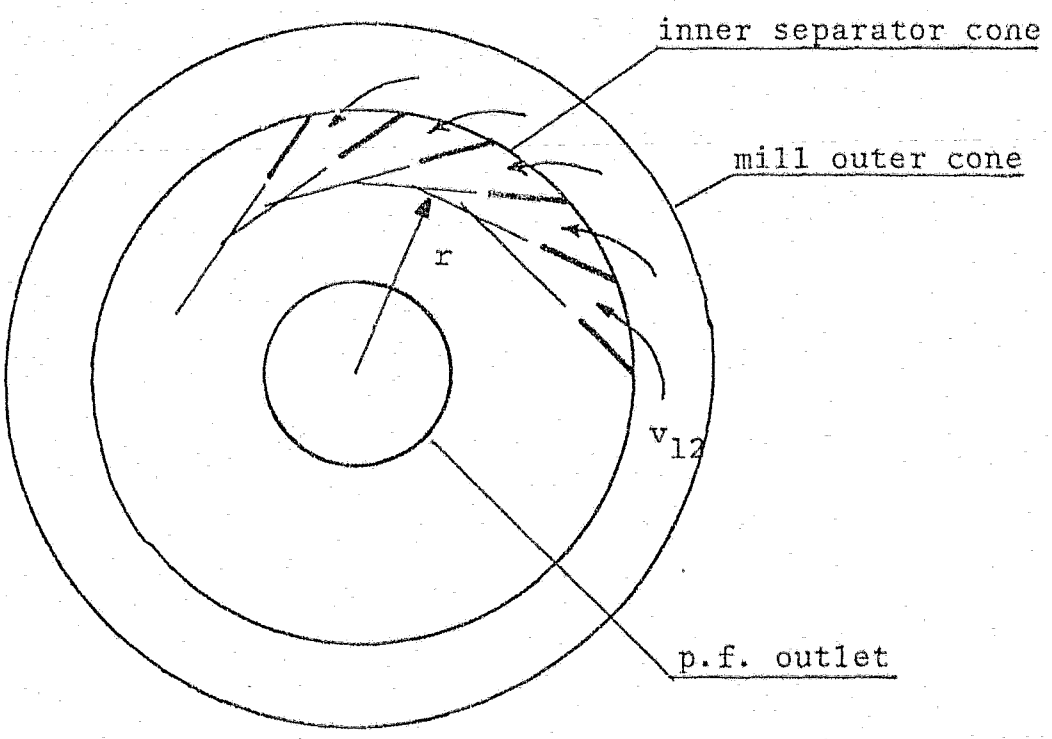
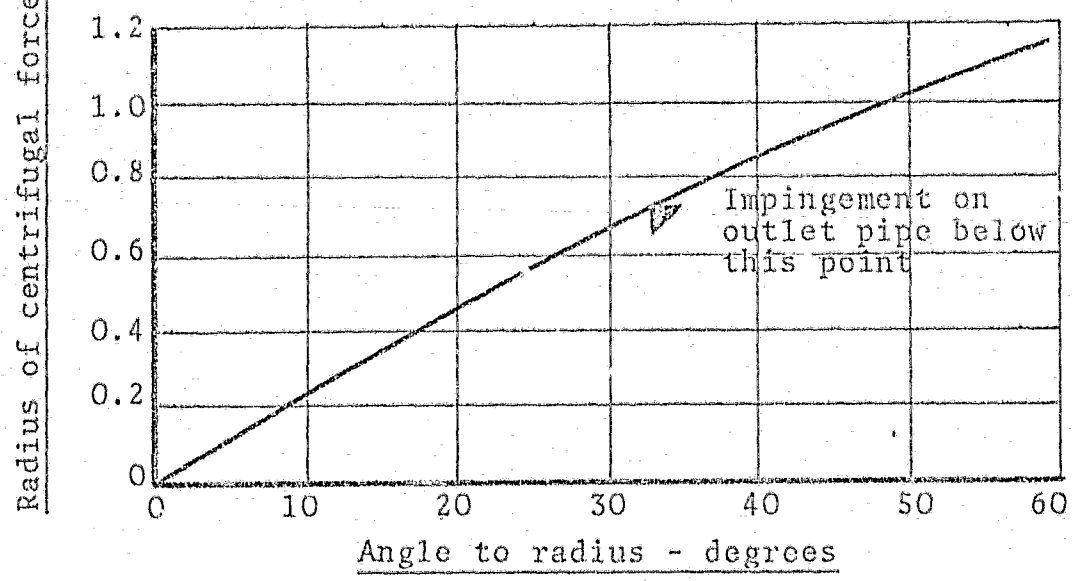
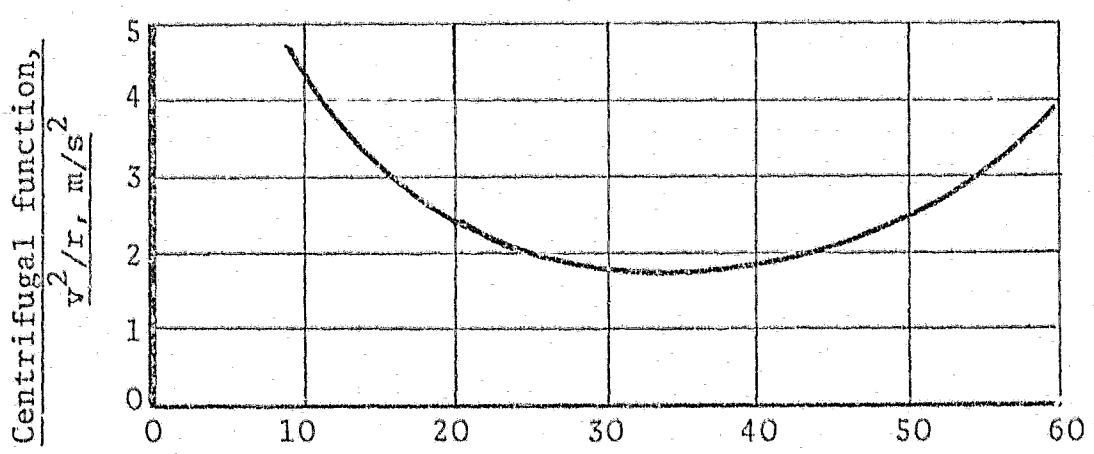


FIGURE 7.16: Flow pattern in vanes

carded unless a smaller outlet pipe diameter is used. This in turn depends on outlet velocity and feed chute size since the feed chute runs down the centre of the mill. The vane geometry is therefore important in influencing the performance of a separator and hence the separator should be sized to utilise the steep v^2/r characteristic without undue loading of the mill with oversize material.

The position of the outlet sleeve relative to the inlet vanes will also influence particle fineness by virtue of the downward velocity of a particle, as shown in Figure 7.15. Obviously, the lower the sleeve, the higher the pressure drop, but also the finer the product, as shown in Figure 7.18. Because of ease of operation, the vanes are used to control fineness, with the sleeve being used to give the fine adjustment perhaps necessary if too high a pressure drop is to be avoided.





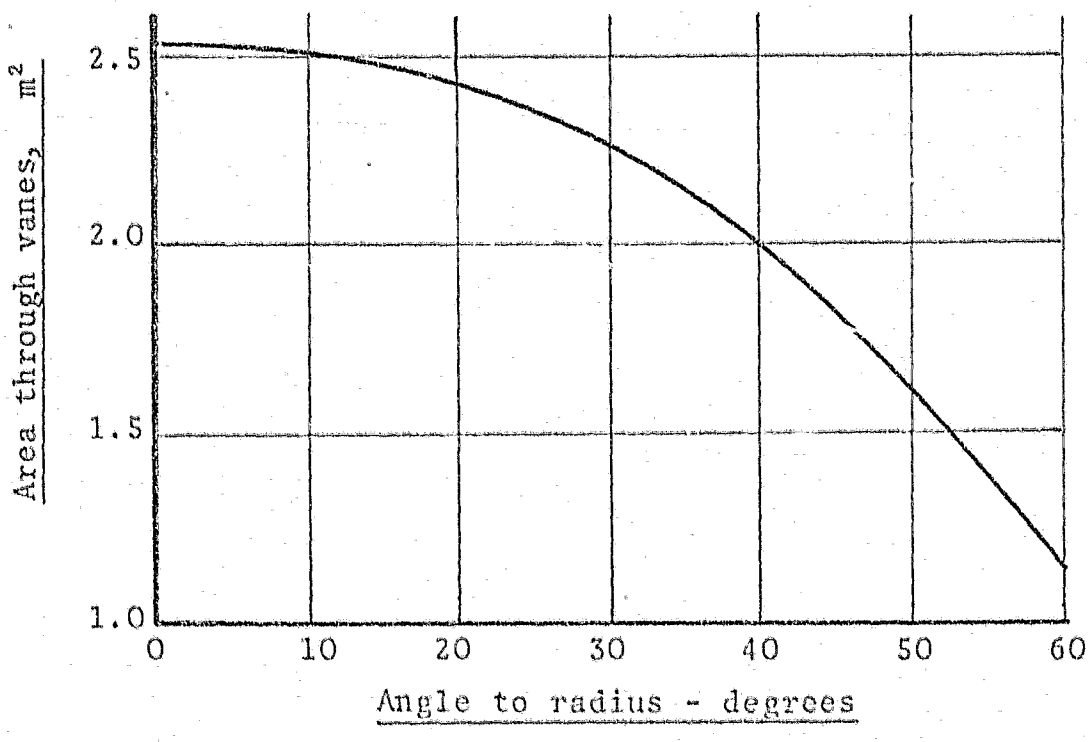


FIGURE 7.17: Separator characteristics for Loesche LM18D mill

7.1.11 Roll Speed

The rolls are rotated by the table, and as explained previously, there is only one point on the roll face in pure rolling contact with the table. Therefore, depending on the roll pressure, this rolling point will change, resulting in a change in roll speed. Obviously, the faster the roll rotates (for a fixed table speed), the more grinding will be accomplished, which results in a higher throughput and possible improved fineness.

Since the roll pressure can easily be adjusted on load, the roll speed was measured at four roll pressures for a fixed mill throughput. Mill power consumption was also noted. The roll speed was measured by counting the impacts of a steel plate welded onto the rear of a roll on a rod inserted through the roll cover. The results are shown in Figure 7.19. The increased rolling friction resulted in a substantial power increase and this must be weighed against fineness and possible throughput improvement per kW absorbed. It appears that a roll pressure of 45 bar gauge will give the same relative speed, and therefore grinding increase, as power increase.

7.1.12 Coal Characteristics in Relation to Wear

The one overriding factor in improving the performance of the mills was to reduce maintenance costs whilst at the same time maintaining acceptable throughput and fineness using a run-of-mine unwashed coal that was outside abrasive specification limits. The standard abrasive tests carried out on the coal by the laboratory were the Hardgrove and Abrasive tests (these tests are outlined in the Appendix). It has long been argued whether in fact the Abrasive Index has any real merit other than a local comparison of run-of-mill coal. With this in mind, an inves-

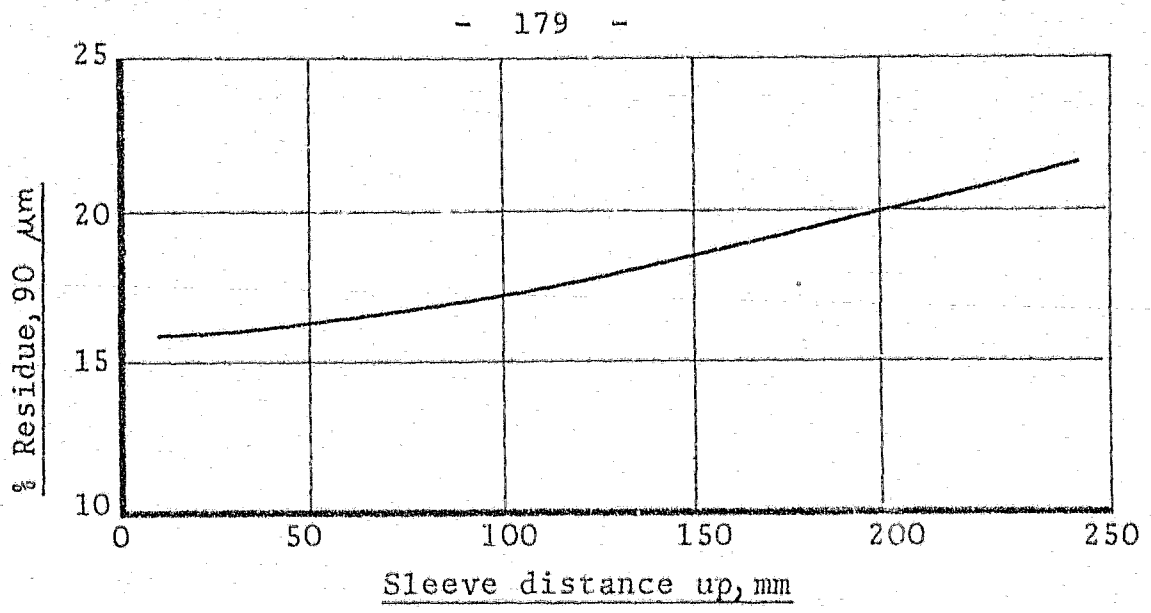


FIGURE 7.18: Fineness variation vs outlet sleeve position

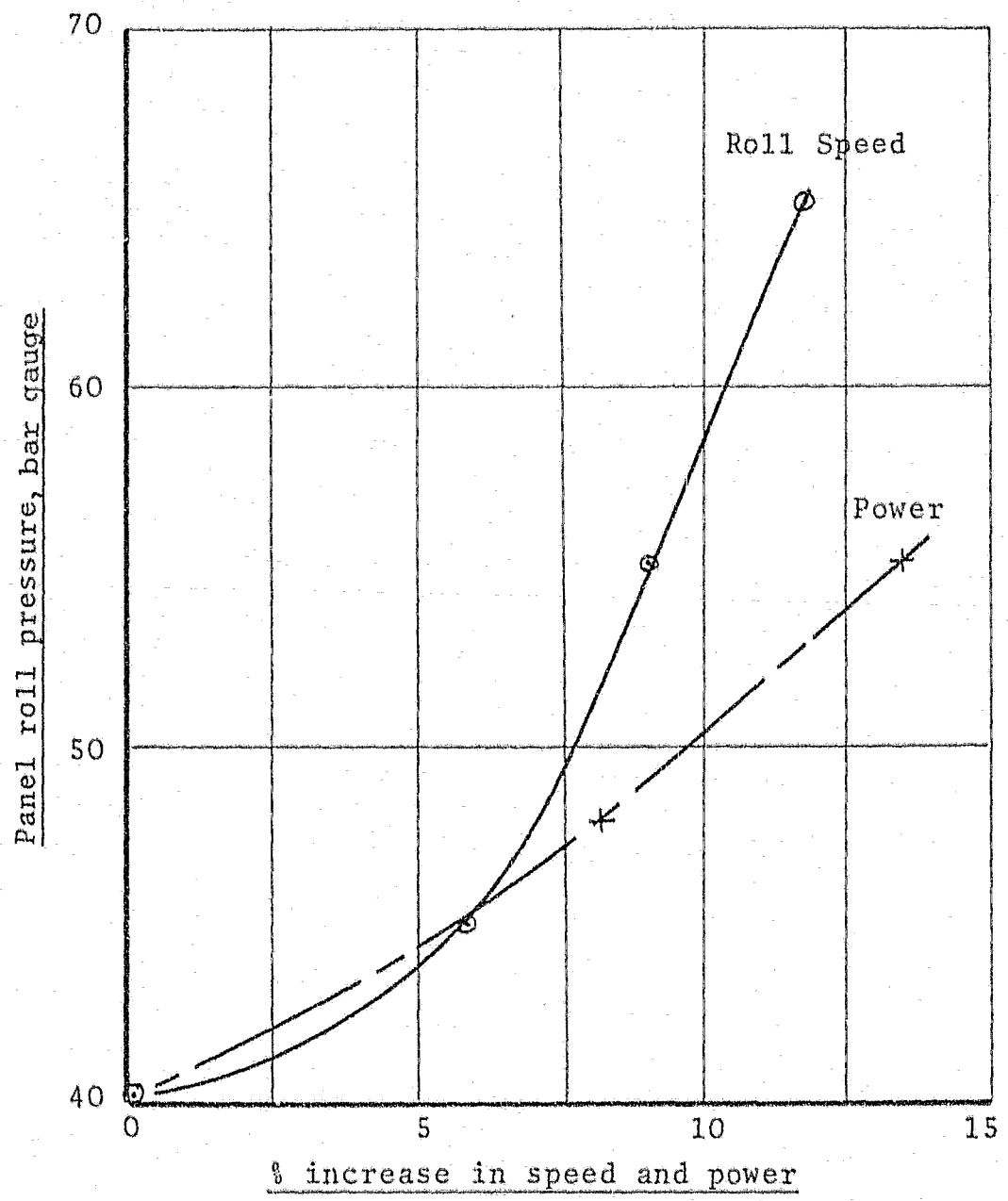


FIGURE 7.19: Effect of roll pressure variation on mill power and roll r/min

tigation into milling costs at five power stations which used widely varying coal quality and utilised a number of types of mill was conducted.

Cost and coal figures for the milling plant were taken for the eighteen month period from June 1972 to November 1973. When total running cost was plotted against Abrasive Index, it was possible to establish the relationship shown in Figure 7.20. When cost was split into labour and material (the latter being a function of wear), a further relationship was also evident. Therefore, allowing for inaccuracies in the Abrasive Index, as must occur it was nevertheless shown that this Index is extremely useful when correlated to the right parameters, and that wear rates and thus costs can be predicted to some degree by noting Abrasive Index trends. Using a modified throat ring which gave a higher mass of rejects, it was found that by increasing the mass of rejects sevenfold, roll wear was noticeably reduced. In this case the main debris was pyrites and dolomite rock. Abrasive Indices as high as 700 were recorded for the raw coal, compared to the specification figure of 253. Furthermore, no direct relationship between Abrasive Index and Hardgrove Index nor between Abrasive Index and free moisture content was evident (Figure 7.21).

7.2 CAMDEN TESTS

The mill model studies were based on the Lopulco mill configuration, these mills being installed at Camden Power Station. Unfortunately, by the time that the laboratory studies were completed, the mills were fully operational and further full scale tests on the scale envisaged were not possible. However, certain areas were studied concurrent with the laboratory tests, these being:

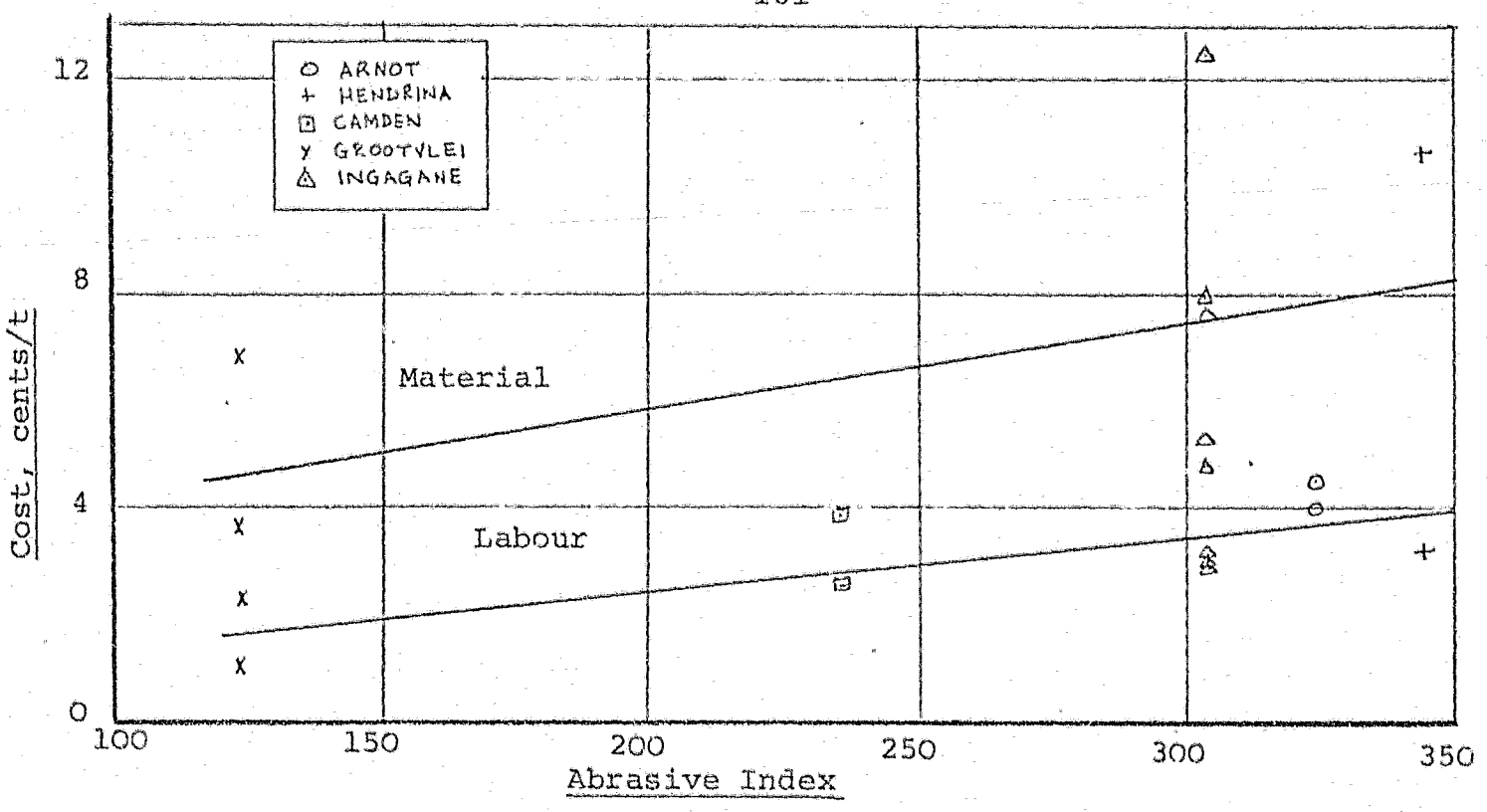


FIGURE 7.20: Cost correlation from South African power stations (from M21)

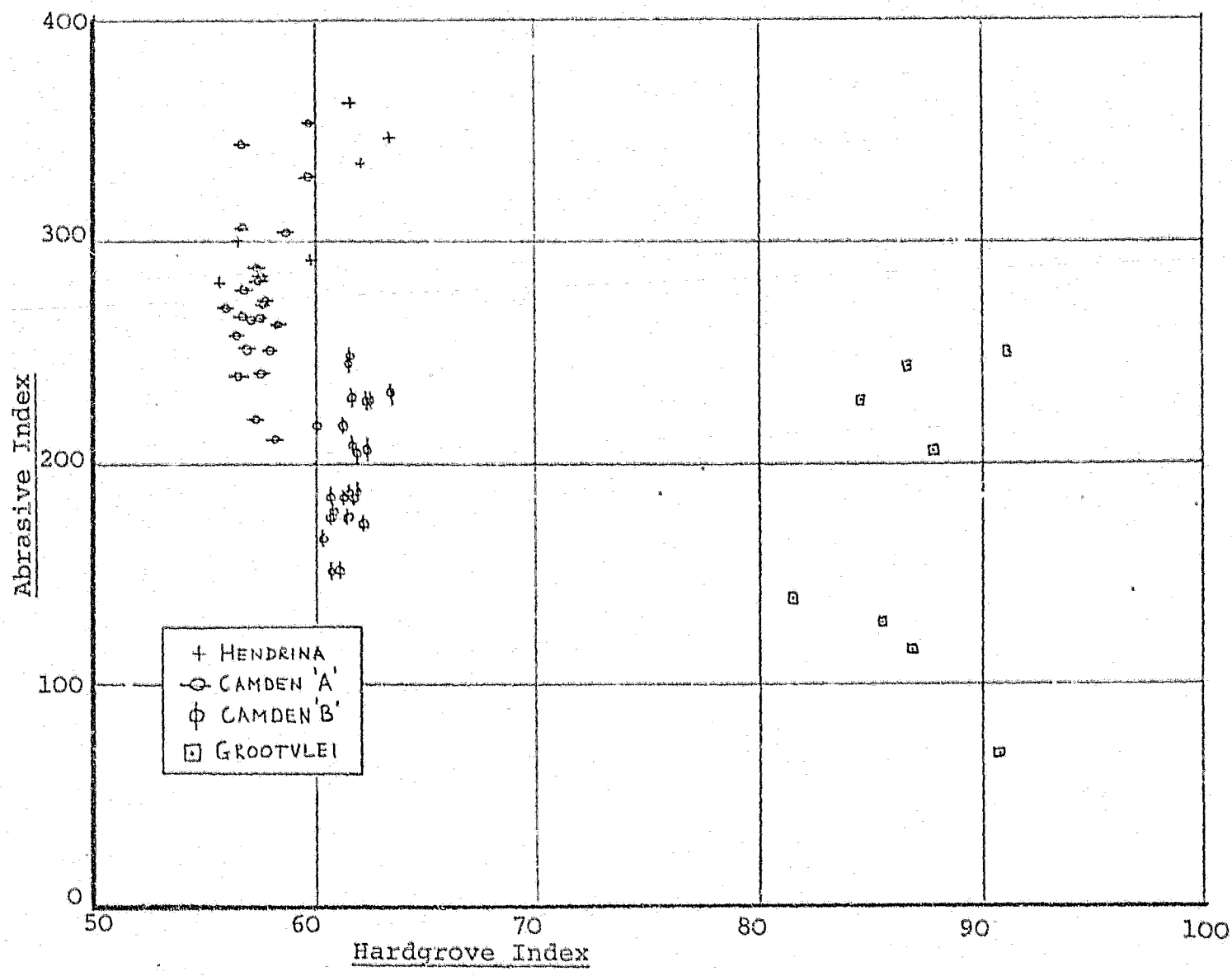


FIGURE 7.21: Correlation of Hardgrove and Abrasive Indices (from M21)

(i) sampling methods

(ii) coal labelling

and an analysis of results obtained on the mills by others was also made.

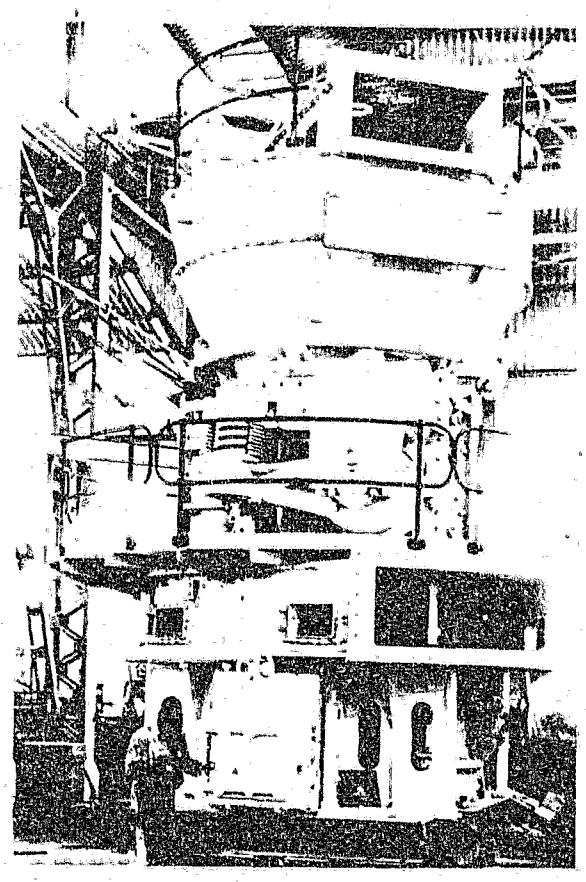


FIGURE 7.22: Lopulco Mill assembled in works

7.2.1 Principle of Operation of Lopulco LM 14/3P Mill (Figure 7.22)

Raw moist coal from the bunkers enters the rotating table feeder which discharges the coal at a controlled rate by means of an adjustable sweeping arm down a central feed chute into the mill. The rotating mill grinding table

throws the coal under spring-loaded free running rolls set at an initial small clearance off the table. The crushing action reduces the coal to a powder which spills over the rim, or dam ring, of the grinding table.

Hot P.A. discharges from the rotating annular throat around the table and sweeps the pulverised fuel into the body of the mill. Some oversize material falls back on to the table, and further oversize is returned by the centrifugal action of the rotating whizzer separator blades mounted above the grinding chamber.

The pulverised fuel of required fineness is conveyed out of the mill via one pipe and is split into individual pipes by means of splitter vanes. Each mill supplies four burners, all on the same horizontal level at the furnace front wall. Reject material is discharged from the mill through the annular throat and swept by ploughs, attached to the rotating table, into two reject bins.

7.2.2 Sampling

7.2.2.1 Introduction

Mill performance is judged by the fineness of the pulverised fuel at the rated mill load. If this finess drops, then combustion problems as well as boiler losses are encountered. To enable the forty mills at Camden to be operated at optimum conditions, and to check this, required a great deal of time for sampling p.f. What was therefore needed was a quick and reliable p.f. sampling method. The best possible method would be continuous sampling at a number of points simultaneously, using isokinetic sampling. It had earlier been established by others that by setting the withdrawal rate at the average velocity as calculated from the total air flow, a

sample within experimental accuracy limits was obtained. Stratification within the p.f. pipes was likely to cause greater errors than that involved in not knowing the exact isokinetic withdrawal velocity; thus a continuous sampler should be more accurate and simpler to operate.

7.2.2.2 Rotating Arm Sampler

The first type of sampler used was of a rotating arm type, with 10 sampling nozzles inserted through the 100 mm diameter pipe pocket above the riffle boxes. The arm was swivelled around by means of a pulley arrangement operated by hand from outside the pipe (Figure 7.23). The isokinetic sampler was connected to this probe and a sample drawn through the 10 nozzles simultaneously whilst rotating the arm through a 360° arc within the pipe.

The main drawback with this system was the difficulty of inserting the probe into the pressurised line when the mill was operating. The probe had also to be accurately positioned, otherwise the arm fouled the pipe side. P.f. also tended to clog the rotating parts although special seals were provided to prevent this from happening. An air seal was tested without success, and the best method appears to be the pressurised box design developed by the C.E.G.B. (Snowsill, P19).

In the face of these drawbacks, it was decided that a permanently installed probe would serve much better and the rotating arm sampler was not further used.

7.2.2.3 Sliding Arm Sampler

The next sampler was tested as a permanent installation on a mill (Figure 7.24). The probe was installed in the rectangular mill outlet, and consisted of a pipe with 10

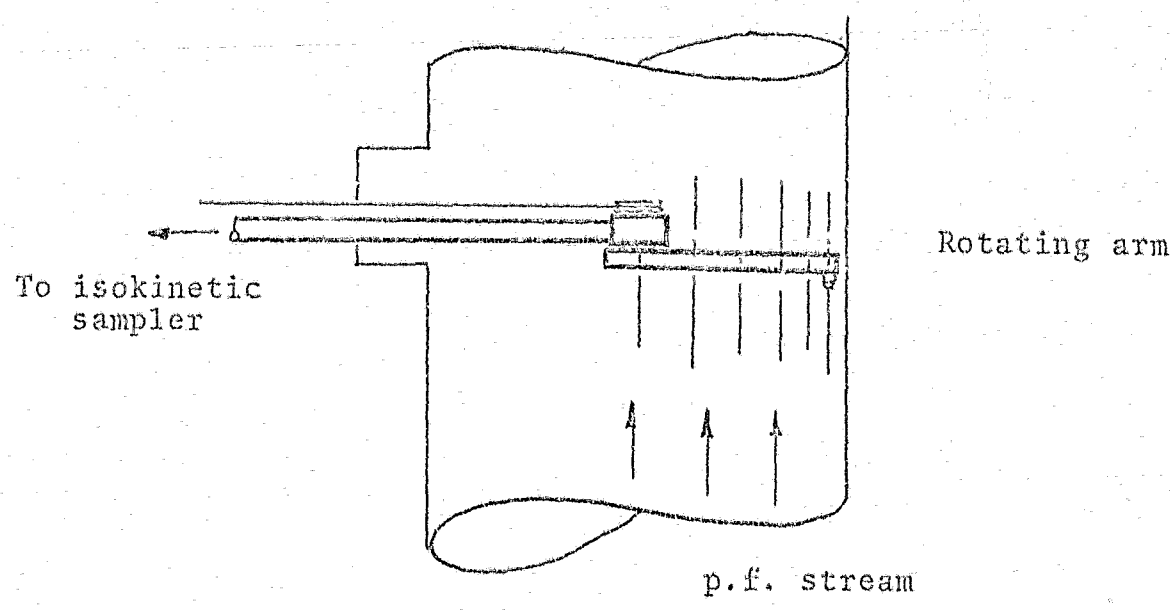


FIGURE 7.23: Rotating arm sampler

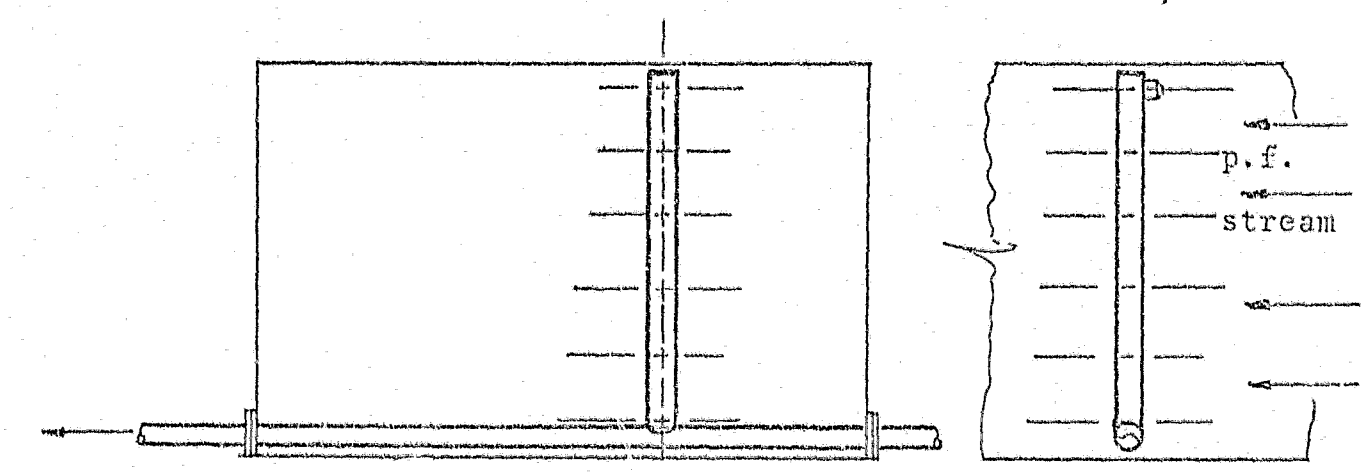


FIGURE 7.24: Sliding arm sampler

nozzles which could be directed into the p.f. stream, this pipe being in turn connected to a sliding pipe so that the nozzles would traverse the complete mill outlet area. When not in use, the nozzles were swung downwards out of the p.f. flow. Again the probe was connected to the isokinetic sampler and the average withdrawal velocity used. Two tests were plotted on a Rosin-Rammler graph to give an indication of the sample distribution (Figure 7.25). The distribution is as good, if not slightly better than, the standard sampling results.

This method was thus more satisfactory from an operational point of view, but would involve fitting probes to every mill as a permanent feature. Difficulty with the station air supply, necessary for operating the sampler, prevented further comparative tests at this stage.

7.2.3 Coal Labelling

Isotopes and radioactive elements have been used extensively in industry to trace flow paths and measure trace products with great accuracy and ease of detection. It was decided to test the Camden coal for its response to radioactive bombardment and then use it as a tracer to measure retention times in the mill. A sample of coal was therefore activated at the Atomic Energy Commission at Pelindaba, and counts were taken over a number of days. From these, the half-lives of various elements were clearly evident when plotted on a semi-log scale of time vs logarithm of counts for various electron-volt values (Figure 7.26).

Elements possibly present and indicated by half-lives were:

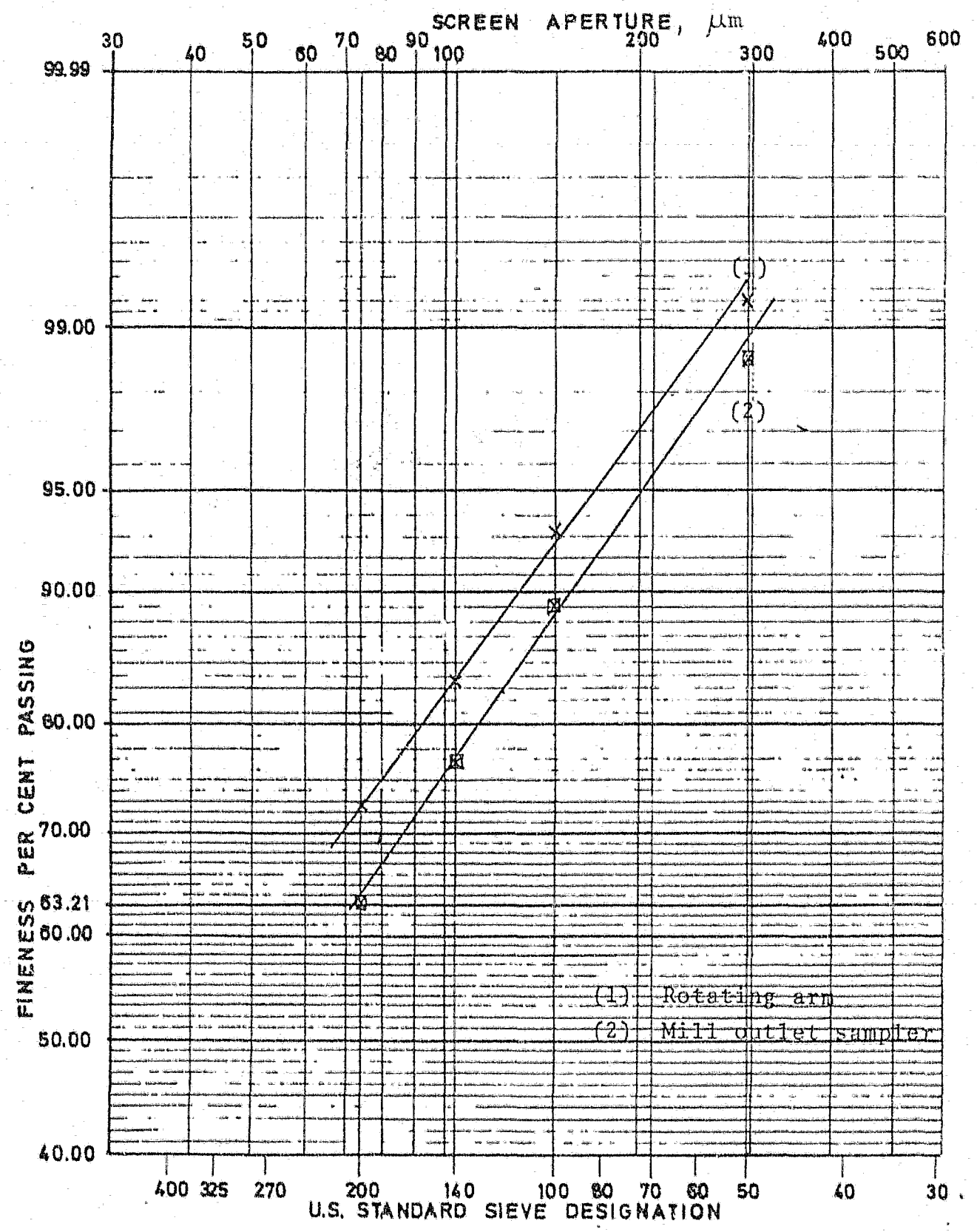


FIGURE 7.25: Sampler test results

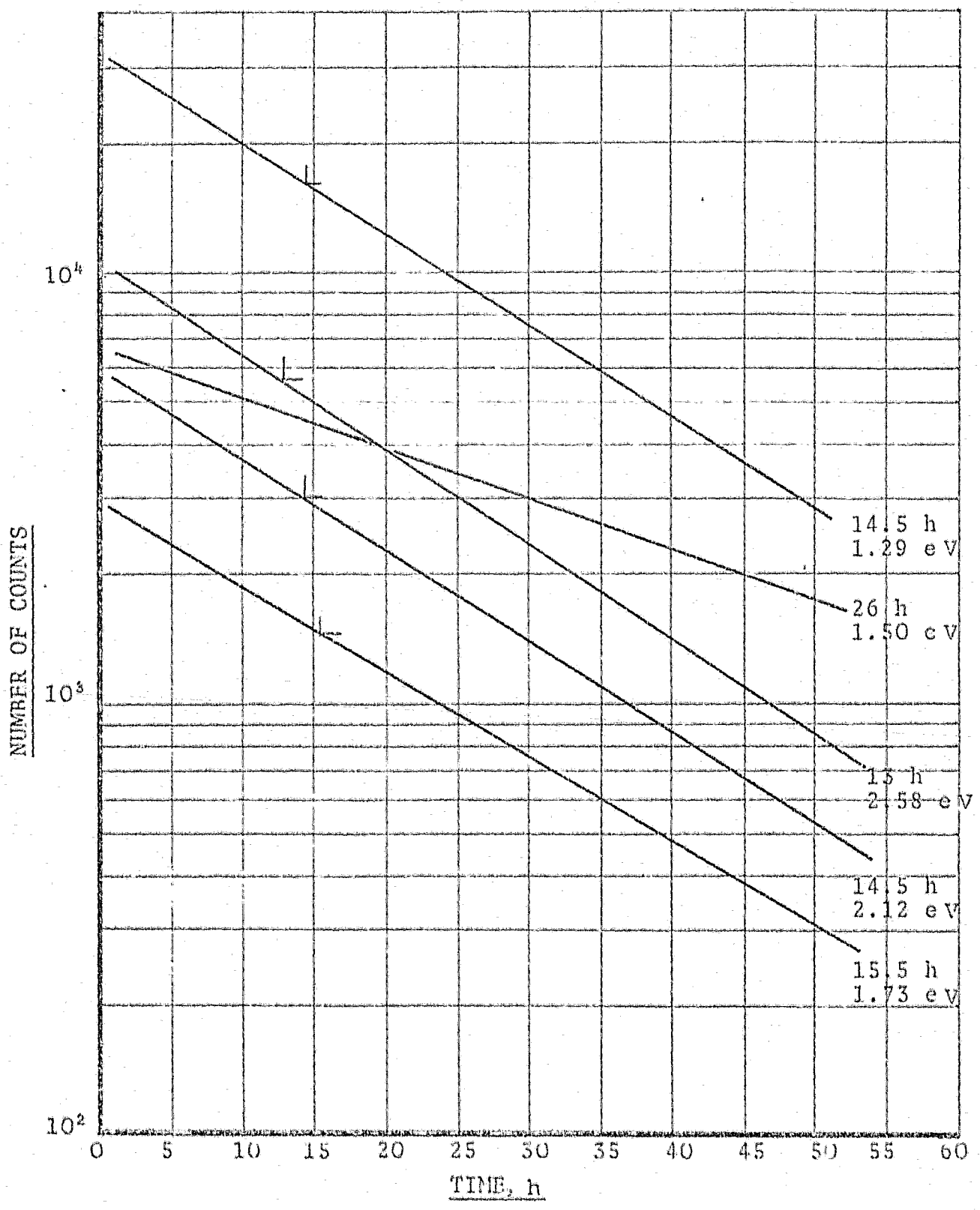


FIGURE 7.26 : Time vs Number of counts for irradiated Camden coal

Cu^{64} - 13 h (1.34 MeV)

As^{72} or As^{76} - 27 h (0.58, 1.2, 1.76, 2.02 MeV)

Na^{24} - 15 h (2.76 MeV)

The conclusion reached from this test was that the coal would make a good tracer if used immediately. Counters set up at the feed inlet and p.f./air exit would pick up at least some of the counts when the coal passed, and this intensity would indicate the amount passing through the mill on a time basis. Unfortunately, the tests could not be carried further due to the expense and non-availability of equipment necessary for on-site tests at that time.

It is interesting to note that irradiation techniques were used by Gardner and Austion (G17A) in studying batch grinding. Whilst irradiation had a negligible effect on the grinding properties of the three coals studied, selective grinding did take place due to the impurities in the coal, and any tests would have had to allow for this inconsistency in evaluating grinding results of irradiated feed.

7.2.4 Interpreting Mill Results

When testing a mill, there are numerous dependent and independent variables to be considered in order to optimise operation for maximum fineness and throughout with minimum power consumption and reject losses.

The independent variables are:

- Air/fuel ratio
- Dam ring height
- Number and width of whizzer blades
- Whizzer speed
- Spring torsion (roll pressure)

- Louvre throat gap
- Load

The dependent variables are:

- Mill differential pressure
- Product fineness
- Power consumption
- Reject quantity and quality

With so many variables, it is not easy to extract trends and optimum operating points. Numerous graphs have to be drawn and interrelated effects are always present. An alternative new system of presenting data was therefore sought which would isolate the most important mill parameter, namely product fineness, to serve as an indicator of the optimum points of all other operating parameters. For this purpose the uniformity coefficient n, was used, as well as the average particle size, as determined by the equation

$$Ag = x_o / \sqrt[n]{1.781}$$

The present system of setting up a mill for optimum conditions hinges around the interpretation of the sample sieve analysis obtained under specific conditions. As has been noted, the uniformity coefficient n is the slope value of the line on the Rosin-Rammler plot, and is an indicator of the spread of the size distribution. Combined with average particle size, these two figures will indicate definite trends in the variations of the operating conditions.

Graphs E1 to E11 are presented in the Appendix along these lines using results obtained by others on the Camden Mills. The full report on this investigation is given in M15.

7.3 CONCLUSIONS FROM INDUSTRIAL TESTS

(i) A series of tests to optimise louvre throat configuration emphasised the importance of this part of the mill on overall performance. A new concept in design was successfully tested and installed (at Grootvlei) as a permanent modification, this being the bypass cone configuration.

(ii) To reduce wear, the air/coal mixture must be diverted towards the centre of the mill by the throat configuration. This allows oversize particles to drop back on to the table.

(iii) The entrance configuration of the throats tested was most important in achieving a low K factor, ie, pressure drop. Well rounded edges and low plenum velocity (approach velocity) are desirable.

(iv) The temperature gradient within the mill is very steep directly above the throat, and the mill body temperature can be taken as the outlet temperature.

(v) Voidage within the mill plenum and separator was high, and the pressure drop through the mill can therefore be taken as being due to the fluidized bed immediately above the throat.

(vi) The velocity distribution in the separator led to high wear due to recirculation. The design of the flow area was faulty, and this should be checked in future applications.

(vii) The geometry of the separator vanes in relation to the outlet pipe will determine to a large extent the separator efficiency by imparting centrifugal force without undue pressure drop. Impingement onto the central pipe was a possibility within the normal operating limits of vane settings.

(viii) Sleeve adjustment on the separator outlet pipe can beneficially influence performance.

(ix) The method of plotting uniformity coefficient n' and average particle size derived from n' simplifies the interpretation of the various milling parameters.

(x) The possibility of using permanent type multi-nozzle samplers should be investigated further with a view to their being corporated as a built-in feature in the m_ system.

(xi) Irradiated coal can be used as a tracer in any residence time tests provided that the coal is used immediately, since tracer element half-lives are relatively short.

(xii) Model tests proved beneficial in showing possible solutions to prototype problems and in the Arnot tests model solutions were able to be put to practical use.

(xiii) The Abrasive Index provides a useful trend when establishing relative maintenance costs.

CHAPTER 8

DISCUSSION OF DESIGN CONSIDERATIONS

8.0 INTRODUCTION

From the present study it has been noted that certain areas of importance on mills can be improved by detailed study, using both models and prototype testing. Of particular note have been throat design and separator performance, since the throat dictates the pick-up zone efficiency, and the separator allows correctly sized particles to leave the mill. Inherent in these two features is the wear within the mill and the rejection of non-combustible material to outside the grinding zone. Therefore, this chapter will briefly survey possible avenues of development of milling plant, bearing in mind some of the problems encountered here, and also the fact that this type of development requires time and extensive capital expenditure.

8.1 FUTURE DESIGN CONSIDERATIONS

The following appraisal of future trends is applicable more to the vertical spindle type mill, although it is realised that the problems facing the tube mill designer are, in some cases, similar. Due, however, to the increased popularity of the vertical spindle mill, and indeed its suitability to many industrial applications formerly fulfilled by tube mills, the present and future development of this type mill is considered of prime importance, and it is in this field that the application of new ideas and methods will prove most fruitful.

What the mill manufacturer aims for is the lowest power consumption per tonne of product ground, coupled with efficient operation, low maintenance, and obviously a competitive selling price.

One of the largest vertical spindle mills with which the author's company was associated was installed in Japan in a cement works, where it grinds raw cement meal at the rate of 210 t/h to a fineness of 10% residue on 90 µm. This is a four-roller type Loesche LM32 mill driven by a 1500 kW motor through a reduction gearbox. Figure 8.1 shows the mill and Figure 8.2 the size of the gearbox. The rolls are hydraulically loaded with the spring effect provided by nitrogen filled accumulators in the hydraulic circuit.

There are mills in operation with higher capacities than this but it must be remembered that capacity is governed by the type of material (Hardgrove Number) and the fineness of the final product, and on this basis it is felt that 300 - 350 t/h is probably the biggest capacity the present design of mill is capable of being extended to without radical changes or new design concepts.

The trend of growth in the milling industry favours single units with high availability for the following reasons:

- Lower capital cost of milling plant.
- Lower capital cost of auxiliaries, such as ducting, hoppers and instrumentation.
- Probable reduced maintenance costs and spares holdings.

The disadvantages are that, for example, in a cement plant the whole operation depends on the availability of the mill and a mill shut-down of any duration would mean

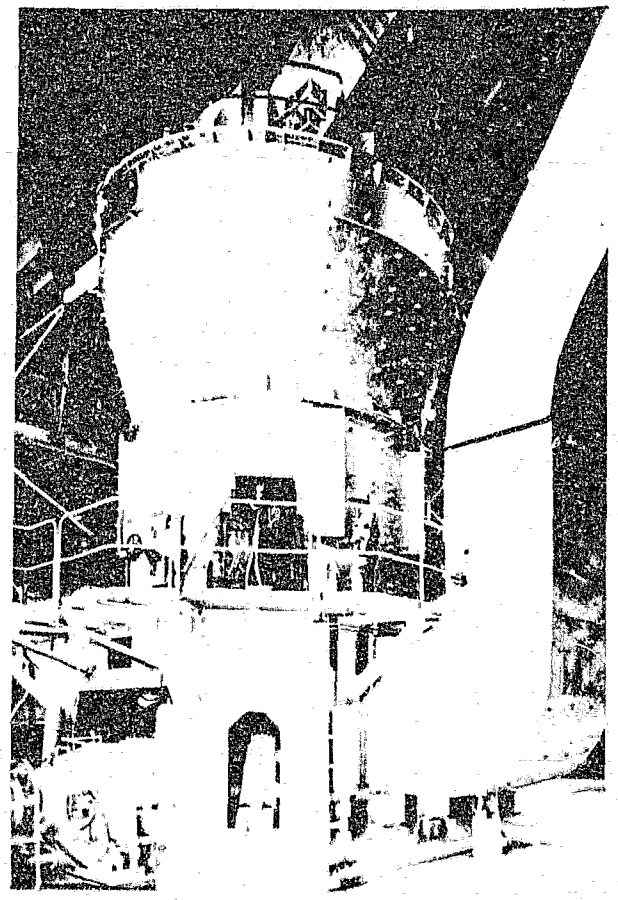


FIGURE 8.1: Large cement raw meal mill -Loesche LM 32/4

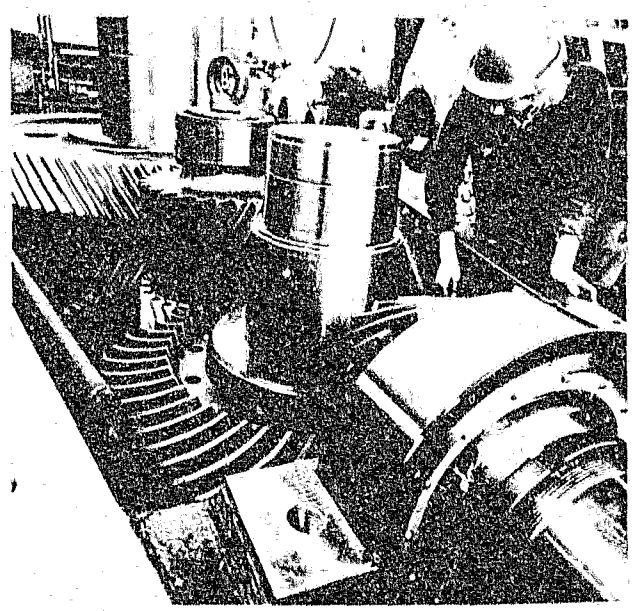


FIGURE 8.2: Gearbox for Loesche LM 32/4 mill

shutting the kiln down. However, this fear seems unfounded if current Continental practice is accepted. Accepting, then, that the milling units are going to be considerably larger in the not-too-distant future, some thoughts are now proposed as to how the design problems are to be tackled.

8.1.1 Mill Drive

The normal drive arrangement of the vertical spindle mill is a horizontal input into a reduction gearbox through a Bibby or similar type coupling. Assuming 8 - 9 kW/t power consumption on average, for, say, cement raw meal, the 350 - 300 t/h mills would required large motors of 3 200 to 4 500 kW, driving through equally large gearboxes. The following are the alternative solutions:

1) The development of a linear induction type motor around the mill table assembly. This would be bulky, and subject to tremendously stringent safety precautions. The hot gas temperatures reach 500°C, and this temperature might be imposed on the windings and insulation. A sturdy supporting base would still be required to take the roll thrust, and fitting the drive unit under the mill would be extremely difficult.

   The high cost of the 90° reduction drive is mainly attributable to the input pinion and bevel gears. A start has been made to altering this arrangement by using an in-line gearbox drive on a large Loesche mill. The motor is mounted vertically under the gearbox, as shown schematically in Figure 8.3.

2) Driving the rolls and not the table. This method has already been studied - but not very thoroughly - and presents distinct possibilities. Accepting that the

larger mills will have four or even six rolls, the mill motor rating could be split into four or six smaller drive units, each driving a roll through an extended roll shaft. To obtain the lowest speed - in the region of 50 r/min - radial hydraulic motors could be fitted on to the roll shaft and each motor coupled to either a central pumping set or to individual sets. The system would have the added advantage in that an optimum table speed could be selected for any operational condition. A disadvantage would be the lower motor efficiencies and resultant higher power consumptions.

For supporting the table thrust, a base mounted under the mill would house a pad-type thrust bearing as on present installations with locating bearings, and the huge and expensive gearbox would not be required. From a maintenance and availability point of view, this arrangement would be most favourable.

As to the feasibility of the drive arrangement, as mentioned previously, the problem has been studied on a small mill in the USSR with promising results. As soon as a thin layer of material has formed on the table the rolls will start to drive the table, and the same grinding action can be expected except that the bed will probably be thinner due to the roll action biting into the material layer on the table - this action is more satisfactory in that it is an established fact that the most efficient grinding is accomplished on a thin bed. Lower wear rates were also experienced in the USSR tests.

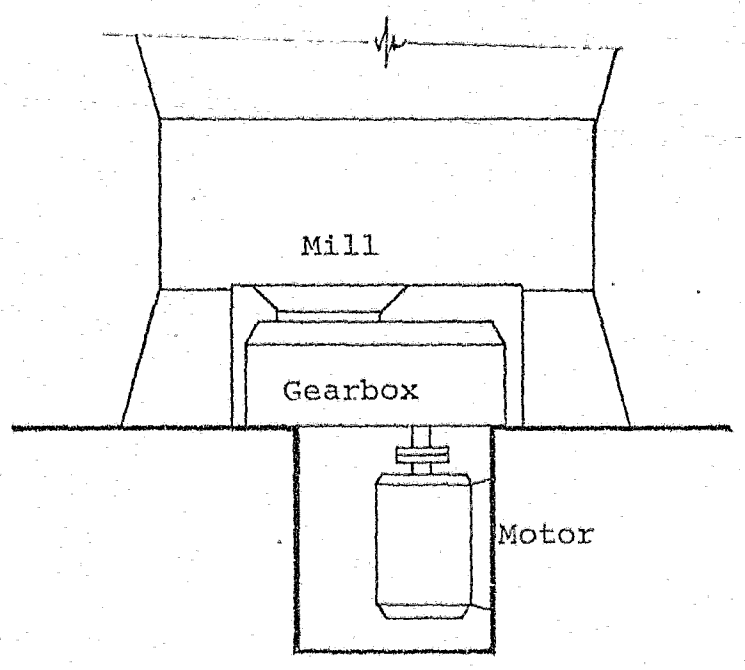


FIGURE 8.3: New Drive Arrangement for a Roller Mill

8.1.2 Mill Size

The principle of operation of the fluid flow aspect of the mill is simply that air entering the mill through the annular throat around the table entrains material spilled off the table, and conveys it to a separator. At the same time, the velocity of air within the main body, or plenum, of the mill must be low enough to allow oversize particles entrained by the high velocity throat air to fall back on to the table for further grinding - which necessitates a large mill volume above the table. Therefore, to keep the mill size within reasonable limits, and accepting the fact that the table must be large enough, for, say, four or six rolls, the velocity of the air above the table must be increased. This will mean entraining more oversize particles to the separator or, alternatively, re-designing the throat and dam ring to operate more effectively - ie, by allowing for mechanical impingement of oversize particles back on to the table or by squeezing ground fine material through slots

Author De Wet Kruger J I
Name of thesis A study of the parameters affecting the design of vertical spindle mills 1977

PUBLISHER:
University of the Witwatersrand, Johannesburg
©2013

LEGAL NOTICES:

Copyright Notice: All materials on the University of the Witwatersrand, Johannesburg Library website are protected by South African copyright law and may not be distributed, transmitted, displayed, or otherwise published in any format, without the prior written permission of the copyright owner.

Disclaimer and Terms of Use: Provided that you maintain all copyright and other notices contained therein, you may download material (one machine readable copy and one print copy per page) for your personal and/or educational non-commercial use only.

The University of the Witwatersrand, Johannesburg, is not responsible for any errors or omissions and excludes any and all liability for any errors in or omissions from the information on the Library website.